ABSTRACT

PRINCIPAL STRESS ANALYSIS OF ROCK FRACTURE DATA FROM THE LONG BEACH OIL FIELD, LOS ANGELES BASIN, CALIFONIA

By

Jacqueline A. Chavez

May 2015

Twelve electric borehole-image logs from oil wells located in the Long Beach oil field were used to conduct a fracture analysis of principal stress orientations associated with the Newport-Inglewood Fault Zone. The fractures analyzed are located in the Puente, Repetto, Pico, and San Pedro formations. Fractures were grouped based on fracture type, orientation, and formation. In-situ S_{Hmax} orientation was interpreted to range between 320° to 40° ($N40^0W$-$N40^0E$). Variations from the in-situ stress were observed across every formation and interpreted as paleo-stress. The S_{Hmax} orientation begins to change from NW to N-NW in the Pico Formation, which may signal the onset of the dextral movement of the Newport-Inglewood Fault 2.5 million years ago or later. The NE S_{Hmax} orientation in the San Pedro Formation may reflect stress trajectory changes as the Newport-Inglewood Fault continues to propagate in the Pleistocene. Additional S_{Hmax} orientations indicate a more complex structural evolution of stress trajectories.

PRINCIPAL STRESS ANALYSIS OF ROCK FRACTURE DATA FROM THE LONG BEACH OIL FIELD, LOS ANGELES BASIN, CALIFONIA

A THESIS

Presented to the Department of Geological Sciences

California State University, Long Beach

In Partial Fulfillment

of the Requirements for the Degree

Master of Science in Geology

Committee Members:

Thomas Kelty, Ph.D. (Chair)
Matthew Becker, Ph.D..
Hilario Camacho, Ph.D.

College Designee:

Robert D. Francis, Ph.D.

By Jacqueline A. Chavez

B.A., 2002, B.S., 2008 California State University, Long Beach

May 2015

ACKNOWLEDGEMENTS

I would like to thank everyone who offered their support and guidance throughout this thesis project. I was lucky to have so many great folks by my side.

To my advisor, Dr. Tom Kelty, a very heartfelt thank you for the opportunity to continue my education and be part of a project that taught me so much about the geology right under my feet. I am incredibly fortunate to have been under your instruction and grateful for all your encouragement and patience. Thank you for helping me stay focused on the prize and for "keeping it real" throughout this whole process.

To Dr. Matt Becker, thank you for agreeing to be on my thesis committee. Your knowledge of fractures and ability to zoom in on the goals were so helpful. I owe you a sincere "thank you" for narrowing the focus of this project to something more manageable during my advancement presentation. To Hilario Camacho, thank you for telling me that I could work full-time, go to school, have a family, and do it all while challenging me to be a better geologist at work and at school. Your passion for science is inspiring and I am fortunate to have had you as my boss, mentor, and thesis committee member throughout this journey. Thank you to CSULB, Geology for being awesome!

To Signal Hill Petroleum, Inc., thank you for all your support with this thesis. Without your generous donation of the data to CSULB this thesis would not have been possible. Thank you to my coworkers during my time at SHP who motivated me to work harder. There is no greater motivation than working full time and going to school—well, except maybe having your first child and another one on the way!

To my family, there are not enough words to express my appreciation and love for you all. To my dad, I owe my passion for geology to you. You introduced me to geology before I even knew it was called "geology." Your love of nature was infectious and I am eternally grateful for having had such an amazing dad that genuinely saw the beauty in a slab of rock. To my mom, your support allowed me to push forward, but seeing your strength made me want to do it. Thank you for everything, from sending me delicious food to watching my daughter so I could work on this project. I am so grateful to have the best mom ever! To my siblings, thank you for listening to my rants about school. Watching you guys push forward with your education has been inspiring.

To Ruben, my best friend, I do not know how to express in words how much I appreciate all the support and encouragement you gave me throughout this whole process. You believed in me from the start and kept telling me that I could do it, even when I doubted myself. Thank you for always knowing how to make me feel better and cheering me on when things got tough. Thank you for understanding that being a grad student requires a certain amount of selfishness with my time, and at times a certain amount of tears, but always a good amount of "mad scientist" wackiness. Thank you for taking on more than your fair share of responsibilities at home so that I could focus and work. You are the love of my life and I would not be where I am today without your unwavering love, encouragement, and support. I love you!

To Liliana, my daughter, thank you for letting "mommy work" and being my inspiration and sunshine. I love you! To Benjamin, my little bun in the oven, I cannot wait to meet you and tell you about writing a thesis while pregnant. You guys can be and do anything you put your mind to, but more importantly, be happy and follow your heart.

TABLE OF CONTENTS

CHAPTER Page

LIST OF TABLES

TABLE Page

LIST OF FIGURES

FIGURE Page

FIGURE Page

FIGURE Page

CHAPTER 1

INTRODUCTION

Statement of Purpose

Fractures are one of the most abundant geologic structures in nature (Davis and Reynolds, 1996). In academia and industry, there is a growing recognition that fractures significantly control the hydraulic behavior of subsurface fluids. However, fractures that affect hydrocarbon accumulations or aquifers are often a result of paleo-stresses that are different from the present-day stress (Engelder, 1992). Knowledge of the these stresses is an essential issue in petroleum exploration and production, and can affect reservoir drainage and flood patterns, fluid flow dynamics, borehole stability, hydraulic fracture stimulation, and geological interpretations. In this study fractures are used to characterize the principal stress orientations in the Long Beach oil field, which is located on the southwest margin of the Los Angeles basin (Figure 1).

Fractures in outcrops are well reported and their utility in evaluating present and paleo-stress regimes has been well established (Barton et al., 2009). However, fracture research in the subsurface is more challenging and subsurface data acquisition can be very costly. In recent years fracture-detecting technology has quickly evolved with several subsurface fracture-detection methods frequently used in the petroleum industry. This study utilizes electric borehole image logs from oil wells in the Long Beach oil field to detect and characterize fractures in the subsurface.

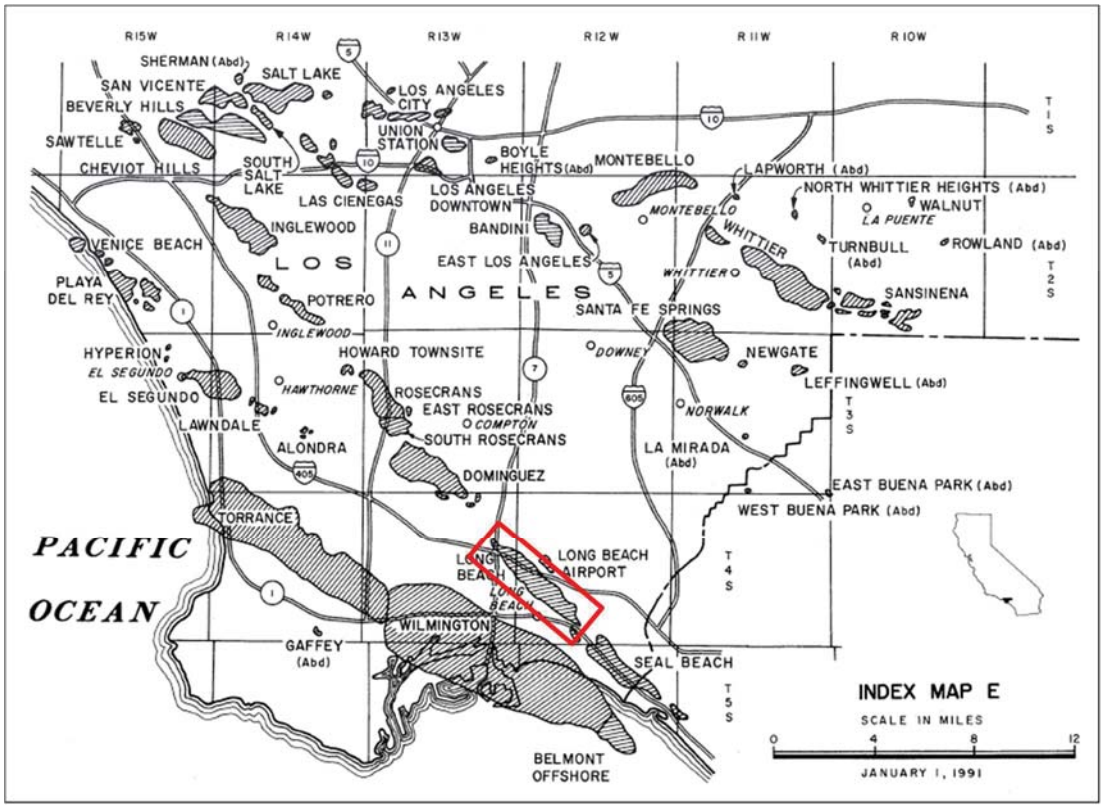

FIGURE 1. Map of the Los Angeles basin with study area outlined in red. Modified from DOGGER (1992).

This study is the first of this kind in the Los Angeles basin to be published. The purpose of this study is 3 fold. The first is to determine in-situ principal stress orientations using borehole breakouts and drilling-induced fractures. The second is to interpret principal stress orientations from natural fractures and determine if any variations exist between these and in-situ stresses. And third, to examine if any of these stresses validate the structural model for the Los Angeles basin and establish the onset of the Newport-Inglewood Fault in the Long Beach oil field.

This investigation tests two separate hypothesis: 1) fractures logged with electric borehole log images will reveal that differences exist between present and past principal stress orientations in the Long Beach oil field, and 2) these principal stress orientations

are associated with the structural evolution of the Los Angeles basin and can be used to established relative timing of the onset dextral movement of the Newport-Inglewood Fault in the mid-Miocene to late-Pliocene. If in-situ and past principal stress can be established in the Long Beach oil field, it would facilitate our understanding of the Newport-Inglewood Fault and Los Angeles basin, which have a complex tectonic and structural history (Wright, 1991).

Site Description and Well Location

The Long Beach oil field is located within the cities of Signal Hill and Long Beach, California, on the southwest margin of the Los Angeles basin. It is one of six major oil fields associated with the deformation of the Newport-Inglewood Fault Zone (Wright, 1991). The oil field has produced more than one billion barrels of oil since its discovery in 1921 and is one of the richest fields in the world in volume of oil produced by surface area (Division of Oil, Gas and Geothermal Resources [DOGGER], 2009; Wright, 1991). The oil field is currently operated exclusively by small independent oil companies, with Signal Hill Petroleum, Inc. being the largest operator. The wells used for this study were drilled and logged by Signal hill Petroleum, Inc and the data donated to California State University, Long Beach.

The Newport-Inglewood Fault Zone in this area has primary been mapped by previous workers using geomorphological surface features and subsurface well log correlations (i.e., Hill, 1971; Yeats, 1973; Wilcox et al; Harding, 1973; Wright, 1987, 1991). Structural and stratigraphic interpretations typically were developed using vintage well logs, core descriptions, and drilling reports. A drilling campaign that began in 2008 by Signal Hill Petroleum offered the first direct look at subsurface geological features via

modern electric borehole image logs. Moreover, it was the first time that fractures were directly confirmed and seen penetrating wellbores in the Long Beach oil field.

The field is located in a densely populated urban environment with limited ground surface exposure and no visible outcrops to study (Figure 2). Shortly after its discovery hundreds of oil derricks covered Signal Hill and the adjacent sections of Long Beach. Now, the field sits under commercial and residential development intermixed with oilfield infrastructure and oil wells. Fault scarps are not exposed, however there are significant offset along the fault zone. Elevation differences between the foot and hanging walls of the Newport-Inglewood Fault are apparent on the surface and the elevation difference can range from 55 to 355 feet. At the center of the oil field the Cherry Hill Fault scarp and Long Beach field anticline form the crest of the Signal Hill structure, which overlooks the Los Angeles basin.

The oil field is about five miles long by one mile across and runs along the strike of the Newport-Inglewood Fault Zone. In the NW, the field begins approximately at the junction between the San Diego Freeway (I-405) and the Long Beach Freeway (710). It roughly runs parallel to the 405 freeway up to the intersection of Lakewood Boulevard and Pacific Coast Highway in the east. In the south, the field is bounded by the Cherry Hill Fault, which is a locally named segment of the Newport-Inglewood Fault.

The field is divided into three major sections, which are the west, central, and east units (Wright, 1987). These divisions are based on historical lease lines, which sometimes roughly follow the outline of the major faults in the field. The wells used for this study are distributed among all three units. Figure 2 is a satellite image of the surface location of the wells. The wells are, from west to east: B2_rd3, A40_rd4, B35_rd1,

C33_rd1, 17-7_rd2, 23-6_rd2, 23-10_rd1, 20-24_oh, 20-23_oh, 23-8_rd2, 54_rd1, and 38_rd2. These wells were drilled and logged between 2008 and 2011. All the wells except A40_rd4 are oil production wells. A40_rd4 is the only well drilled for water injection and was the first well to be drilled in the Long Beach oil field in 2008 after a 30 year period of no drilling.

FIGURE 2. Satellite image with location of wells, oil field boundary, and Newport-Inglewood Fault (USGS, 2015). Modified from Google earth image (2015).

The study wells range from 710 to 7, 008 feet measured depth and penetrate the Pico, San Pedro, Repetto, and Puente formations. The depth intervals of the electric borehole image logs vary throughout the field and are governed by their drill-order, total-well depth, and targeted hydrocarbon bearing zone(s) of interest. Depending on the drill-order, the wells may initially break ground at the surface (original hole), or several feet from the subsurface if the well is a re-drill and was drilled out of a pre-existing wellbore.

As a result this and near surface casing put in place to project ground water, there are varying borehole image log depths and the stratigraphic sections available to study do not necessarily overlap for every well. Therefore, some formations have sections with more available data than others. These limitation and its possible implications will be addressed in the discussion and future work sections. Table 1 shows the well depths, logged depths, and logged formations of each well in the study.

TABLE 1. Electric Borehole Image Log Depths

Well Name	Total Depth (ft.)	Log Type (ft.)	Log Top (ft.)	Log bottom (ft.)	Puente Fm.	Repetto Fm.	Pico Fm.	San Pedro Fm.
17-7 rd2	6807	XMRI	4100	6775	x	x		
23-10 rd1	4297	XMRI	2300	4260		x	x	
23-20_oh	4441	FMI	761	4415		x	x	x
23-24_oh	4282	FMI	880	4490		x	x	x
23-6 rd2	6617	XMRI	2289	6505	x	x	x	
23-8_rd2	4318	XMRI	908	4310		x	x	x
38 rd2	7008	XMRI	1304	7002	x	x	x	x
54_rd1	5100	XMRI	1279	4923		x	x	x
A40_rd4	5544	FMI	950	5520		x	x	x
B2_rd3	5500	XMRI	2995	4940		x		
B35_rd1	4610	FMI	2400	4600		x		
C33_rd1	4783	FMI	695	4695		x	x	x

Note: Formations logged are designated with an "x." The two log types are Halliburton's X-tended Range Micro Imager (XMRI) and Schlumberger's Formation Micro Imager (FMI).

CHAPTER 2

REGIONAL GEOLOGY

Los Angeles Basin Evolution

The Los Angeles basin is one of at least twenty California Neogene sedimentary basins (Figure 3) that formed during the transition of the North American plate boundary from a convergent to a transform boundary (Atwater, 1970; Blake et al., 1978). The development of the Los Angeles basin consists of a three stage model of deformation during the Neogene period (Rumelhart and Ingersoll, 1997; Ingersoll and Rumelhart, 1999). These stages are described as transrotation (18–12 Ma), followed by transtension (12–6 Ma), and then finally by transpression (6–0 Ma) (Ingersoll and Rumelhart, 1999).

The three stage model is usually discussed in terms of three major basin-filling units, which correlate with the microplate-capture events that occurred during the conversion of the California coast from a convergent to a transform margin (Wright, 1991; Nicholson et al., 1994; Bohannon and Parsons, 1995; Ingersoll and Rumelhart, 1999). These basin-filling units consist of the Topanga, Puente, and Fernando formations, which range from Miocene to Pleistocene in age. The Fernando Formation is often divided into two units throughout the Los Angeles basin, which consist of the Repetto and Pico Formations.

Transrotation occurred during the capture of the Monterey and Arguello microplates by the Pacific plate (Nicholson et al., 1994) 18-12 million years ago

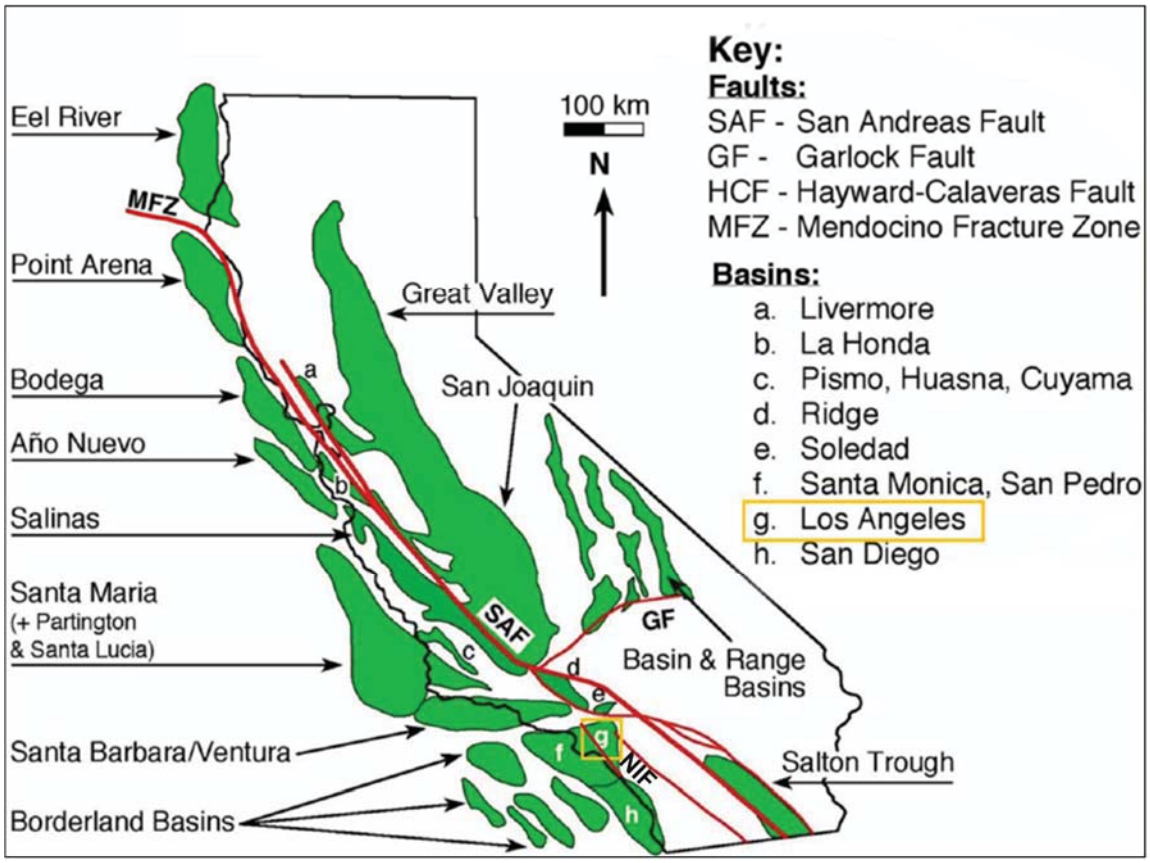

FIGURE 3. Locations of Neogene sedimentary basins. Los Angeles basin is boxed in yellow and NIF = Newport-Inglewood Fault, Modified from Lanners (2013), after Behl (1999).

(Ingersoll and Rumelhart, 1999). This is supported by paleomagnetic data that documents an average 90° clockwise rotation of the western Transverse Ranges (Atwater, 1970; Luyendyk and Hornafius, 1987; Luyendyk, 1991; Ingersoll and Rumelhart, 1999). During this vertical-axis rotation, upper Mesozoic and lower Cenozoic accretionary prism rocks were exhumed in the continental borderland by extension along low-angle detachment faults (Ingersoll and Rumelhart, 1999). This formed the Topanga basin, which is a precursor to the modern Los Angeles basin (Crouch and Suppe, 1993; Ingersoll and Rumelhart, 1999).

Transtension occurred 12-6 million years ago when rapid extension created the Puente basin, in which the Modelo and Puente submarine fans accumulated at bathyal depths (Wright, 1991; Critelli et al., 1995; Rumelhart and Ingersoll, 1997). During this time widespread deep-sea fans deposited the Puente Formation as the Los Angeles basin began to subside very rapidly beginning at 12 million years ago (Wright, 1991; Critelli et al., 1995; Rumelhart and Ingersoll, 1997). The bulk of the Monterey Shale, which is the primary petroleum source rock of the basin, was also accumulated during this time.

Transpression began 6 million years ago during a period of contraction and rapid uplift, which predominantly characterizes the neotectonics of the Los Angeles basin (Ingersoll and Rumelhart, 1999). At 6 Ma the southern San Andreas Fault became active as Baja California was transferred to the Pacific plate (Nicholson et al., 1994; Axen and Fletcher, 1998). Then, the restraining bend of the San Andreas Fault initiated contraction of the Fernando basin, which rapidly filled with upward-shallowing sediments of the Pliocene-Quaternary Fernando Formation and younger deposits in the Los Angeles basin (Wright, 1991). It is also during this phase that the Newport-Inglewood Fault is thought to have initiated dextral motion and developed as part of the southern California fault structure accommodating the tectonic deformation between the Pacific and North American plates (Wright, 1991; Grant and Shearer, 2004).

Newport-Inglewood Fault Zone

The Newport-Inglewood Fault Zone is a northwest striking, dextral, strike-slip fault zone that extends about 40 miles from Beverly Hills to Newport Beach, and is located along the western margin of the Los Angeles basin. In the north, the fault abruptly terminates at the Santa Monica Fault, while in the south it continues offshore. It

is part of the larger Newport-Inglewood-Rose Canyon Fault System, which extends from the Los Angeles basin to Baja California, Mexico (Grant and Rockwell, 2002; Grant and Shearer, 2004).

At the surface, the Newport-Inglewood Fault Zone is characterized by NW striking, dextral, left-stepping, discontinuous fault segments, and a series of faulted folds that comprise its onshore topography. These features are associated with extensional and compression fault duplexes related to releasing and restraining bends. The faulted anticlinal structure of the Long Beach oil field is one of these compressional structures.

The Newport-Inglewood Fault is described as overlying a major tectonic boundary (Wright, 1991). It is part of the local southern California system of faulting that accommodates the tectonic deformation between the Pacific and North American plates (Wright, 1991; Walls et al., 1998), where the greatest deformation occurs along the San Andreas Fault and decreases W towards the offshore borderland. It separates the continental granitic basement in the E from the metamorphic Catalina schist facies of the inner Continental Borderland to the W (Yerkes et al., 1995; Hill, 1971; Wright, 1991). It marks an area of structural weakness along a Mesozoic subduction zone that is thought to have reactivated with dextral motion in the middle Miocene to late Pliocene (Wright, 1991; Freeman et al., 1992). Presumably, the entire fault zone from the Los Angeles basin to Baja California is a major structural boundary within the Peninsular Ranges (Wright, 1991).

The strike-slip faulting of the Newport-Inglewood Fault initiated in the south and propagated to the north (Wright, 1991; Freeman et al., 1992). Evidence of this propagation is examined using cross cutting relationship from well data along the strike

of the fault (Wright, 1987; Wright, 1991; Freeman et al., 1992). In the Long Beach oil field, 4,000 feet of right-lateral offset of late Miocene to Pliocene strata has been used as evidence that faulting initiated in the late Miocene (Wright, 1987). However, it should be noted that available petroleum well data becomes limited with increased depth and a reevaluation of the lateral offset distance is needed with greater definition of the piercing points used.

The extensional and compressional duplexes of the Newport-Inglewood Fault Zone form petroleum traps, thus, it has been extensively studied by petroleum workers for the purpose of oil production. The Long Beach oil field is one of six major oil fields associated with the deformation of the Newport-Inglewood Fault. It was first recognized as a zone of folding by Mendenhall (1905) and later associated to seismicity and faulting by Hamlin (1918). It was first mapped and named as the Inglewood-Newport-San Onofre Fault by Taber in 1920, but later called the Newport-Inglewood Fault by Hoots (1931).

The tectonic history and subsurface structure of the fault is described in a series of classic papers by Hill (1971), Yeats (1973), Wilcox et al. (1973), Harding (1973), and Wright, (1987, 1991). Most of the data used for these papers originated in the petroleum industry from control wells used for exploration and production. These papers describe the Newport-Inglewood Fault as a structurally complex series of disconnected, en-echelon, strike-slip faults that have associated folds and secondary normal and reverse faults. It was often interpreted to be a classical example of wrench-style, strike-slip faulting associated with tectonic deformation (Harding, 1973).

More recently publications regarding earthquake surface ruptures and magnitudes (e.g., Grant et al., 1997; Hauksson, 1987; Hauksson and Gross, 1991) have identified geologic evidence of the faults seismic potential, while Tsutsumi et al., (2001) has characterized the faults propagation in the northern Los Angeles area. However, there appear to be no fracture studies associated with the Newport-Inglewood Fault that have been previously published. Thus, this study is the first of this kind to be published.

Long Beach Oil Field

Structure

The Long Beach oil field is located on the southwest side of the Los Angeles basin along the Cherry Hill Fault segment of the Newport-Inglewood Fault Zone. It is associated with the northwest-striking, dextral, strike-slip fault zone of the Newport-Inglewood Fault Zone. The field's structure is characterized by a 305° (N55°W) trending, faulted anticline, with bedding dips ranging from 45° in the S to 15° in the N. Historically, there have been four major faults mapped within the field: Cherry Hill Fault, Pickler Fault, Northeast Flank Fault, and Reservoir Hill Fault. There are also a group of smaller north striking extensional faults located at the crest of the anticline and a structurally undefined fault locally referred to as the Sports Park Fault that intersects the N limb of the field.

The Cherry Hill Fault is an oblique transpressional fault with vertical subsurface displacement up to 1, 100 feet and an estimated dextral displacement of about 4, 000 feet (Wright, 1991). It is striking 305° (N55°W) and dips vertical to 80° NE. The Pickler fault is a high-angle compressional fault that strikes 60° (N60°E) and dips 80° NE. It's estimated vertical displacement ranges from 900 to 600 feet. The Northeast Flank Fault

is a steeply dipping compressional fault that strikes from 330° (N30°W) to 300° (N60°W) and dips 75°NW. The Reservoir Hill Fault strikes 305° (N55°W) and has a nearly vertical dip. Figures 4 shows a subsurface structure map of the Long Beach oil field with locations of well intercepts in the Repetto Formation.

The eastern half of the field demonstrates a greater level of structural complexity than the west. It is characterized by two compressional fault duplexes. The most pronounced structure forms the structural high of the anticline. Here, crustal shortening is accommodated by the steeply dipping Picker and Northeast Flank faults relative to the Cherry Hill Fault. A smaller compressional structure is located towards the SE end of the field at the juxtaposition of the Northeast Flank Fault, the Reservoir Hill Fault, and the West Reservoir Hill Fault.

The wells used in this study vary in depth from approximately 4, 200 to 7, 000 feet measured depth. Imaged borehole log intervals range from 1, 945 to 5, 700 feet in depth. These intervals collectively penetrate the Puente, Repetto, Pico, and San Pedro formations, which range from Miocene to Pliocene in age. Fracture and principal stress analysis have never been conducted in the Long Beach oil field.

Stratigraphy

The stratigraphic column of the Long Beach oil field has historically been established within the context of the oil production discoveries of the field. The field has six named hydrocarbon producing zones which include, from deep to shallow, the DeSoto, Deep, Brown, Alamitos, Lower Wilbur, and Upper Wilbur zones (Wright, 1987). These zones are encompassed within three formations, which are, from oldest to

youngest, the Puente, Repetto, and Pico (Wright, 1987). The Pico Formation is overlain by the San Pedro Formation, which is not a hydrocarbon bearing zone, but is encountered

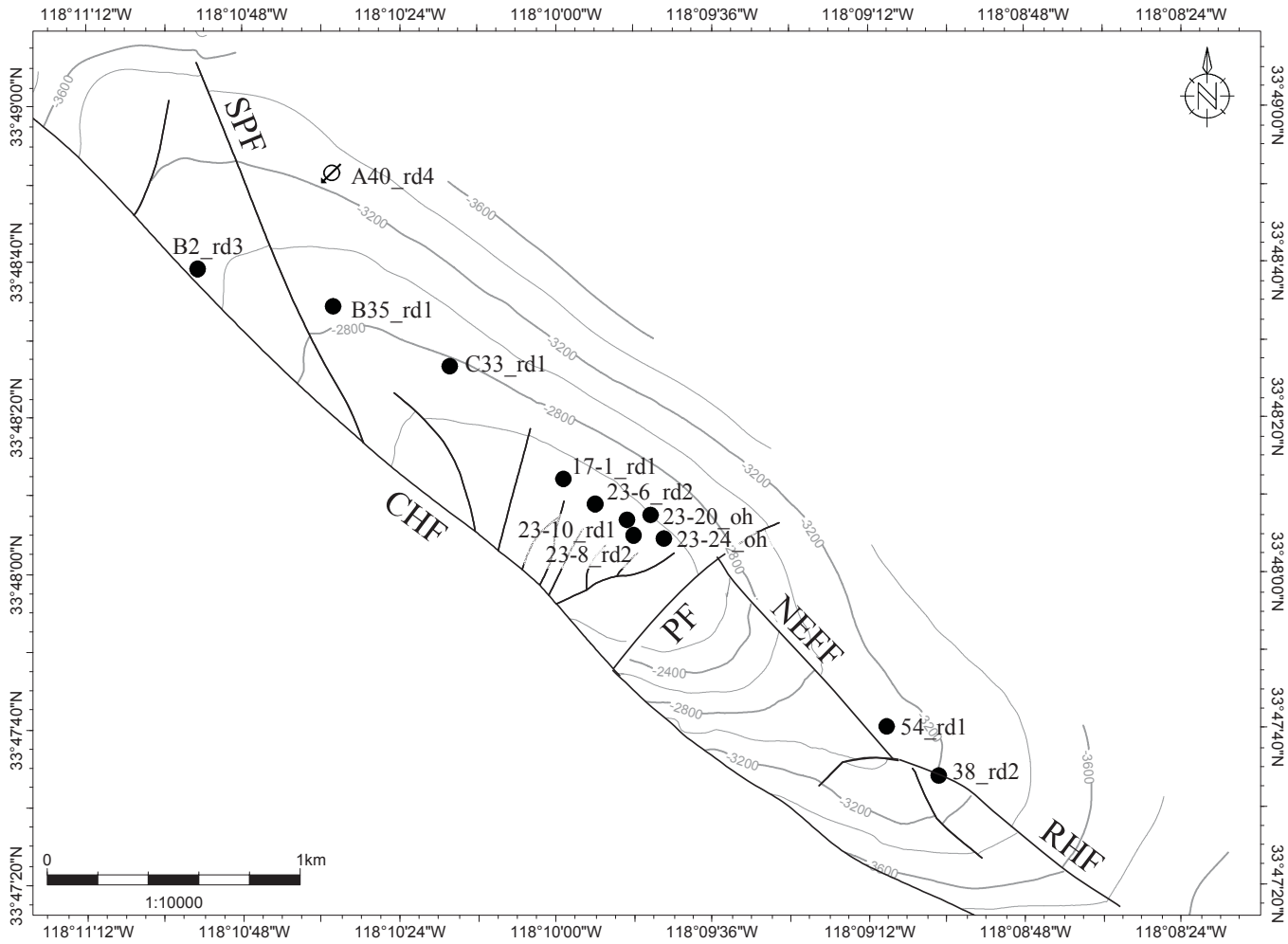

FIGURE 4. Subsurface structure map of the Long Beach oil field with locations of well intercepts in the Repetto Formation. Contours are 200 ft (61m) intervals at the top of the Alamitos zone. Fault name abbreviations are: CHF = Cherry Hill Fault, PF = Pickler Fault, NEFF = North-East Flank Fault, RHF = Reservoir Hill Fault, SPF = Sports Park Fault.

as wells were drilled from the surface to hydrocarbon bearing zones. These formations range in age from Miocene to Late Pleistocene.

The early to middle Miocene age Topanga Formation is not identified in the Long Beach oil field. However, it needs to be noted that detailed subsurface analysis of the structural and stratigraphic evolution of the Long Beach oil field is seriously hindered by the lack of data and deep well penetrations. Wright (1991) reported that deep wells show increased complexities with depth in the Miocene sections, but the data are too sparse to interpret. Consequently, the approximate top of basement rock or strata overlying it, are typically based on estimated regional controls (e.g., Wright, 1991) and have not been properly identified and classified in the Long Beach oil field.

In the subsurface of the Los Angeles basin the stratigraphic interval between the Topanga and Repetto formations have been designated the Puente Formation (Wright, 1991). In the Long Beach oil field, the Topanga Formation is not identified and thus all strata below where the Puente Formation is first identified in well log data is identified as the Puente Formation.

The Puente Formation is overlain by the Repetto Formation and was named by Eldridge and Arnold (1907) for its outcrop exposures in the Puente Hills. In Puente Hills it is divided into three members, which include a lower shale member, an intermediate sandstone member, and an upper shale member. However, the Puente Formation has considerable variation due to numerous unconformities, intertonguing, and gradational contacts (Yerkes, 1972; Wright 1991) and in the subsurface of the Long Beach oil field, members have not been identified.

The Puente Formation sections included in this study are characterized by massive to thin bedded sandstones interbedded with massive to thin bedded calcareous to siliceous siltstones, with occasional pebble conglomerates. The age of the Puente Formation is estimated at 13.4 Ma at the Topanga-Puente contact and 4.95 ± 0.15 Ma at the Puente-Repetto contact (Blake, 1991; Tsutsumi et al., 2001). The Puente-Topanga contact was estimated from radiometrically dated Conejo Volcanic exposed in the Santa Monica Mountains that date between 15.6 ± 06 to 13. 4 ± 0.9 Ma (Weigand and Savage, 1993). This age was used because the Topanga Formation is found to be interbedded with basalts in the Sawtelle and Inglewood oil fields (Blake, 1991; Wright, 1991; Tsutsumi et al., 2001) that may be equivalent in age.

However, it is possible the oldest strata included in this study may actually be between 16.4 to 7.2 Ma old. This age was established using biostratigraphy analysis of wet mud log samples obtained while drilling well 38_rd2, which is the deepest well used in this study. An age model was established using the first and last occurrence events of foraminiferal, nannofossils, and playnological events for samples collected from 4, 500 to 7, 008 feet deep. This interval samples Pliocene to Miocene age ranges. The biostratigraphic analysis was conducted by Biostratigraphy, LLC for Signal Hill Petroleum, Inc.

The large range between the possible ages is due to the differences between the first and last appearance of biostratigraphic markers found in the well. The age-depth model used calculates the sedimentation rate for intervals between age defining events and uses the last appearance datum (LAD) events (Zippi, 2011). However, first appearance datum (FAD) events also provide additional age constraints since samples

can be contaminated with sediment from shallower intervals that "spall-off" in the wellbore. Using the LAD age-depth model the projected age at the total depth for this well is Late Miocene, Tortonian, 7.97 Ma (Zippi, 2011). The oldest age of 16.4 Ma Middle Miocene, Langhian, age is established using a FAD approximately 100 feet from the bottom of the well, while the younger age of 7.2 Ma Late Miocene, Tortonian, was determined from a LAD collected approximately 550 feet from the bottom of the well (Zippi, 2011). Barring no known contamination or reworking of older fossils, the date of 16.4 Ma is the age allocated to the oldest strata penetrated in this study.

The Pliocene to early Pleistocene Fernando Formation overlies the Puente Formation and is divided into the Repetto and Pico members. In the Long Beach oil field the Repetto and Pico members have historically been characterized as two separate formations due to the differences in strata and hydrocarbon producing zones. This study uses the local distinction and refers to these members as the Repetto and Pico formations.

The Repetto Formation is characterized by fine- to course-grained sandstone interbedded with sandy micaceous shale, siltstone, and clay that represent submarine fan deposition at lower bathyal water depths. The age at the base of the Repetto Formation contact is estimated as 4.95 ± 0.15 Ma while the top contact is estimated as 2.5 Ma (Blake, 1991). This lower Pliocene formation is considered the most extensive Pliocene unit in the Los Angeles basin (Wissler, 1943). In the Long Beach oil field, it contains the greatest number of hydrocarbon bearing zones, which include the Brown, Alamitos, and Lower Wilbur zones, and the top contact is found at an average depth of 2, 400 feet subsea (Wright, 1987).

The Pico Formation overlies the Repetto Formation and is overlain by the San Pedro Formation. It is composed of coarse-grained, marine sand and gravel deposits of middle to upper bathyal water depths that fine upwards to massive, micaceous siltstone and claystone, interbedded with silty sand of inner neritic environments. These sediments range from upper Pliocene to upper Pleistocene, and the age of the base of the Pico Formation is estimated as 2.5 Ma, while the top is estimated as 0.9 ± 0.1 Ma (Blake, 1991). The Pico Formation contains the Upper Wilbur producing zone and is typically found at a subsea depth of 2, 000 feet (Wright, 1987).

The Pico Formation is overlain by alluvial and fluvial deposits, which in the Long Beach field are names as part of the San Pedro Formation. The San Pedro Formation consist of yellow-brown silt, sand, clay, and gravel sediments of nonmarine to inner neritic depositional environments. These upper Pleistocene to Holocene strata represents the transition from inner neritic to nonmarine depositions in the Los Angeles basin (Blake, 1991). The age of the base of these deposits are estimated as 0.9 ± 0.1 Ma (Hummon et al., 1994; Tsutsumi et al., 2001). In the Long Beach oil field, the San Pedro Formation does not contain any economic hydrocarbons. The base of these strata on average are found at about 2, 000 feet and the lithological units found above are all grouped into this formation.

CHAPTER 3

METHODS

Data Acquisition

The wells used for this study were drilled by Signal Hill Petroleum Inc. between 2008 and 2011, and logged by Halliburton and Schlumberger. The well data was later released and donated by Signal Hill Petroleum to California State University, Long Beach for academic research. Since two service companies were involved in logging the wells there are two brands of electric borehole image logs used in this study: Halliburton's X-tended Range Micro Imager (XMRI) and Schlumberger's Formation Micro Imager (FMI). Both of these logs are acquired using similar wireline based dipmeter and resistivity imaging tools.

The FMI and XMRI tools are configured with four and six arm, respectively. Resistivity imaging tools can have variable number of pads with variable number of electrodes on each arm (Lagraba et al., 2010). Figure 5 illustrates this tool configuration. Each arm contains an associated pad with sensors and a secondary pad called a flap. The sensors contain electrodes which are spaced circumferentially around the wellbore. The arms open and close to measure the borehole radii and are controlled from the surface by a logging engineer. As the tool travels up the borehole an electrical current is injected from electrodes into the formation. Pressed against the borehole, the sensors on the pads record the electrical currents injected from the tool into the formation as it returns to an

electrode in the upper part of the sonde, essentially measuring the current after it interacts with the formation and fluids (Lagraba et al., 2010).

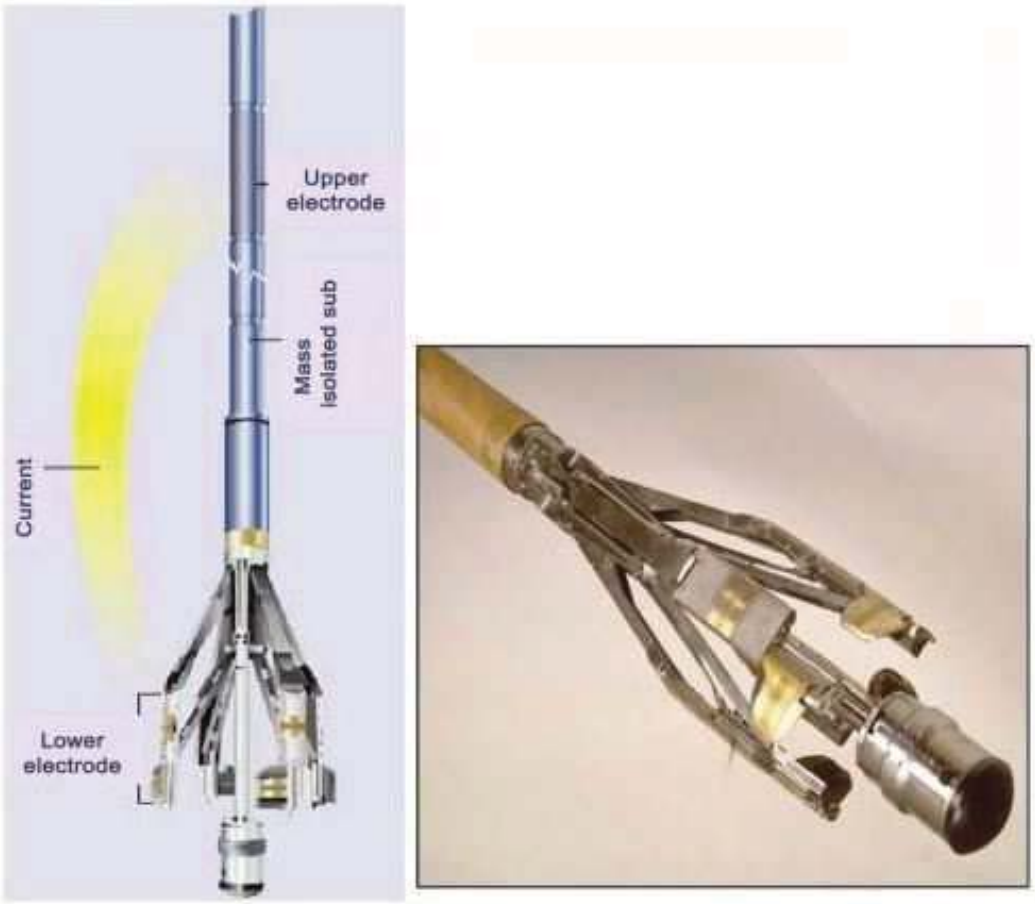

FIGURE 5. Tool configuration of a Formation Micro Imager. Four arms and associated pad and flaps are shown (Lagraba et al., 2010).

The FMI tool has arms mounted with four pads and four flaps. These pads and flaps have two rows of 12 buttons, which contain 192 sensor electrodes. The sensors are arranged in two rows and overlap in order to provide adequate coverage. Schlumberger reports that the FMI has a vertical resolution of 5 mm (0.2 in.), which means that features at least that small maybe visible depending on its resistivity contrast with the background

matrix (Schlumberger, 2002). The FMI's depth of investigation (DOI) is shallow, at approximately 5 cm (2 in.) or less, but can reportedly respond to deeper signals depending on the resistivity contracts of the formation across the measured interval (Lagraba et al., 2010).

The XMRI tool operates under the same general physical principals as the FMI since they are both electric borehole imaging logging tools. However, the XMRI has six arms instead of four that move independently (Halliburton, 2008). The percentage of borehole wall coverage decreases as the hole size increases (Lagraba et al., 2010). The FMI reportedly provides 80% coverage in a 8-inch borehole size (Schlumberger, 2002), while the XMRI reports 67% in a 8.5-inch borehole (Halliburton, 2008).

7

Post-Acquisition Processing

After logging the acquired data requires post-acquisition processing to correct for any gain, offsets, and emitter-exciter discrepancies. Post-acquisition processing is also needed to normalized microresistivities of button-to-button and pad-to-pad. Additionally, because the resistivity pads are highly sensitive to mud cake content and thickness, as well as borehole shape and rugosity, the data is further normalized to account for these factors (Hansen and Buczak, 2010). This post-acquisition processing was done on location by the logging engineer for all the image logs used in this study. Once these processing steps were completed the electronic-log data was sent to a log annalist for further processing, while a field-log print and digital files were given to the company representative.

Additional in-house processing of the acquisition data is necessary to enhance the image quality of the FMI and XMRI logs. These processes include scaling and color

mapping, and were applied by Schlumberger and Halliburton to all the logs used in this study. Raw data from image log sensors commonly have skewed distributions or pronounced values. This distribution of the raw data has to be scaled to equal distributions. This step is necessary because the image is derived by mapping the measurement scale onto a color map to produce statically or dynamically normalized images. In static images, each resistivity value is assigned a unique color over the entire logged interval, were as in dynamic images, the color scale is continuously renormalized within a specified depth window to increase contrast and enhance features. The logs in this study have both statically and dynamically normalized image tracks.

Once the static and dynamic images have been processed, the logs are ready for image-log interpretation. This may include identifying bedding dip, faults, fractures, stratigraphy, and structural features. The degree and quality of interpretation vary for each log used in this study. In some cases, "auto-dip" picking was the only method applied, but often at least some form of manual-dip picking was conducted by Schlumberger or Halliburton for varied structural and/or stratigraphic features in the image logs. In regard to fractures, most of the logs have some degree of fracture dip identification that was conducted by the service companies; however, the quality, consistency, and nomenclature of the fractures and their respective dips vary significantly between the two service companies and between varied log analysts. The limitations and effects of post-acquisition processing, along with the depth of investigation, vertical resolution, and borehole coverage of the logs will be addressed in more detail during the recommendations for further research chapter.

Fracture Identification Methodology

Under perfect drilling conditions a borehole image would cover the entire surface of the borehole similar to that of an unslabbed core and mirror the utility of a circumferential core photograph. An image log can be thought of as a cylinder that is opened. Conventionally, images are oriented with the north or high side displayed to the left, representing the cut. In unwrapped images planar features that intersect the borehole will appear to be sinusoids (Figure 6) (Hansen and Buczak, 2015). Thus, dip picking of surface can be done by fitting a sine wave to these structures. Conventionally, these sine waves are displayed directly on the image and are accompanied by "tadpoles" representing the dip and azimuth of each structure on a neighboring log track.

Weather using software or picking fractures orientations directly from the logs, the basic variables used to calculate the dip direction and angle of a fracture or any planar feature that intersects a borehole are the vertical intercept (h) of the fracture, the direction of the dip from the image log, and the diameter (d) of the borehole. Using these variables the angle of the dip is equal to the arctangent of h/d, and the dip direction is picked at the trough of the sinusoid on the image log (Mattioni et al., 2010). This calculation can be applied directly to an image or calculated automatically when using dip-picking software.

Where fractures are identified by the service companies, these structures were identified and labeled using sinusoidal matching software. This process is initially done automatically by software, in what is called "auto-dip" picking or "automatic-dip' picking, then manually inspected by a company log analyst who makes adjustments or additions. However, there are varying interpretations of fracture types and nomenclatures between the twelve image logs. Fracture nomenclature, definitions, and interpretations

vary between the two service companies and between log analysts. Furthermore, often fractures are incorrectly interpreted or labeled, often misrepresented as fault or vice versa, or not identified at all on the image logs. Hence, fracture orientations and types were independently identified and interpreted by myself for this study.

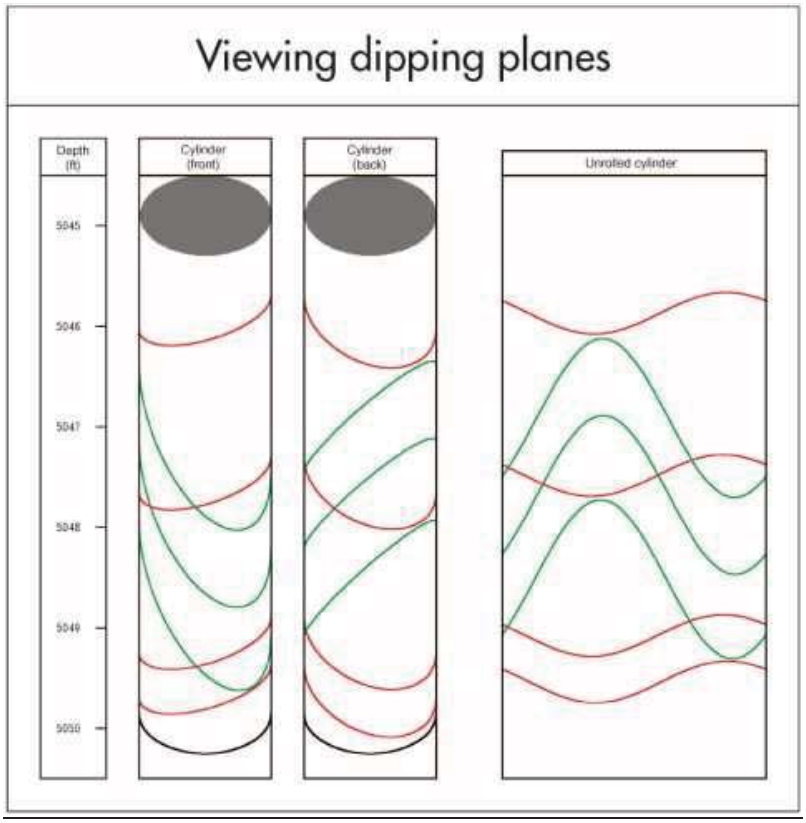

FIGURE 6. Planar features cutting a cylindrical section of a borehole (Hansen and Buczak, 2010).

Fractures were identified using dip-picking software or, when not available, directly from the image-log prints. Two different software programs were used to manually dip pick fractures, which are Halliburton's *Ready View* and Schlumberger's *Welleye*. The software programs were log specific and provided by their corresponding

service companies with each log acquisition. The software, apart from a convenient presentation of images, provides the ability to fit sine waves to visible fractures and allowed for their categorization. The software converted the pitch and position of a fitted sine wave into a dip and azimuth of the dipping plane, and accounted for the logging tool orientation, hole size, and borehole direction. It also provided multiple view points and enhancements of the images which aided the very laborious task of manually dip-picking the over 1, 500 fractures found in the 41, 574 feet of image logs examined.

Additionally, apart from the categorization of full sine-wave planar features, the *Ready View* software included with the Halliburton logs provided the ability to pick other features such as breakout, tensile fractures, and partial sine waves for fractures only visible partway around the hole. For the Schlumberger logs, these features were directly confirmed against (if initially provided by Schlumberger) or directly identified on the log prints themselves.

For each fracture pick, the quality of the dip picked was recorded as excellent, good, fair or poor in a Likert-type scale of 1 to 4 respectively. The ranking of 1 is the highest quality and the least ambiguous pick, which is derived from a structure with a continuous trace along the borehole wall that matches a sinusoid very well. As the quality of the ranking deceases, from 1 to 4, the amount of subjective interpretation increased. Structures assigned a quality ranking of 4, or poor, frequently did not match a sine wave and often involved connecting discontinuous or ambiguous segment to define a fracture plane. Fractures that had orientations that could not be determined or were considered too ambiguous where not used in this study. As a result, conservative picking in this study may underestimate the total number of fractures, but should yield reliable

analysis of structure orientation and distribution. Sampling bias of fractures will be discussed in more detail during the discussion.

For each fracture analyzed, the morphology of the structure was characterized and grouped into a fracture type. The fracture types identified for this study are: conductive fractures, resistive fractures, partial fractures, induced fractures, borehole breakout, and Petal fractures. The morphology of these groups as identified and used for this study are defined in the text to follow. Although the primary focus of this study was fractures, faults where also used in the analysis of principal stress direction. Thus, fault orientations were also pick when a strike and dip were obtainable and picks were subdivided into two groups, micro-faults and faults. Figure 7 shows some examples of the imaged fractures and faults logged.

Resistive fractures are high-angle structures relative to bedding that are highlighted by a bright resistivity contrast and/or a halo relative to the matrix lithology. This high resistivity is likely attributed to secondary mineralization in the fracture's aperture. These structures can cut across bedding contacts or terminate in a single lithology, are typically symmetrical, and frequently look like sinusoids in borehole images. Thus, the orientations of these fractures tend to be highly reliable since they are easily matched to a sine wave.

Conductive fractures look similar to resistive fractures, but are marked by a dark conductive contrast relative to the matrix lithology. The high conductivity contact can be attributed to conductive material in fracture apertures, such as conductive fluid (saline rich water), drilling mud, or soft sediment fill. Conductive fractures also tend to have high quality dip orientations similar to resistive fractures.

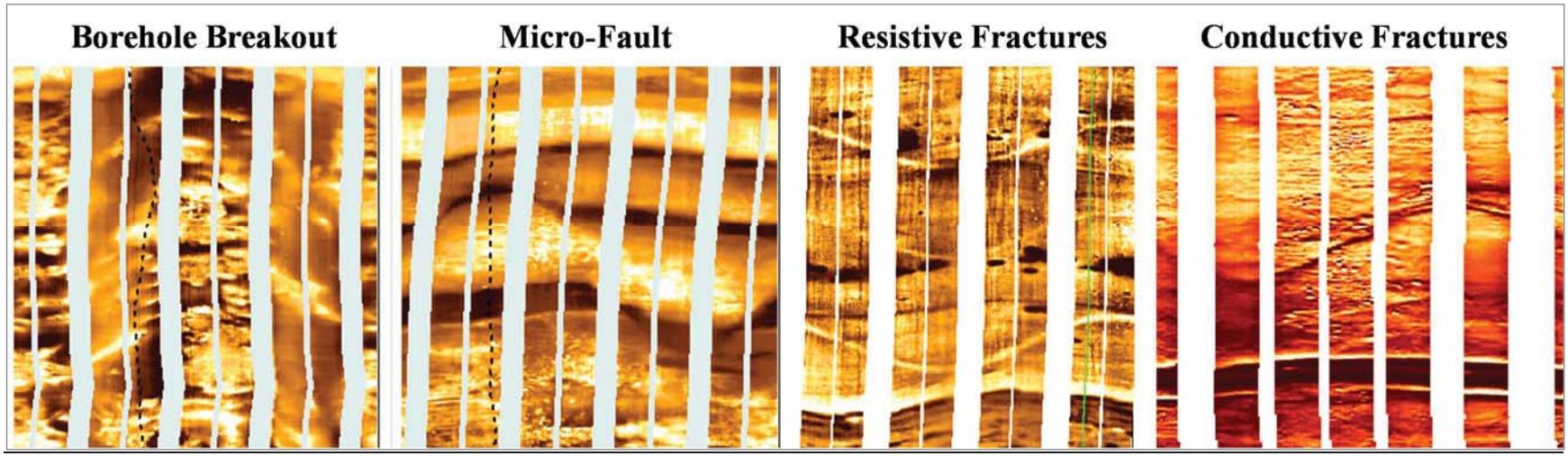

FIGURE 7. Examples of imaged fractures analyzed.

Partial fractures are high-angle features relative to bedding that appear discontinues and/or asymmetrical. As a result, it can be difficult to match a sinusoidal wave and frequently involved connecting discontinuous or ambiguous segment to define a fracture plane. Consequently, the orientations of these fractures are less unreliable and have a low quality ranking. Furthermore in this study, partial fractures are typically more conductive than the matrix lithology, but a few have sporadic resistivity or are at least partially resistive. There were no partial fractures that appear entirely resistive in any of the image logs used in this study.

Micro-faults are identified in the image logs as symmetrical, sinusoidal, high-angle structures relative to bedding, with offset bedding planes on either side of the structure. Displacement is minimal, appearing to be less than two feet in most cases, and bedding planes can be correlated across the structure. Additionally, there is no significant change in dip azimuth above or below the structure. They can look similar to conductive and resistive fractures on image logs, but are categorized differently based on their displacement of beds. Likewise, micro-faults also tend to have relatively high quality rakings.

Unlike micro-faults, which look similar to resistive or conductive fractures, larger faults may not appear symmetrical, and/or do not have offset bedding planes that can be correlated on either side of the fault in the image logs. These faults typically have a larger section of apparent offset than what the image log can capture. For these picks the dip and strike orientation can still be captured with a sine wave, but often other methods, like lithological log correlations and structural position, where identified it as a fault

rather than a fracture. Additionally, there was often a significant change in dip azimuth above and below these structures.

Two types of drilling induced fractures were identified in this study, borehole breakout and tensile fractures. Borehole breakout are vertical failure fractures or failed elongations along the borehole wall. They appear on image logs as broad, parallel, often poorly resolved conductive zones, which are separated by 180° and exhibit caliper enlargement in the direction of the conductive zones (Tingay et al., 2008). Tensile fractures or drilling-induced fractures are conductive, parallel, vertical fractures along borehole walls that often do not terminate in a single lithology. They also appear 180° apart in image logs, but do not form broad poorly resolved zones or elongate the borehole like borehole breakouts (Rajabi et al., 2010). These two types of fractures were used to determine present-day stress.

Principal Stress Interpretation Methodology

Principal stress regimes in the Long Beach field were determined and analyzed using both natural fractures, borehole breakout, and drilling induced tensile fractures. In-situ maximum principal stress orientation was established from borehole breakout and drilling induced tensile fractures. Principal stress orientations of natural fracture were interpreted using Anderson stress model and examined against their fracture type. Stress regimes interpreted from natural fractures were then compared with the in-situ stress determined from the drilling-induced fractures, and tested against the anticipated principal stress orientations of the Los Angeles model, and the dextral onset of the Newport-Inglewood Fault.

The present-day S_{Hmax} orientation was determined from borehole breakouts in the image logs. As a borehole is drilled, the material removed from the subsurface is no longer supporting the surrounding rock, resulting in concentrated stresses in the borehole. The stress-induced elongations or borehole breakout of the borehole occur when the circumferential stress exceeds the stress required to cause compressive failure of the matrix rock (Bell and Gough, 1979). Thus, the resulting elongation of the borehole (Figure 8) is the result of compressive shear failure on intersection conjugate planes, which result in sections of the borehole wall to spall-off (Bell and Gough, 1979). The maximum circumferential stress around a vertical borehole occurs perpendicular to S_{Hmax}. Thus, borehole breakouts elongations occur perpendicular to the present day S_{Hmax} direction and along the S_{Hmin} direction (Bell and Gough, 1979).

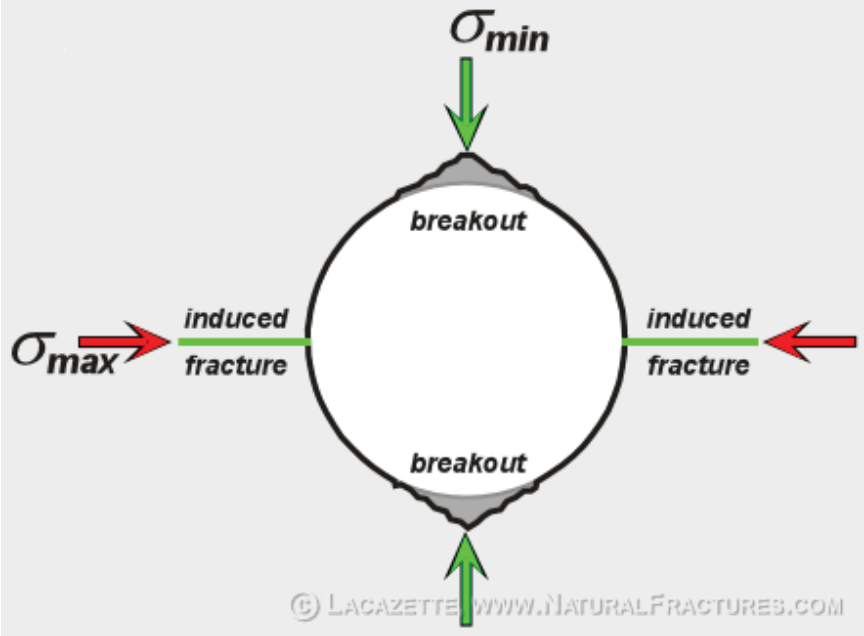

FIGURE 8. Geometry of borehole breakouts and induced fractures (Lacazette, 2015).

Drilling-induced fractures form during different stages of drilling the wellbore. Petal and centerline fractures often form just beneath and ahead of the drill bit as a result of mud pressure and bit weight, while tensile fractures develop when drilling mud hydraulically fractures the borehole wall. Drilling induced tensile fractures occur in the borehole wall where the circumferential stress is negative and exceeds the tensile strength of the matrix rock. These fractures form parallel to the borehole axis of S_{Hmax} in vertical wells (Figure 8) (Barton et al., 2009; Zoback, 2009) and, thus, were also used to infer present-day stress since all the wells used in the study were vertical or near vertical.

Natural fractures found in the image logs were used to examine principal stress patterns and possible variations from neostress. Using the standard engineering fracture mechanics terminology (Boek, 1982), which classifies fractures by the relative movement of the fracture walls during propagation, the fractures identified in the image logs are interpreted to be natural Mode I rock fractures, or joints. Furthermore, the plane of a propagating joint is considered to be perpendicular to the localized least principal stress that prevailed during that joints propagation (Engelder 1987). Therefore, the orientation of a joint within a volume of rock directly indicates the orientation of the minimum paleostress at the time that joint was formed (Figure 9) (Engelder 1987, 1992; Lacazette, 2009). Thus, by applying the principles from Anderson's stress model, the orientations from the natural fractures identified in the image logs were used to identify the prominent stress regime at the time of their formation.

Similarly, Anderson's stress model (Anderson, 1942) was used to analyze the paleostress of the fault as well, primarily focusing on the principal that when faults form, they originate as conjugate sets that are oriented parallel to the intermediate stress axis

and are commonly ±22 to 30° from the maximum stress axis (Lacazette, 2009). However, there are limitations regarding faults and image logs. The slip direction and architectural structure of a fault is not normally visible in image logs. As a result, observations of offset beds can sometimes crudely define the slip sense, but not the slip direction of a fault, which limits the application of Anderson's stress model and allows for more ambiguous interpretations of stress regimes. Thus, where conjugate patterns emerged, faults were more "loosely" used to complement observations noted from fracture data.

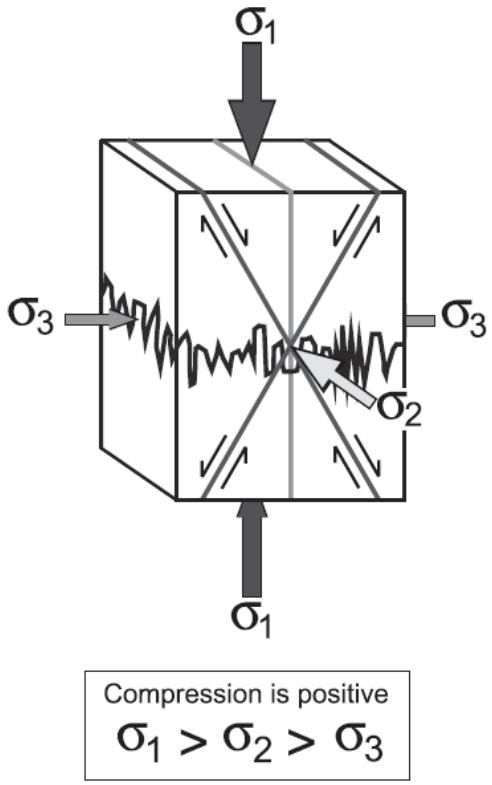

FIGURE 9. Orientation of fractures relative to principal stress. Fracture joints are parallel to the maximum compressive stress and perpendicular to the minimum compressive stress (Lacazette, 2009).

Fractures record the stress field at the time of their formation. Engelder (1992) provides three reasons why natural fracture orientations are often not related to the present day stress regime in a rock. First, fracture orientations reflect the direction of stress in the rock at the time the fracture was formed. Second, regional stress changes through geologic time. Third, the majority of natural fractures formed during the geological past under the influence of ancient stresses (paleostress) that do not prevail today. Thus, variations from the in-situ stress can be interpreted as paleo-stresses and used to understand the geological history of the fractured rock.

Fracture Diagrams

Fractures orientations were plotted on stereographic pole diagrams and rosette-strike plots using Petrel software. Diagrams were made for each well, fractures type, and formation. The plots were then used to examine fracture patterns and define stress regimes using Anderson's stress model mentioned in the previous section.

CHAPTER 4

RESULTS

Data Overview

A total of 1, 539 fractures and faults were interpreted using electric borehole image logs from the wells used in this study. These fractures and faults were then defined and divided into distinct fracture type sets and subsets, which include natural fractures, drilling induced fracture and fault subsets. Of these data, 1, 160 are identified as natural fractures, which consists of 73.3 percent of the total data interpreted for this study. This group of natural fractures is further subdivided into three sets, which include conductive fractures, partial fractures, and resistive fractures. The total number of fractures allocated to each type or subset is, in descending order: 488 conductive fractures, 399 partial fractures, and 242 resistive fractures. These numbers respectively represent 31.7 %, 25.9 %, and 15.7 % of the total data for this study (Figure 10).

A total of 229 drilling induced fractures were interpreted and grouped into subsets. This represents 14.9 percent of the total fracture data interpreted for this study. These fractures do not occur in nature and in this study are subdivided into three types, which include borehole breakout, induced, and petal fractures. The total number of fractures allocated to each type is, in descending order: 139 petal fractures, 58 borehole breakout fractures, and 32 induced fractures. These volumes respectively represent 9 %, 3.8 %, and 2.1 % of the total data for this study (Figure 10).

One hundred eighty-two faults were interpreted and divided into two types of subsets, which together make up 11.8 percent of the total data interpreted for this study. The two subsets are defined as faults and micro-faults. The data consist of 92 micro-faults and 89 faults, which respectively represents 6.0% and 5.8 % of the total fracture data for this study (Figure 10).

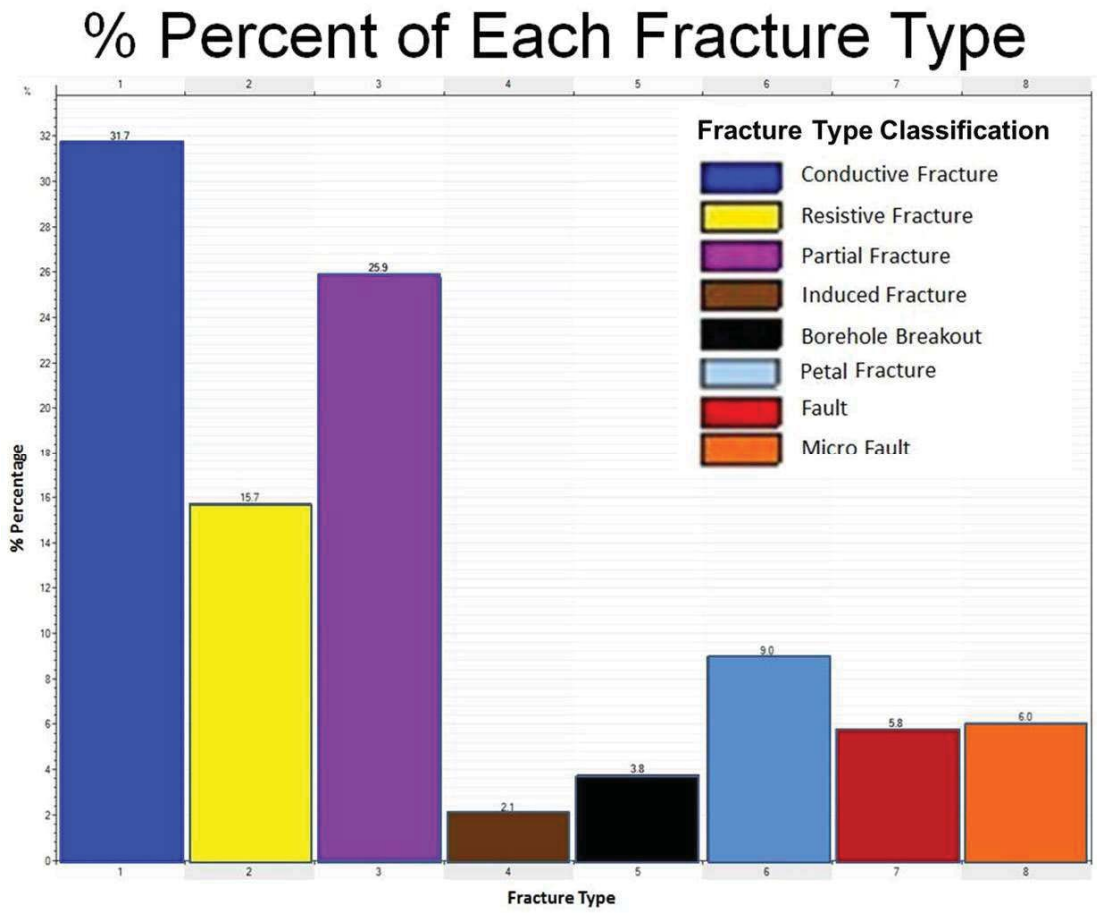

FIGURE 10. Percent of each fracture type.

The orientations of the fractures and faults were plotted on Schmidt stereonets that include rosette-strike polar frequencies. Dips are plotted as poles to the dip plane and a lower hemisphere projection was applied. Rosette increments of 10 degrees were

also applied to all the plots. With the exception of the first plot, all stereonets presented are 2D equal-area plots. The data plots presented in this thesis include stereonets of all these data, fracture type sets, and fracture type sets for each formation

The results observed of all the data is examined, followed by the results of plotting individual fracture types, and then the results of plotting individual fracture types for each formation. Figure 11 is a lower hemisphere, equal-area stereonet of all the data. It shows a broad range of fracture orientations with a few distinct clusters that can be observed. However, more detail can be observed when fractures are plotted by fracture type and formation. The subsequent sections will discuss these results.

Fracture Orientation Sets

Fracture Type Sets

Figure 12 is a stereonet of all the conductive fractures interpreted in this study. It consists of a large diversity of fracture orientations, with three wide-ranging sets of orientation. These sets are generally defined by greater rosette-strike frequencies and are divided where short intermittent frequencies exist. These broad sets range in orientations between 50° to 80° (N50°-60°E), 290° to 40° (N70°W-N40°E), and 260° to 270° (N90°-80°W). Within these ranges there are two sets that occur more frequently and are considered the dominant orientations. These sets have rosette-strike orientations between 10° to 20° (N10°-20°E) and 50° to 60° (N50°-60°E) azimuth.

Conversely, the resistive fractures interpreted in this study have one distinctive and dominant fracture set by comparison. These fractures are primarily oriented W-NW between 270° and 320° (N50°-90°W) (Figure 13).

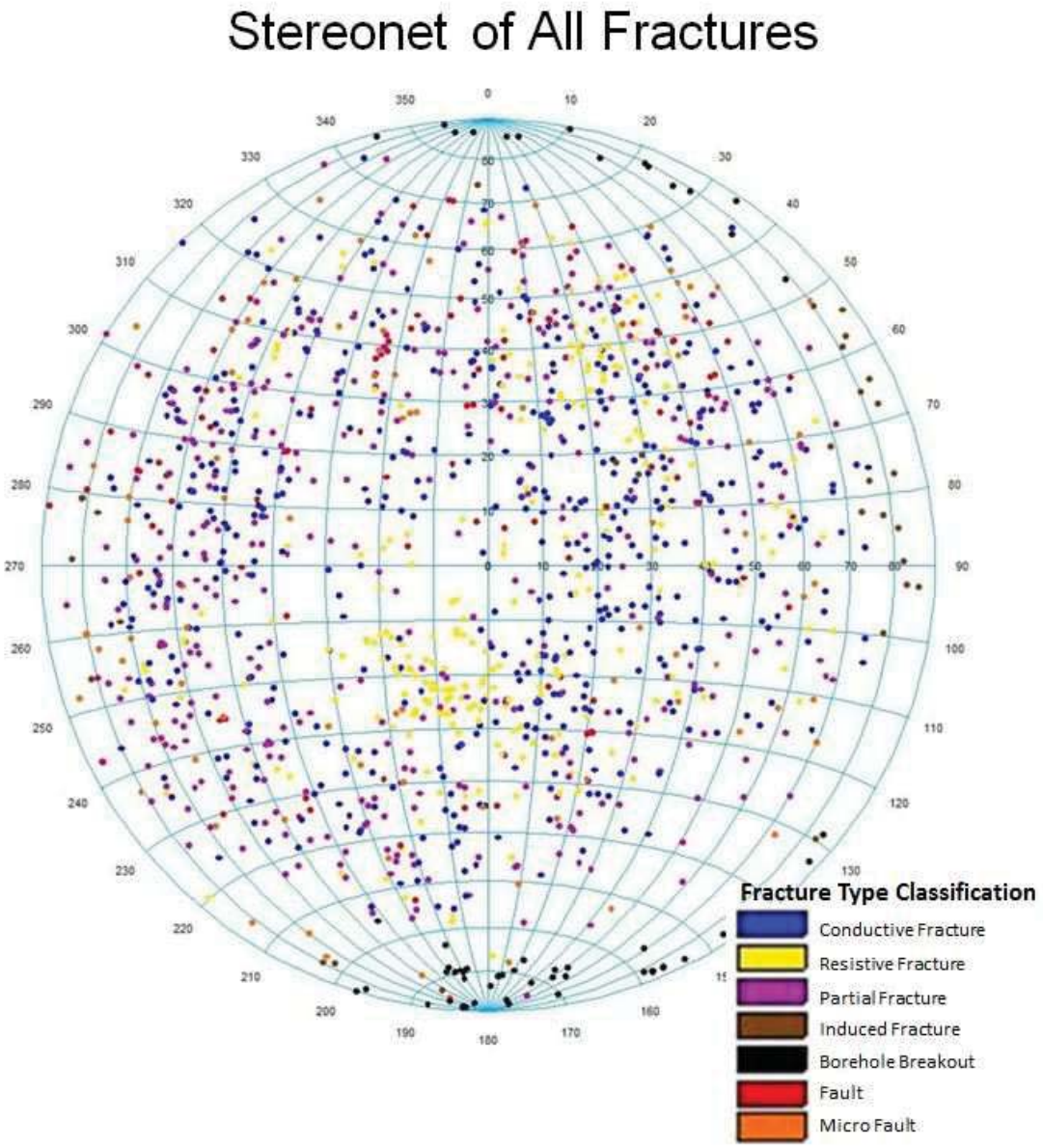

FIGURE 11. Lower hemisphere, equal-area stereonet with poles to planes for fractures and faults. Stereonets include rose frequency diagrams of strikes.

Smaller frequencies occur within 10° of this range and as well between 340° to 350° (N20°W), but these are minor in comparison to the distinctive dominant west, north-west set.

Partial fractures also have a relatively large range of fracture orientations. However, these fractures also show two dominant sets of strike orientations that occur more frequently. These sets have rosette-strike frequencies located between 280° to 300° (N60°-80°W) and between 320° to 330° (N30°-40°W) (Figure 14).

Borehole breakout fractures found in the study area display a dominant and distinctive set of fracture orientations. This dominant set is primarily striking W-E between 270° and 280° (S80°W-N80°W) (Figure 15). However, there is a smaller, but notable rosette-strike frequency set that occurs between 60° to 70° (N60°E-N70°E).

Induced fractures show two dominant orientations and one minor orientation (Figure 16). The two most dominant frequencies occur between 320° to 330° (N30°-40°W) and between 0° to 10° (N0°-10°E) azimuth. There is a gradual transition from 330° NW to 10°NE in which the number of occurrences increases towards the NE. A minor set also occurs from 290° to 300° (N30°-40°W).

The micro-faults interpreted in this study display four orientation sets. These set ranges are, in ascending order of occurrences, 300° to 310° (N40°-50°W), 60° to 70° (N60°-70°E), 350° to 360° (N0°-20°W), and 20° to 30° (N20°-30°E). There is a slightly smaller frequency set that is also observed between 270°-280° (N80°-90°W) (Figure 17).

Faults have three dominant orientation sets, which are loosely similar to sets observed with micro-faults. These sets fall between 260° to 270° (N0°-20°W), 300° to 310° (N50°-60°W), and 10° to 20° (N10°-20°E). There are also smaller frequencies

present that encompasses a broad range between 220° to 330° (S40°W-N30°W) and 0° to 30° (N0°-30°E) (Figure 18).

Petal fracture data has one distinctive set of orientations. These fractures are primarily striking north between 270° and 330° (N90°-50°W) (Figure 19). However, the most dominant range is between 280° and 300° (N60°-80°W).

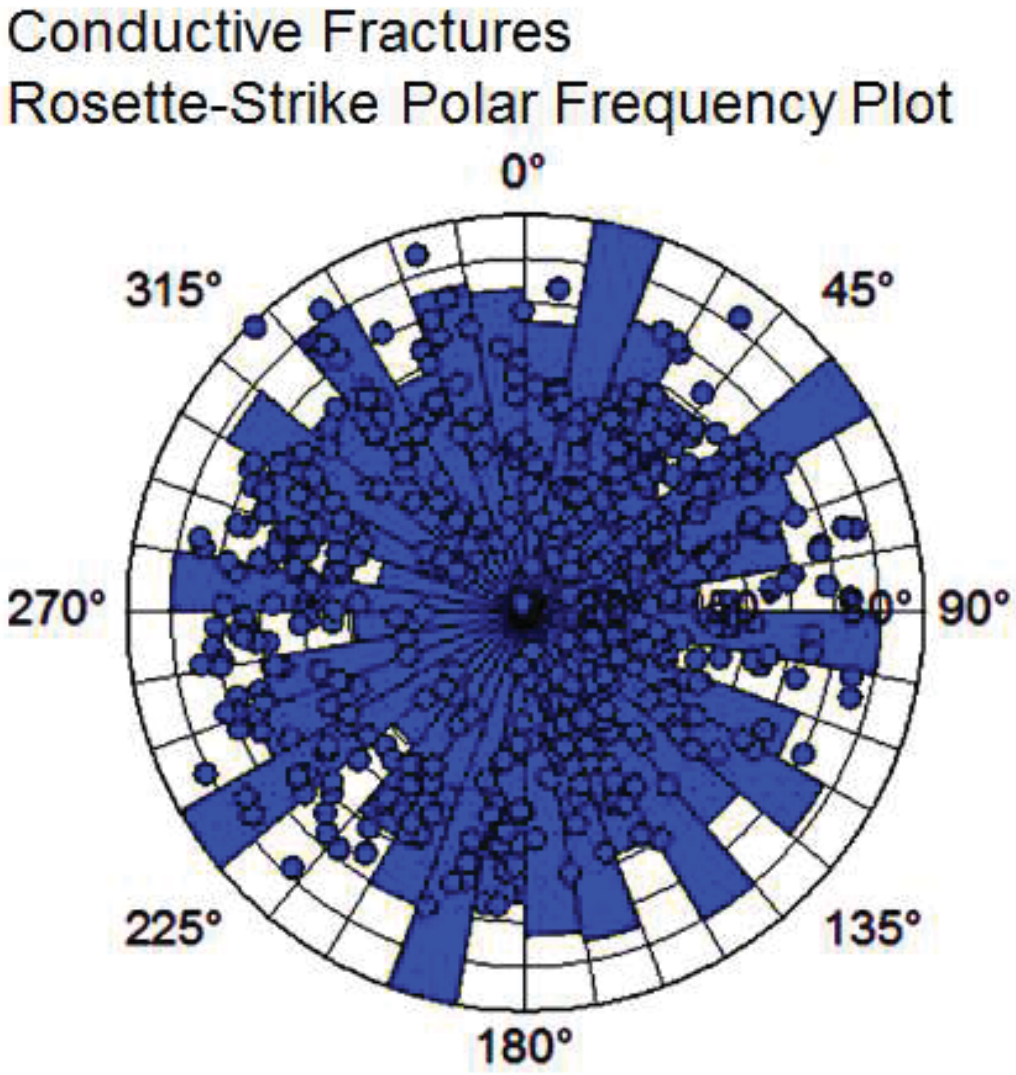

FIGURE 12. Lower hemisphere, equal-area stereonet of conductive fractures with poles to planes and rose diagrams of strikes.

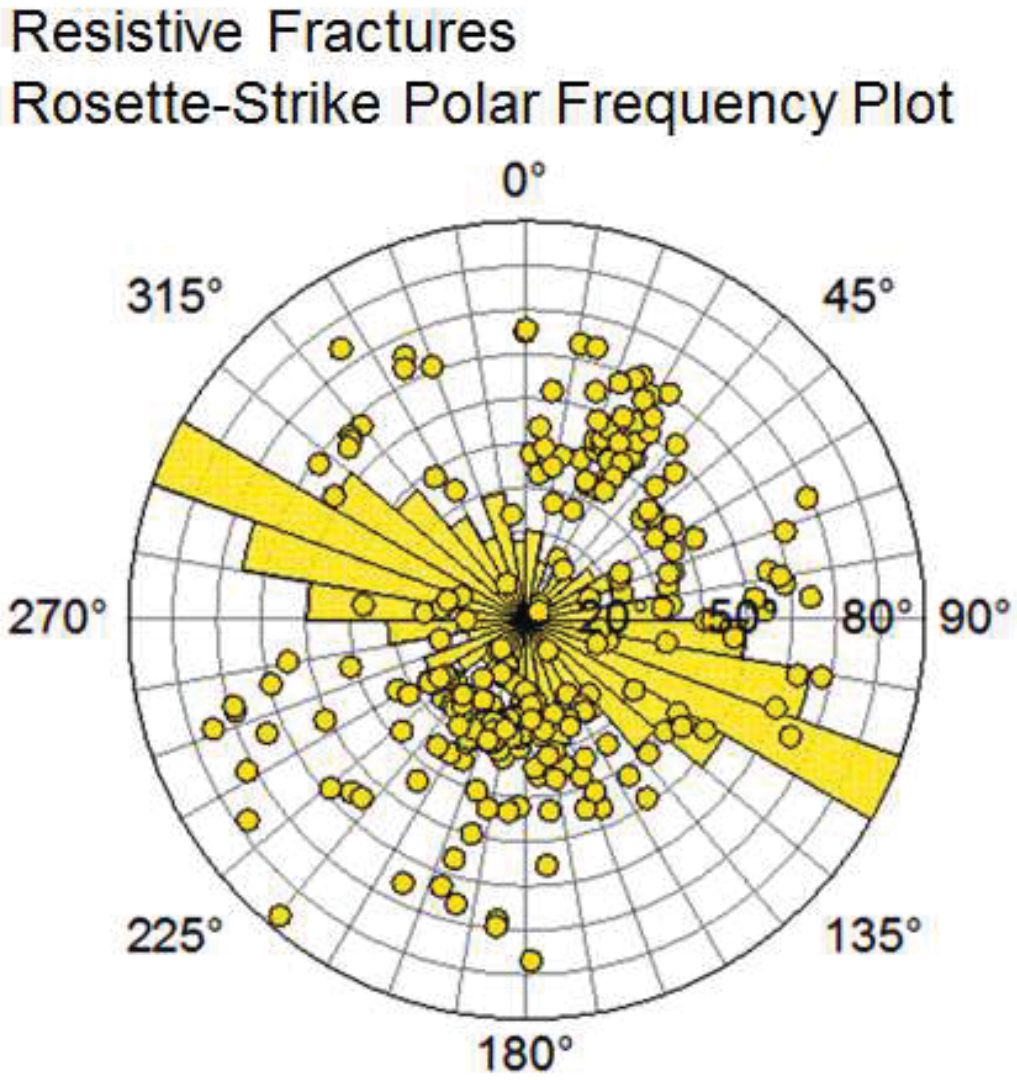

FIGURE 13. Lower hemisphere, equal-area stereonet of resistive fractures with poles to planes and rose diagram strikes

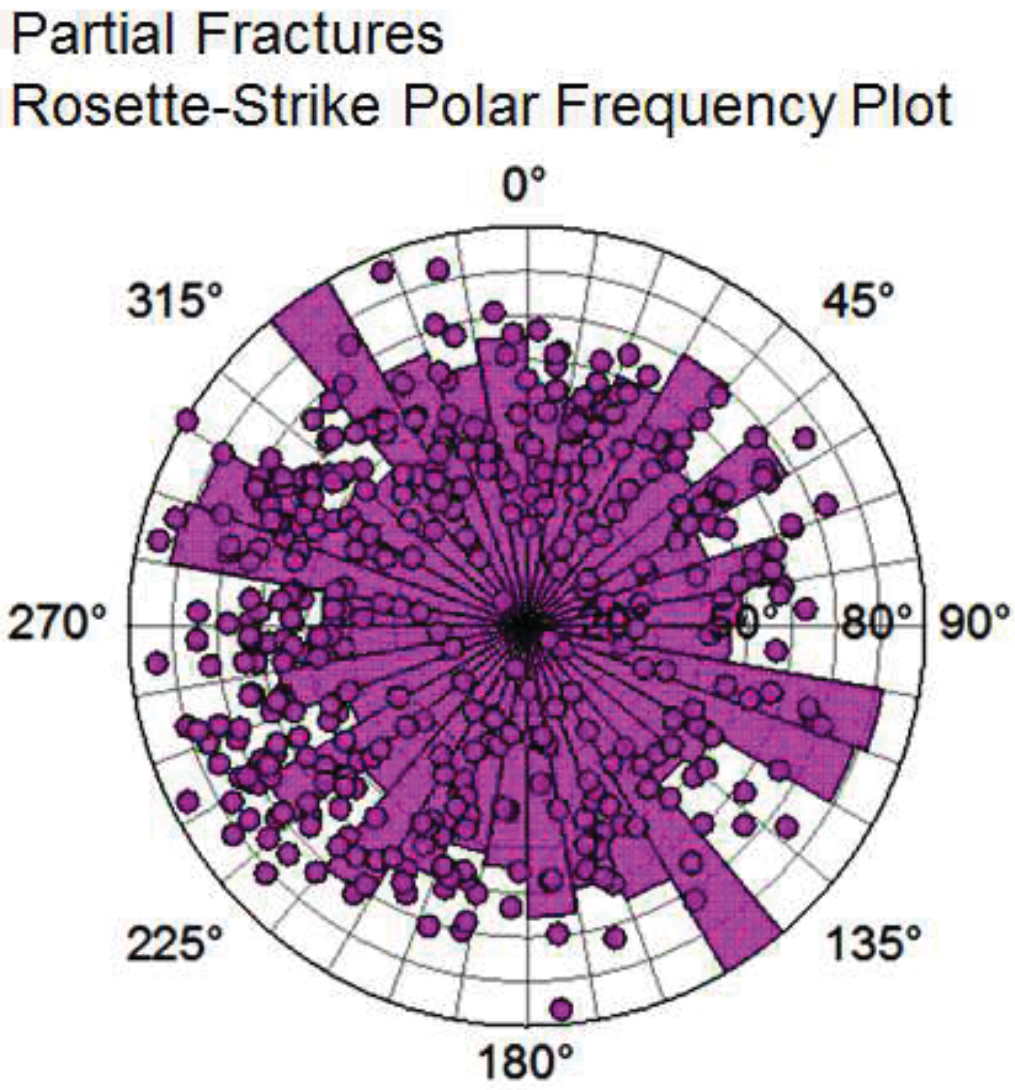

FIGURE 14. Lower hemisphere, equal-area stereonet of partial fractures with poles to planes and rose diagram strikes.

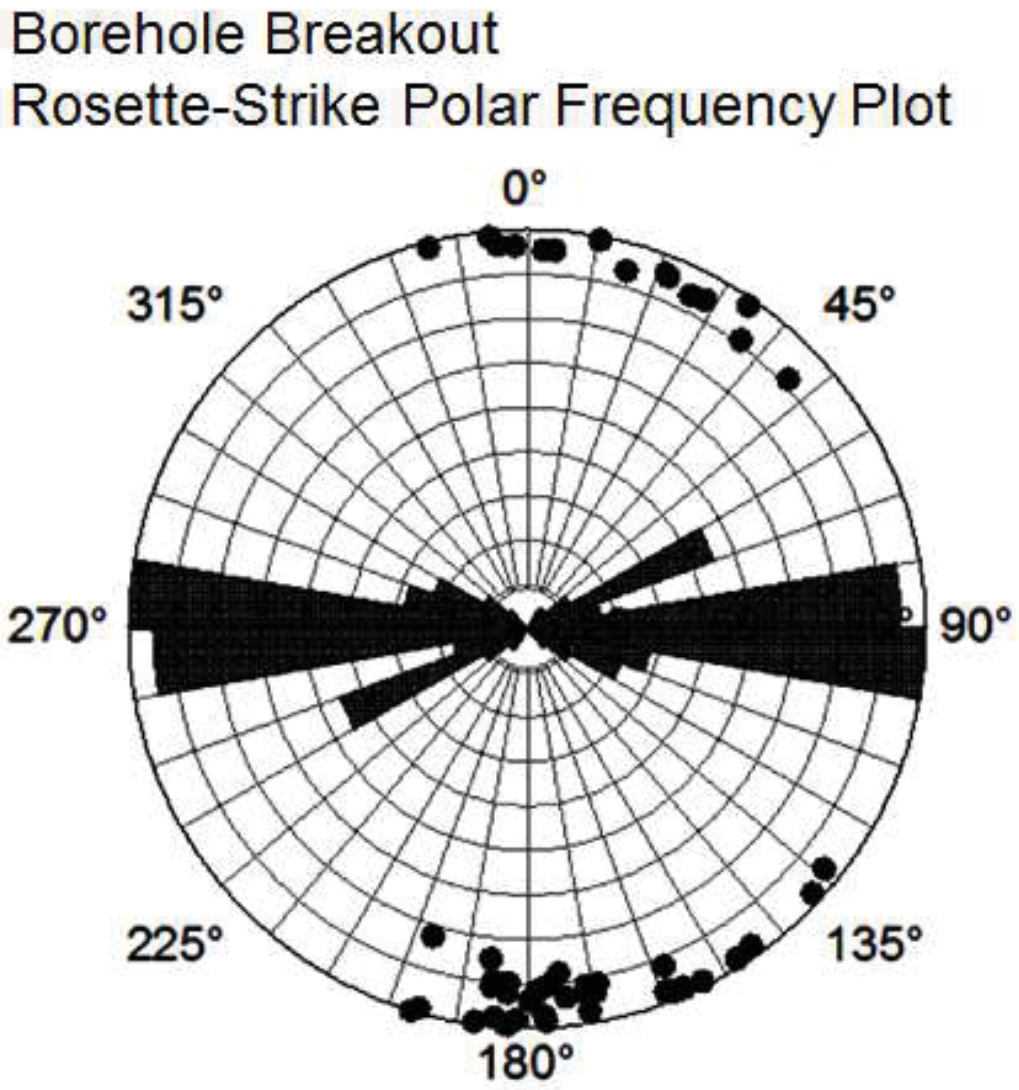

FIGURE 15. Lower hemisphere, equal-area stereonet of borehole breakouts with poles to planes and rose diagram strikes

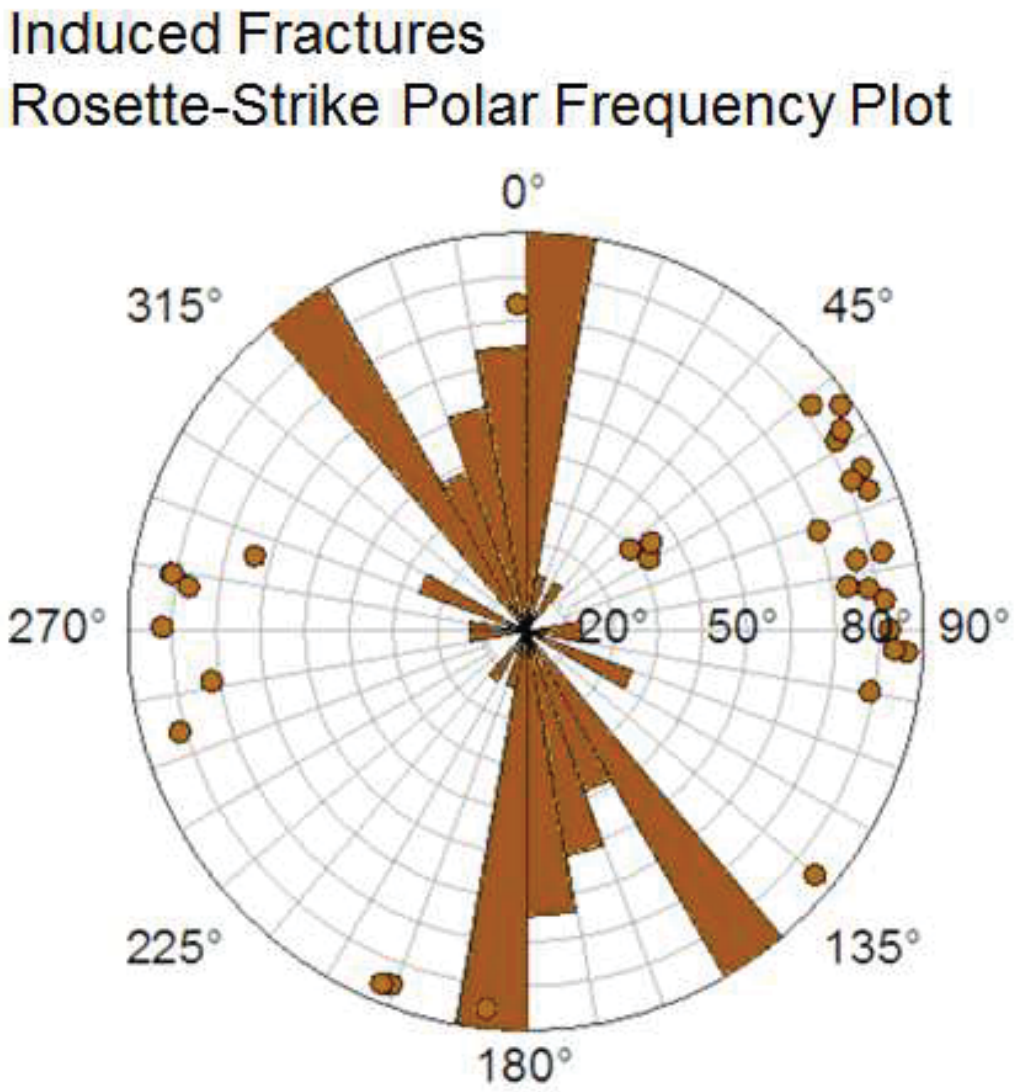

FIGURE 16. Lower hemisphere, equal-area stereonet of induced fractures with poles to planes and rose diagram strikes.

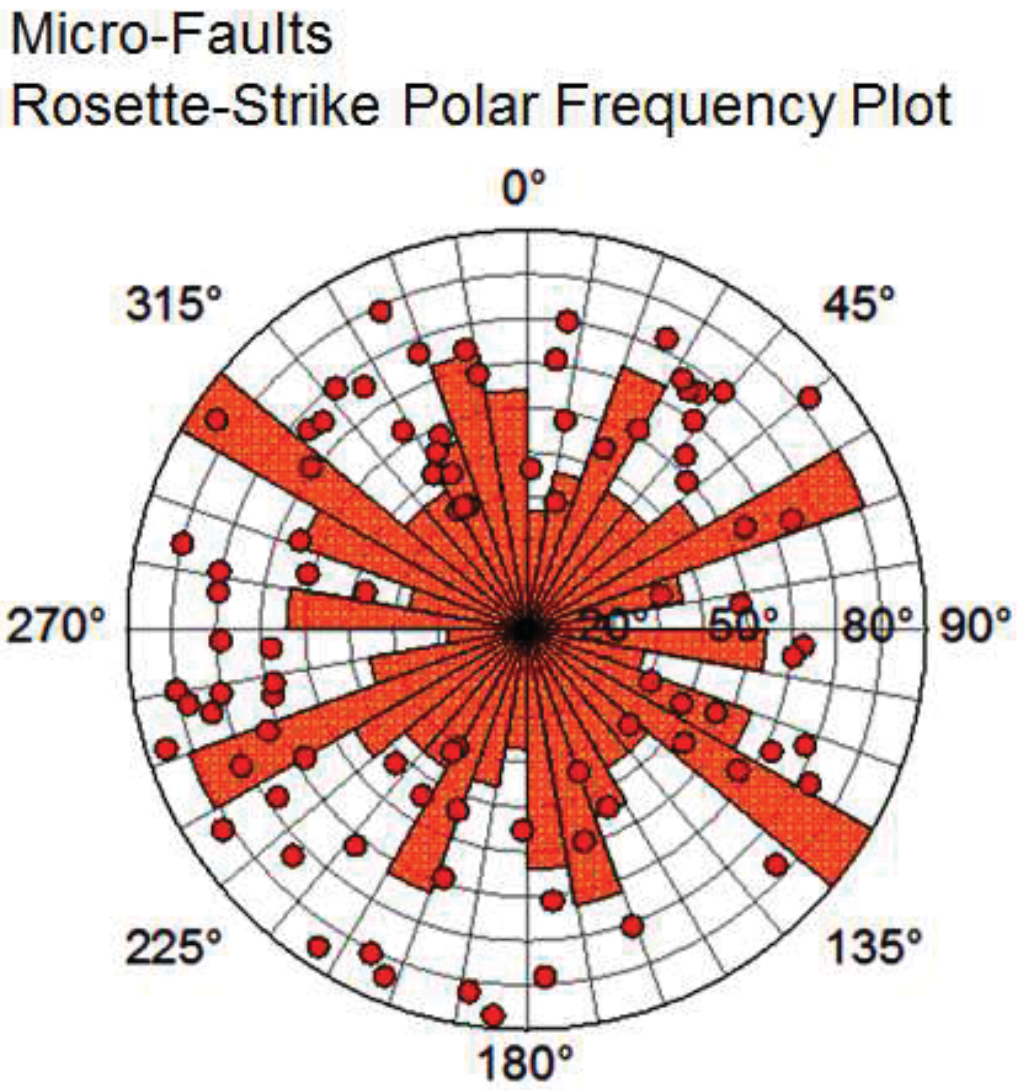

FIGURE 17. Lower hemisphere, equal-area stereonet of micro-faults with poles to planes and rose diagram strikes.

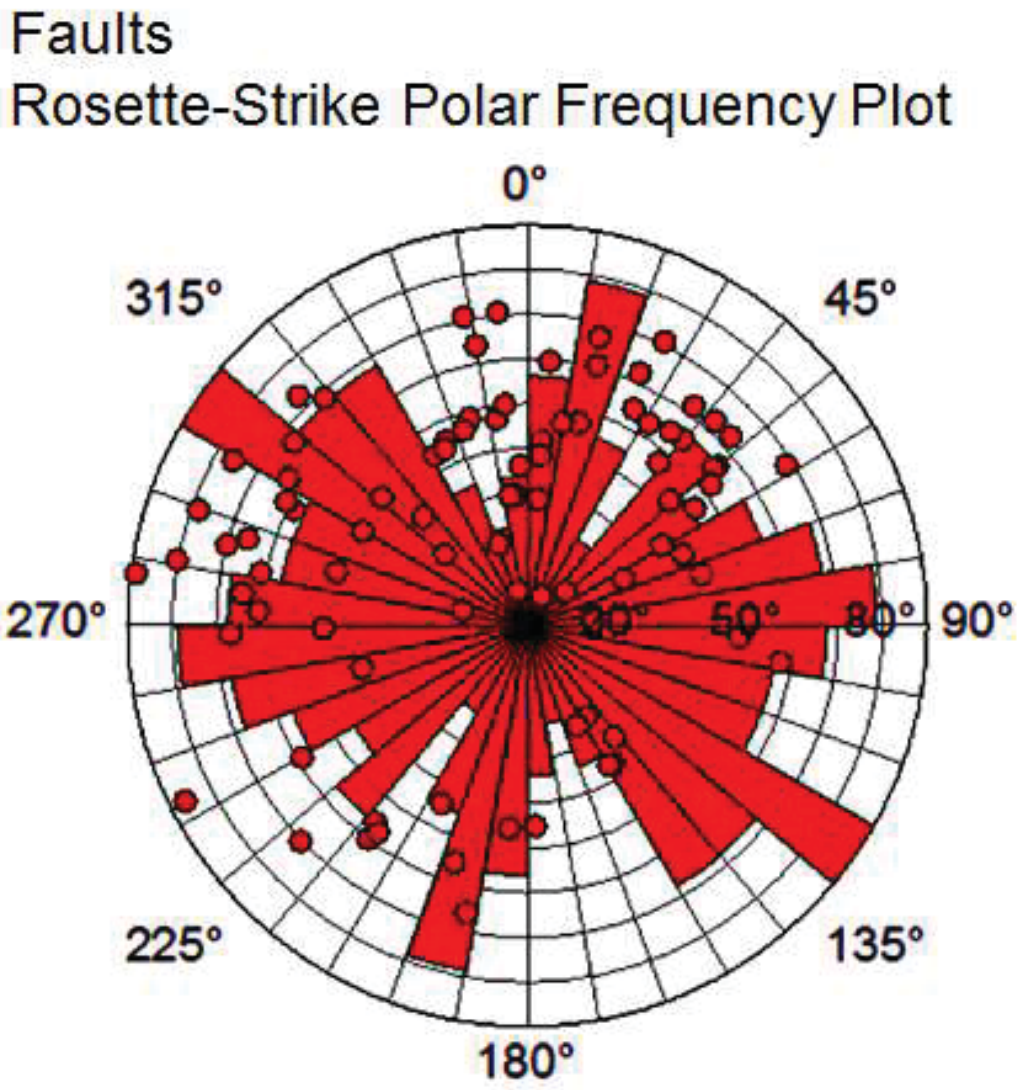

FIGURE 18. Lower hemisphere, equal-area stereonet of faults with poles to planes and rose diagram strikes.

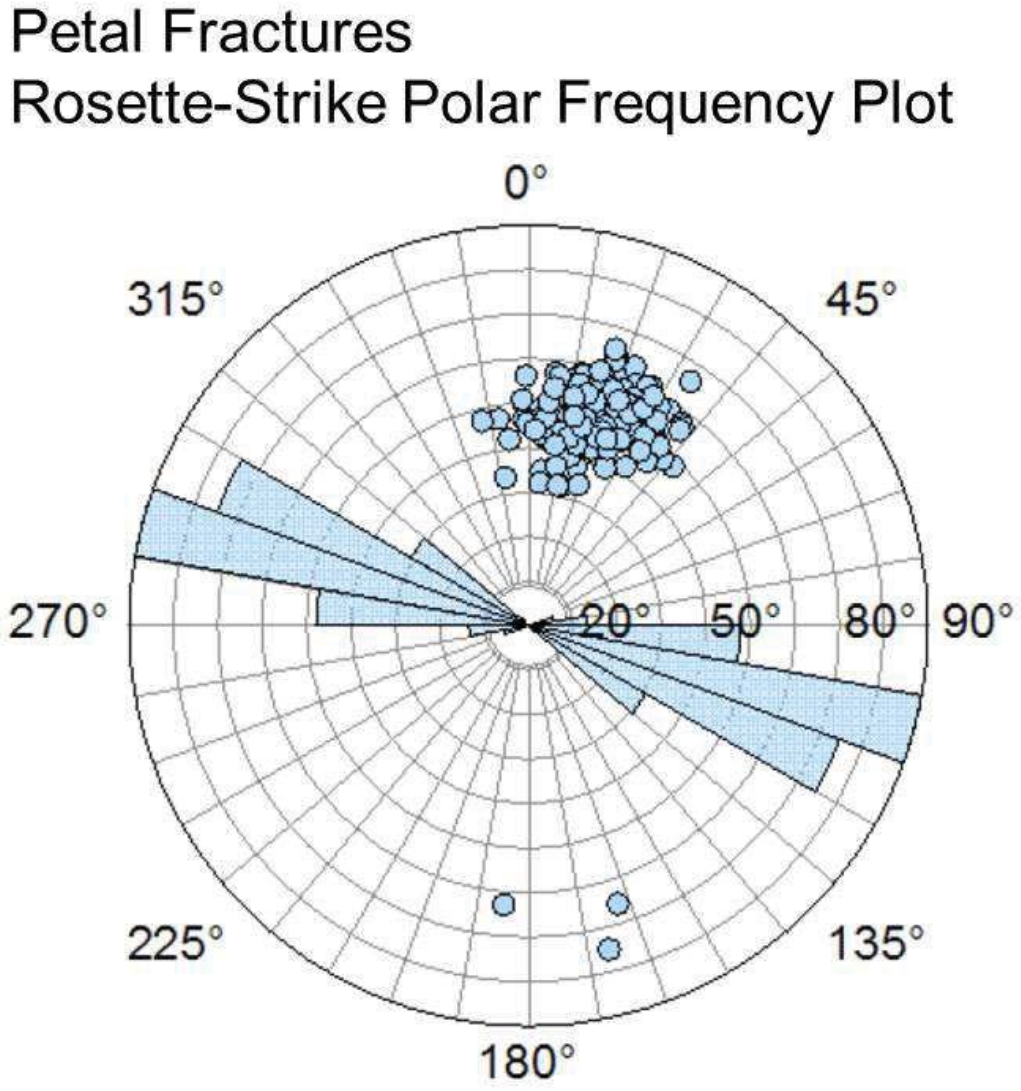

FIGURE 19. Lower hemisphere, equal-area stereonet of petal fractures with poles to planes and rose diagram strikes.

Formation Overview

Figure 20 is Schmidt stereonets of all the fracture and fault data interpreted in the Puente Formation, which is the oldest formation penetrated in this study. It shows that the data has a relatively dominant NW-SE orientation, with smaller NW and NE rosette-strike frequencies as well. The largest frequencies are found between the range of 270° to 310 ° (N90°-50°W), with the most dominant set located between 290° to 300° (N70°-60°W) azimuth. Minor rosette-strike frequencies are present between 310° to 330° (N50°-30°W), 340° to 0° (N20°-0°W), and 50° to 90° (N50°-90°W).

Figure 21 is a plot of all the fracture and fault data interpreted in the Repetto Formation. It displays great discrepancies of rosette-strike frequencies, but has dominant frequencies sets oriented towards the W and NW. There are three dominant sets that occur within 260° (S80°W) and 330° (N30°W). These sets are between 270° to 280° (N80°-90°W), 290° to 300° (N60°-70°W), and 320° to 330° (N30°-40°W). Smaller rosette-strike frequencies are fairly evenly distributed from 330° to 80° (N30°W-N80°E), with two minor set ranges that standout from 350° to360° (N0°-10°W) and 10° to 20° (N10°-20°E).

Figure 22 is Schmidt stereonets of all the fracture and fault data interpreted in the Pico Formation. The plot shows that the Pico Formation appears to have 3 major sets of rosette-strike frequencies, with the most dominant set oriented to the NW. The fracture set orientations occur between 310° to 330° (N30°-50°W), 260° to 280° (S80°W-N80°W), and 0° to 10° (N0°-10°E). The greatest occurring strike range is the first one mentioned. Minor frequencies are also observed between 330° to 350° (N10°-30°W) and 290° to 300° (N50°-70°W).

Figure 23 is a stereonet of the San Pedro Formation. The stereonet shows a dominant NE orientation of rosette-strike frequencies with three minor trends spread across other coordinates. The greatest range of frequencies is seen between 80° to 50° (N50°-80°E), with the most dominant set observed between 60° to 70° (N60°-70°E) azimuth. Minor fracture frequencies occur between 50° to 0° (N0°-50°E), 350° to 320° (N10°-40°W), and 310° to 270° (N50°-90°W) azimuth.

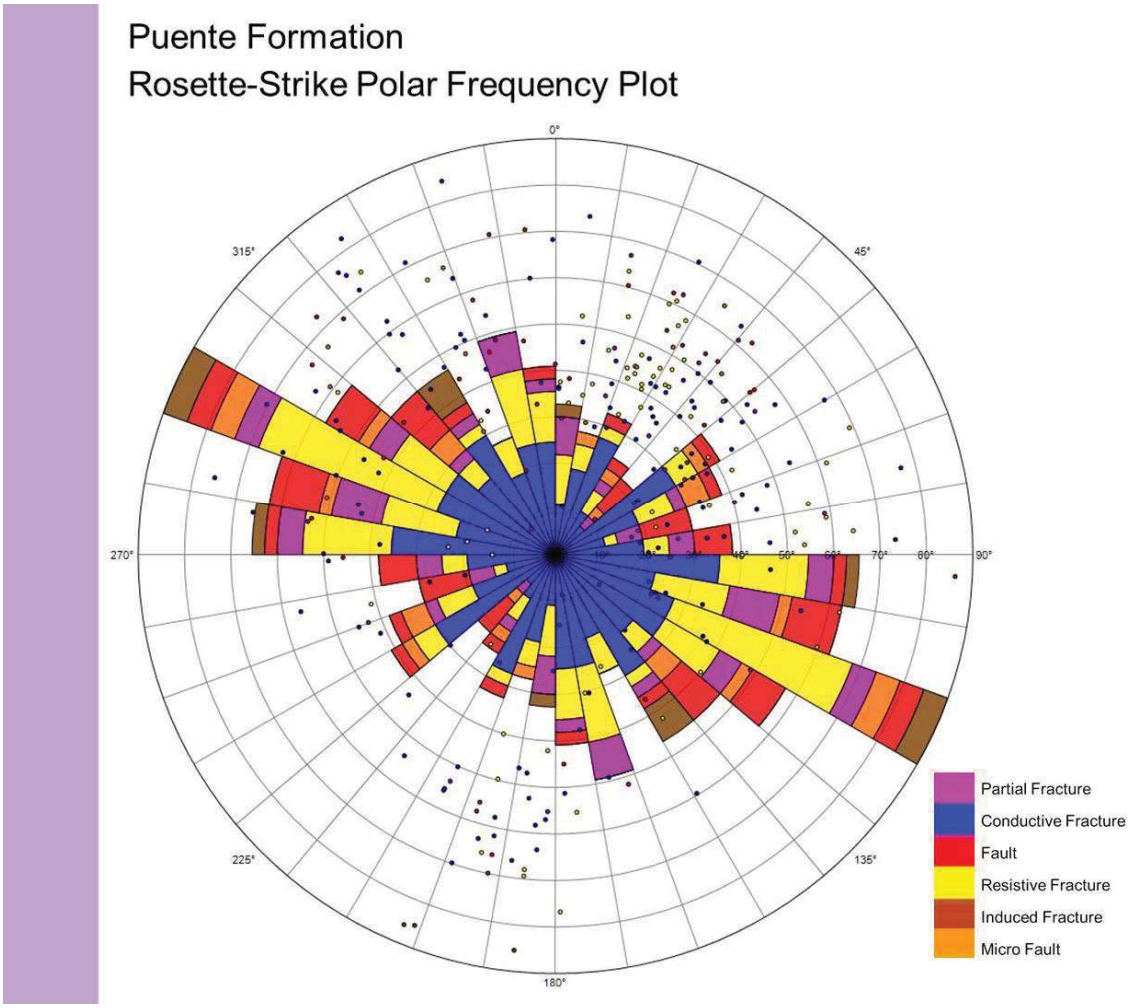

FIGURE 20. Lower hemisphere, equal-area stereonet of fractures and faults in the Puente Formation with poles to planes and rose diagram strikes.

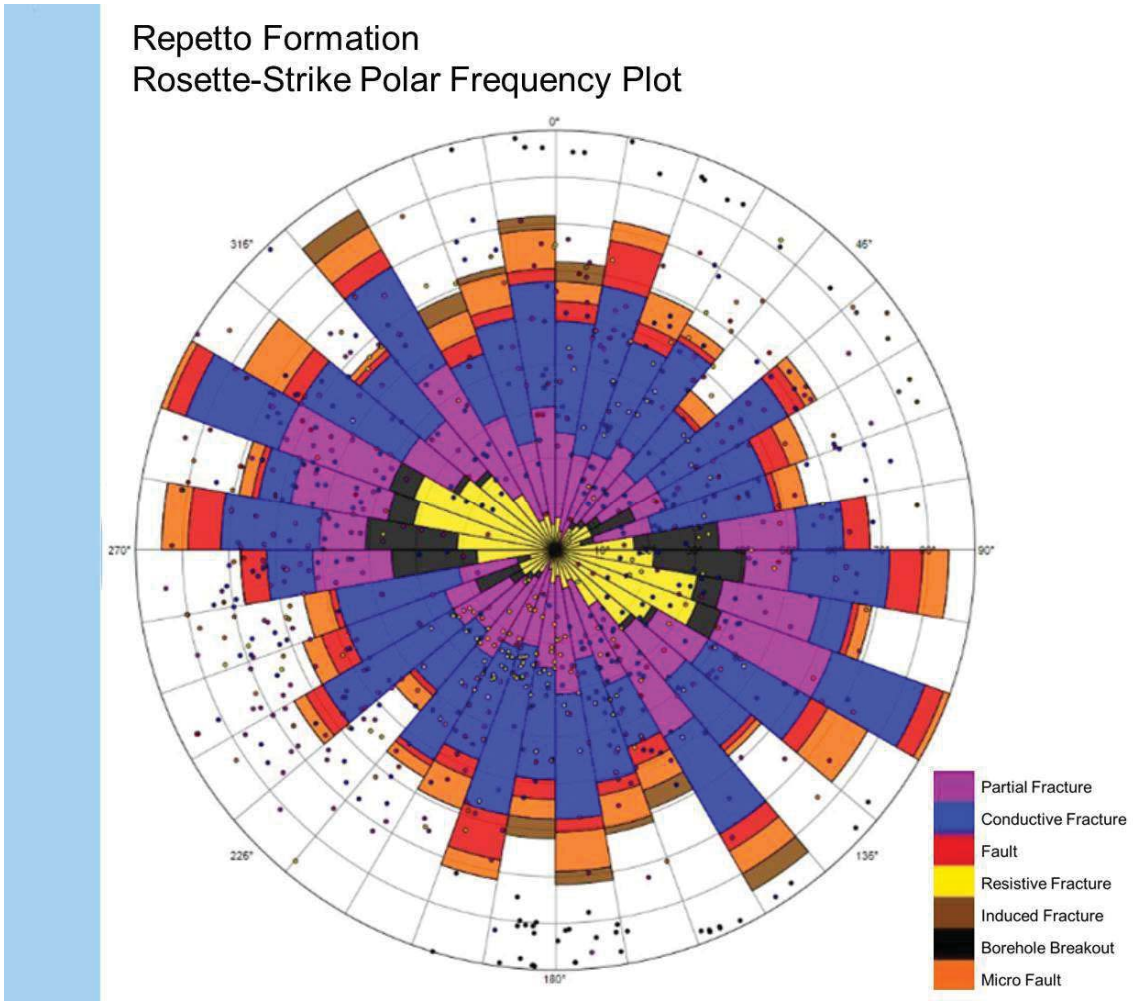

FIGURE 21. Lower hemisphere, equal-area stereonet of fractures and faults in the Repetto Formation with poles to planes and rose diagram strikes.

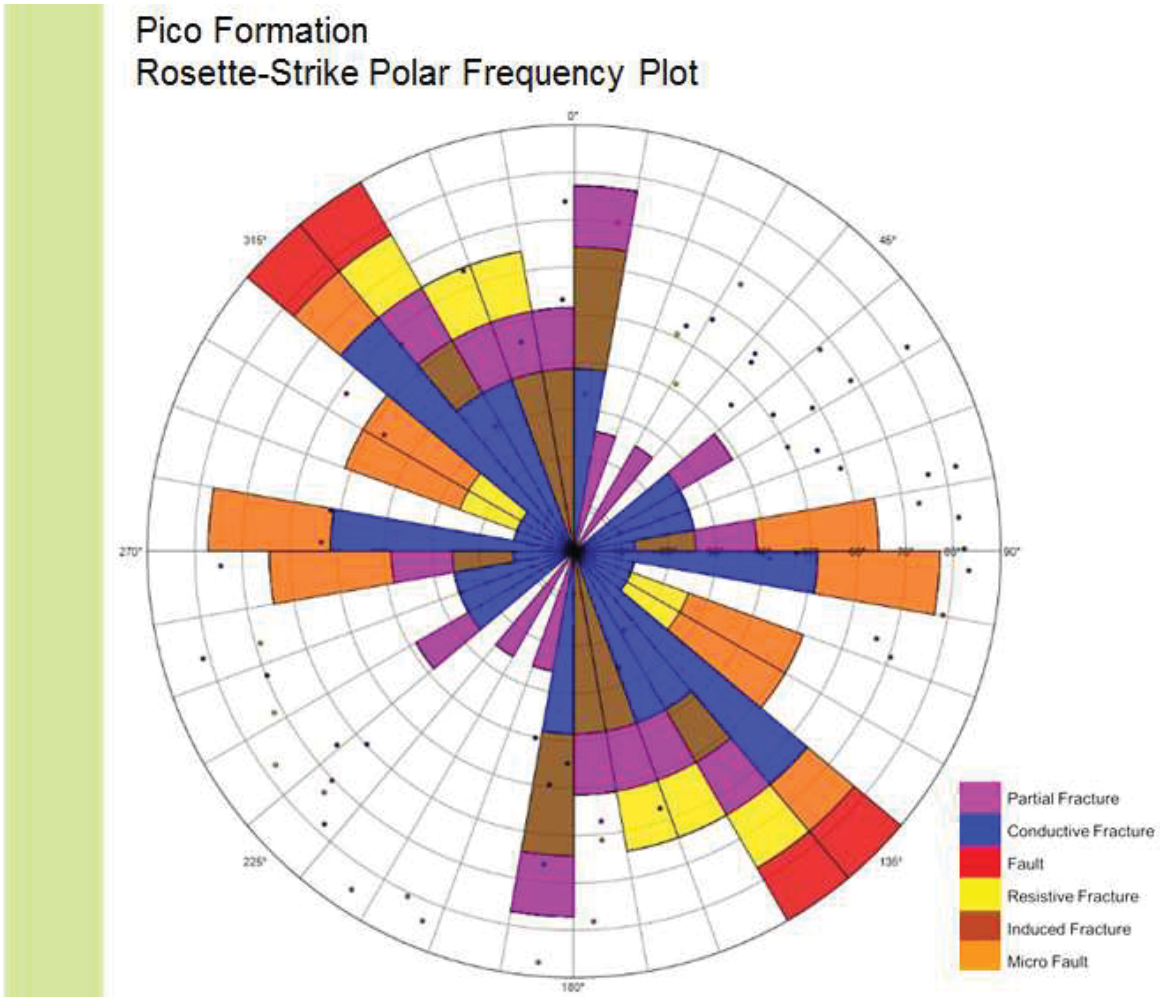

FIGURE 22. Lower hemisphere, equal-area stereonet of fractures and faults in the Pico Formation with poles to planes and rose diagram strikes.

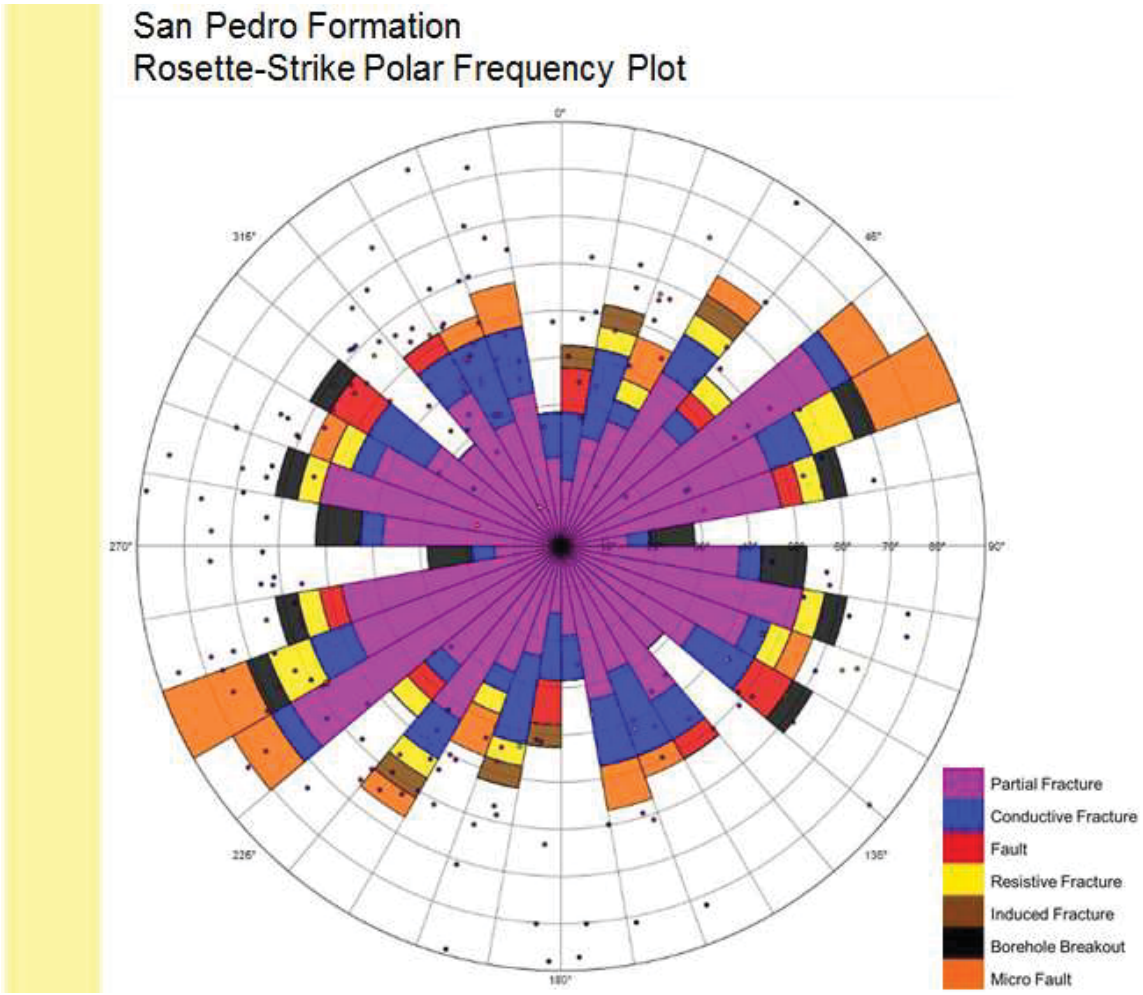

FIGURE 23. Lower hemisphere, equal-area stereonet of fractures and faults in the San Pedro Formation with poles to planes and rose diagram strikes

Formations and Fracture Type Sets

This section describes the results observed for the individual fracture types found within the each formation. The results will be described from the oldest formation to the youngest formation. Fracture types will be described in the following order: conductive fractures, resistive fractures, partial fractures, borehole breakout, induced fractures, micro-faults, and faults. Figure 24 shows an overview of Schmidt stereonets for each fracture type in each formation.

Puente Formation. This section describes the results observed for the individual fracture types found within the Puente Formation. Six groups of fracture types will be discussed, which include conductive fractures, resistive fractures, partial fractures, induced fractures, micro-faults, and faults. There was no borehole breakout found in wells that penetrated the Puente Formation.

Figure 25 shows a Schmidt stereonet of the conductive fracture interpreted in the Puente Formation. It displays a broad range of closely spaced frequencies to the W-NW, with four sets of fracture rosette-strikes that stand above the rest. The most commonly occurring broad range of orientations are located between 270° to 360° (N90°-0°W). The most dominant set is found within this range between 270° to 280° (N80°-90°W). The other significant sets of conductive fractures observed in the Puente Formation are between 320° to 330°(N30°-40°W), 20° to 30° (N20°-30°E), and 50° to 60° (N50°-60°E).

On the other hand, resistive fractures (Figure 26) observed in the Puente Formation have one dominant set range that strikes W-NW and located between 290°-300° (N60°-70°W) . There are minor rosette-strike frequencies that neighbor the

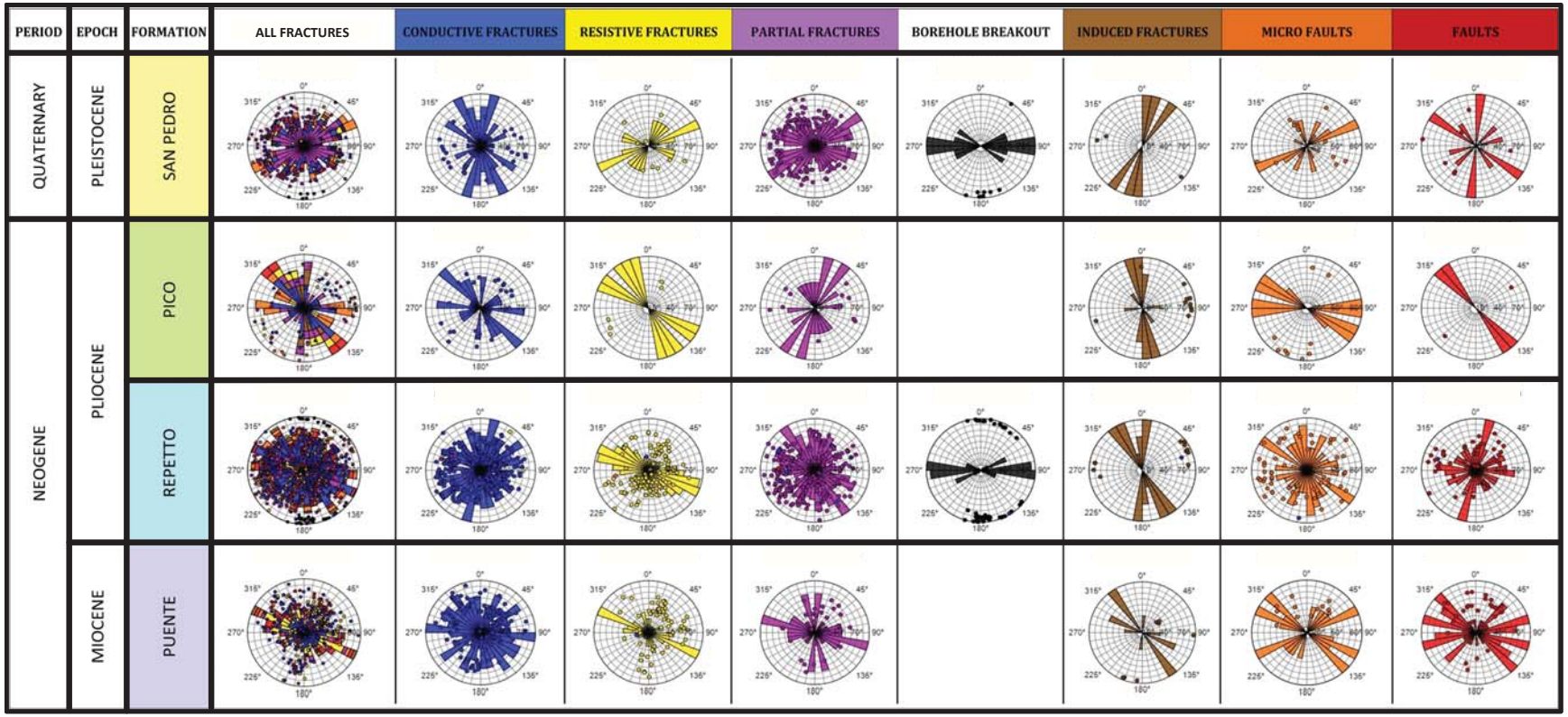

FIGURE 24. Overview of fracture types plotted in stereonets for each formation. Stereonets are lower hemisphere, equal-area with poles to fracture or fault plane and rose diagram strikes.

dominant set between 270° to 310° (N50°-90°W), and to the N between 340°-10° (N0°2W- N10°E). However, partial fractures found in the Puente Formation appear to have three sets of strike frequency ranges. These set ranges are located at 280°-290° (N80°-90°W), 340°-350° (N10°-20°W), and 0°-10° (N0°-10°E) (Figure 27).

There were no borehole breakouts present in the Puente Formation, but there are seven induced fractures that plot four rosette-strikes frequency and show a dominant NW set of fractures strikes (Figure 28). These strike orientations are between 320 to 230 (N30-40W), 290 to 300 (N60-70W), 0 to 10 (N0-10E), and 270 to 260 (N80-90W). They are described above, in descending order from the most dominant set to minor frequencies.

Figures 29 and 30 are Schmidt stereonets of all the micro-faults and faults interpreted in the Puente Formation. There are three dominant micro-fault sets with rosette-strikes frequencies between 290° to 300° (N60°-70°W), 310° to 320° (N40°-50°W), and 60° to 70° (N60°-70°E) azimuth. Additionally, it should be noted that when minor frequencies are examined micro-faults are split between NW and NE strikes.

Faults interpreted in the Puente Formation are relatively split into east-west strikes with little data found in the N-S direction. There are four sets of frequency ranges that stand out from the rest. They are between 220°-230° (S40°-50°W), 250°-270° (S70°-90°W), 280°-290° (N80°-70°W), and 310°-320° (N40°-50°W).

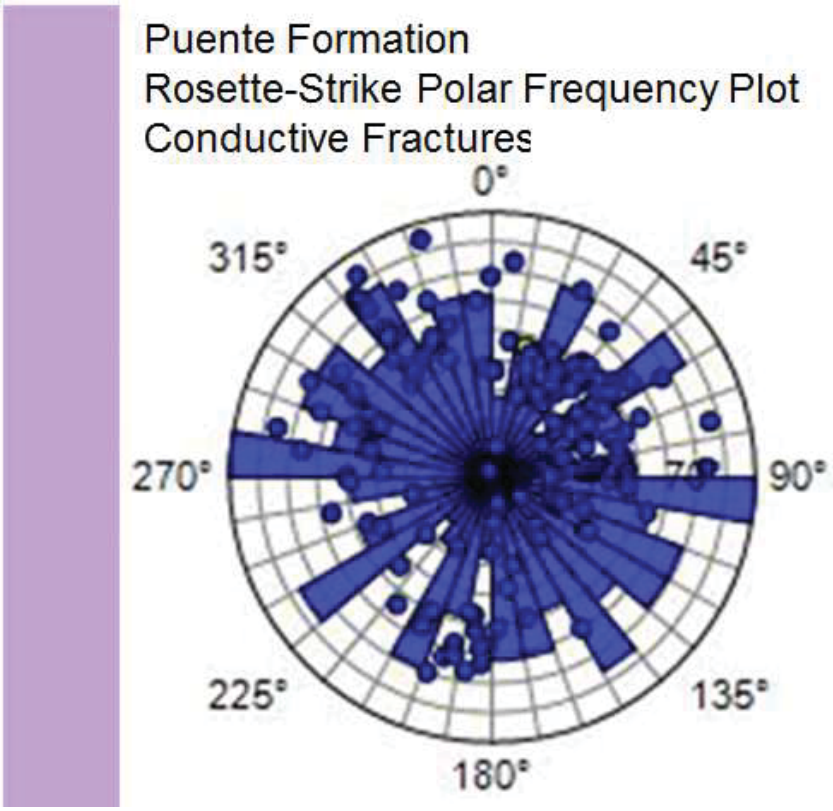

FIGURE 25. Lower hemisphere, equal-area stereonet of conductive fractures in the Puente Formation with poles to planes and rose diagram strikes.

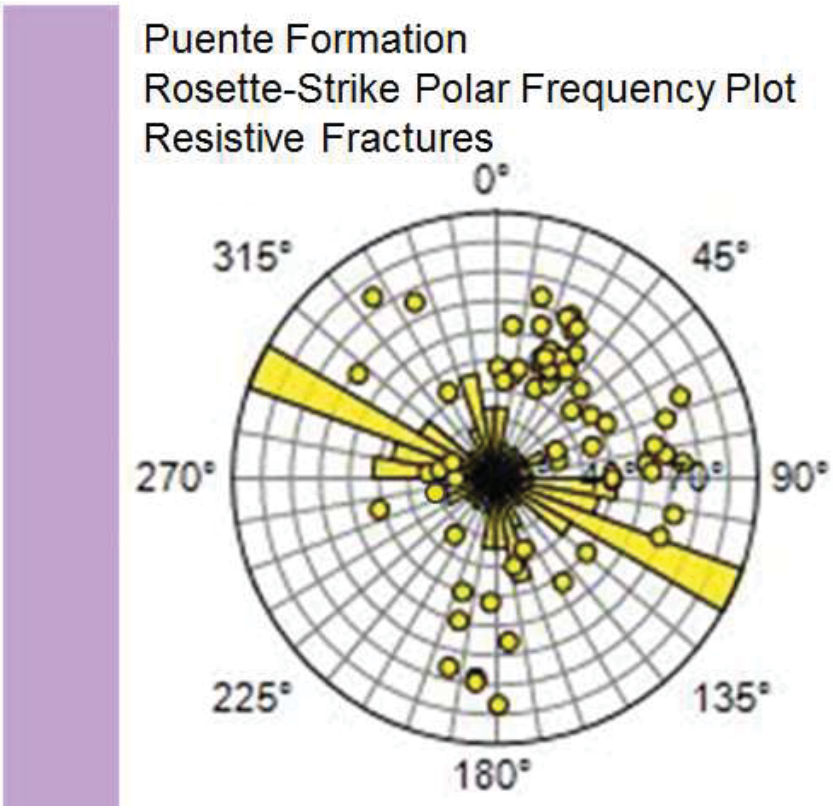

FIGURE 26. Lower hemisphere, equal-area stereonet of resistive fractures in the Puente Formation with poles to planes and rose diagram strikes.

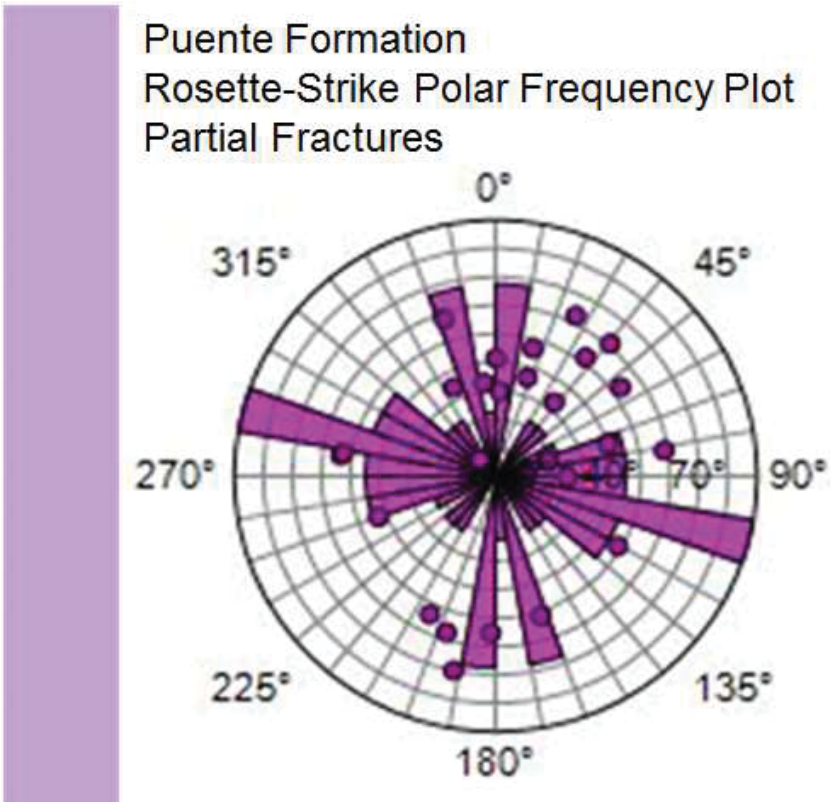

FIGURE 27. Lower hemisphere, equal-area stereonet of partial fractures in the Puente Formation with poles to planes and rose diagram strikes.

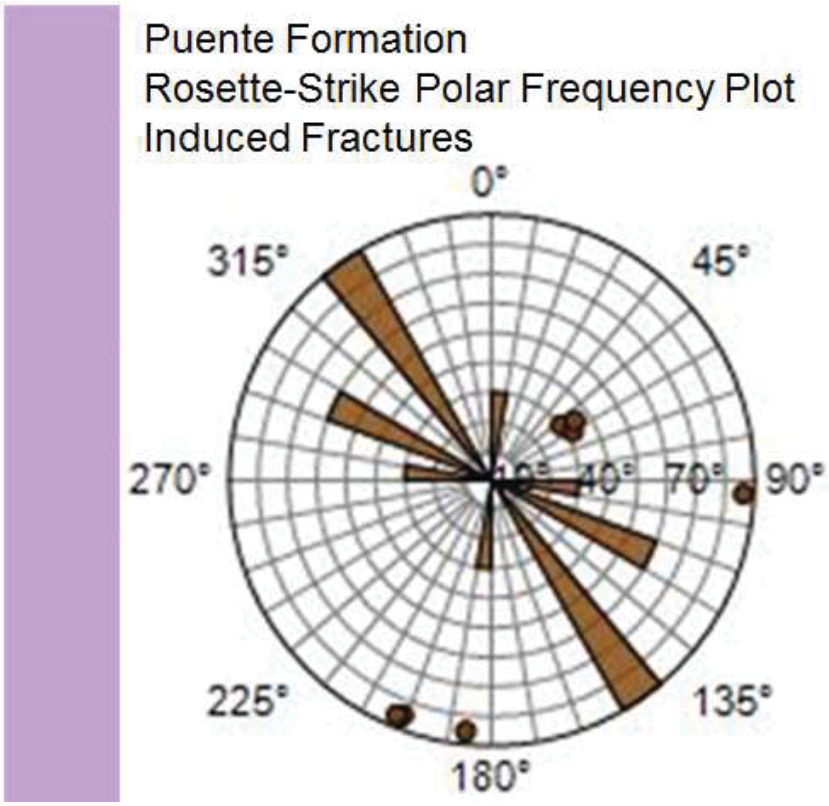

FIGURE 28. Lower hemisphere, equal-area stereonet of induced fractures in the Puente Formation with poles to planes and rose diagram strikes.

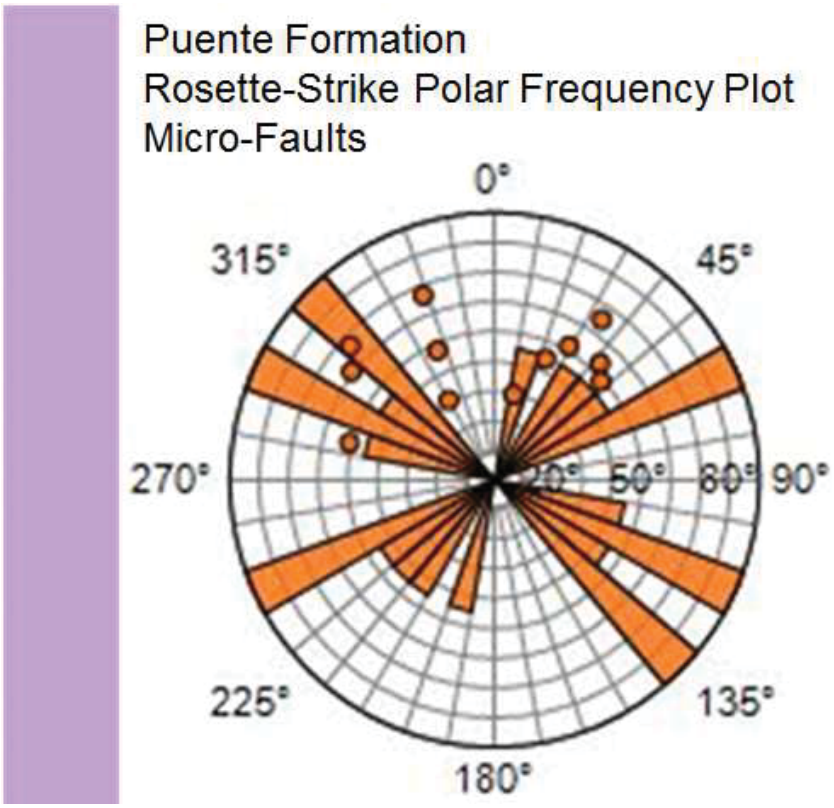

FIGURE 29. Lower hemisphere, equal-area stereonet of micro-faults in the Puente Formation with poles to planes and rose diagram strikes.

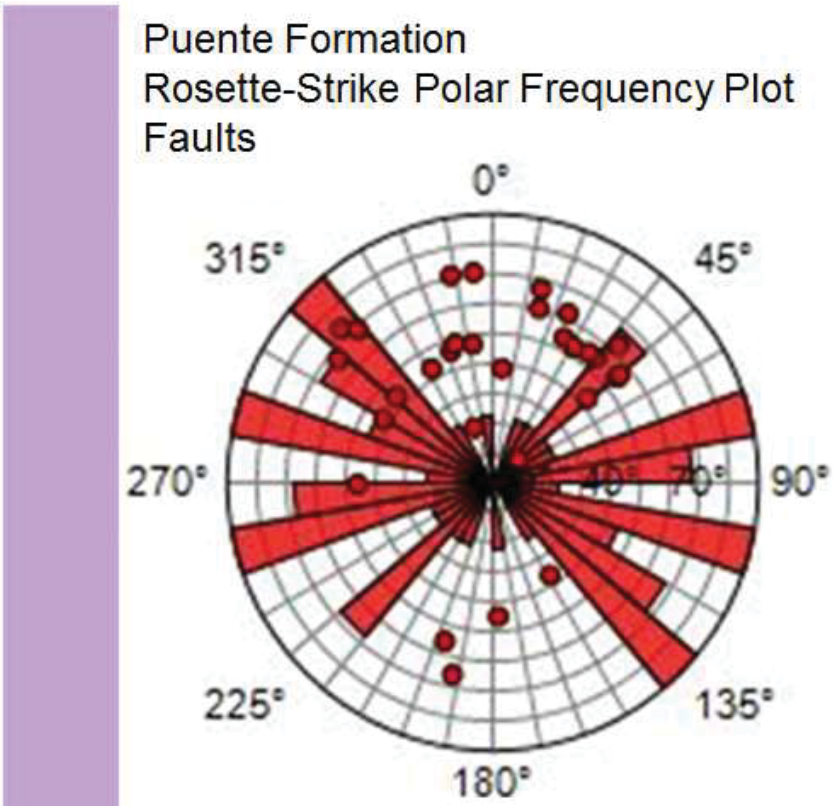

FIGURE 30. Lower hemisphere, equal-area stereonet of faults in the Puente Formation with poles to planes and rose diagram strikes.

Repetto Formation. This section describes the results observed for the individual fracture types found within the Repetto Formation. All seven fracture types are present in this formation and their results will be described in the following order: conductive fractures, resistive fractures, partial fractures, borehole breakout, induced fractures, micro-faults, and faults.

Figure 31 shows a Schmidt stereonets of the conductive fracture interpreted in the Puente Formation. It displays a large range of relatively closely spaced frequencies throughout the plot, but shows at least two sets of strike orientations that occur more frequently. These two sets have strike orientations between 10°-20° (N10°-20°E) and between 50°-60° (N50°-60°E).

Conversely, resistive fractures in the Repetto Formation are primarily striking E-W between 260° and 330° (S80°W-N30°W) (Figure 32). The dominant set range of strikes occurs between 280° and 300° (N60°-80°W). On the other hand, partial fractures display a greater assortment of orientations, but have a dominant set from 320° to 330° (N30°-40°W) (Figure 33).

Figure 34 is a plot of borehole breakout data interpreted in the Repetto Formation. Borehole breakout fractures in the Repetto Formation show one dominant and one minor set of strike rosette-strikes frequencies. The dominant range is oriented W-E between 260° and 280° (S80°W-N80°W). There is a smaller, but notable set that occurs also between 60°-70° (N60°E-N70°E). The borehole breakout from the Repetto Formation encompasses 86 % of the total borehole breakout data found throughout this study.

Figures 35 shows a plot of all the induced fractures interpreted in the Repetto Formation. These fractures have two dominant sets of orientations. They are 320° to

340° (N20°-40°W) and 0° to 10° (N0°-10°E). There is a smaller, but notable set that occurs between 350°-360° (N80°-90°W) that bounds the N striking dominant set.

Figures 36 and 37 are Schmidt stereonets of all the micro-faults and faults interpreted in the Puente Formation. Micro-faults display three sets of relatively higher strike frequencies. These sets range, in ascending order, between 300°-310° (N40°-50°W), 340°-360° (N0°-30°W), and 20°-30° (N20°-30°E). There are a few minor sets scattered throughout the stereonet as well.

Faults, on the other hand, show one dominant N-NE set of orientations. This set occurs between 10° to 20° (N10°-20°E). There is smaller range of frequencies between 270°-280° (N80°-90°W) that is slightly larger than the other minor frequencies.

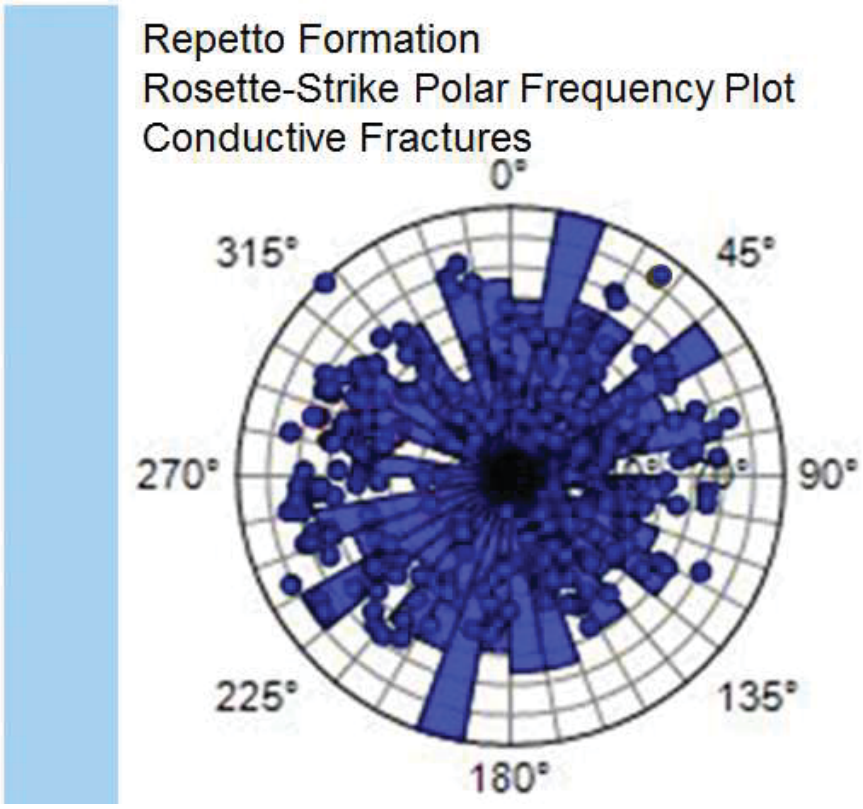

FIGURE 31. Lower hemisphere, equal-area stereonet of conductive fractures in the Repetto Formation with poles to planes and rose diagram strikes.

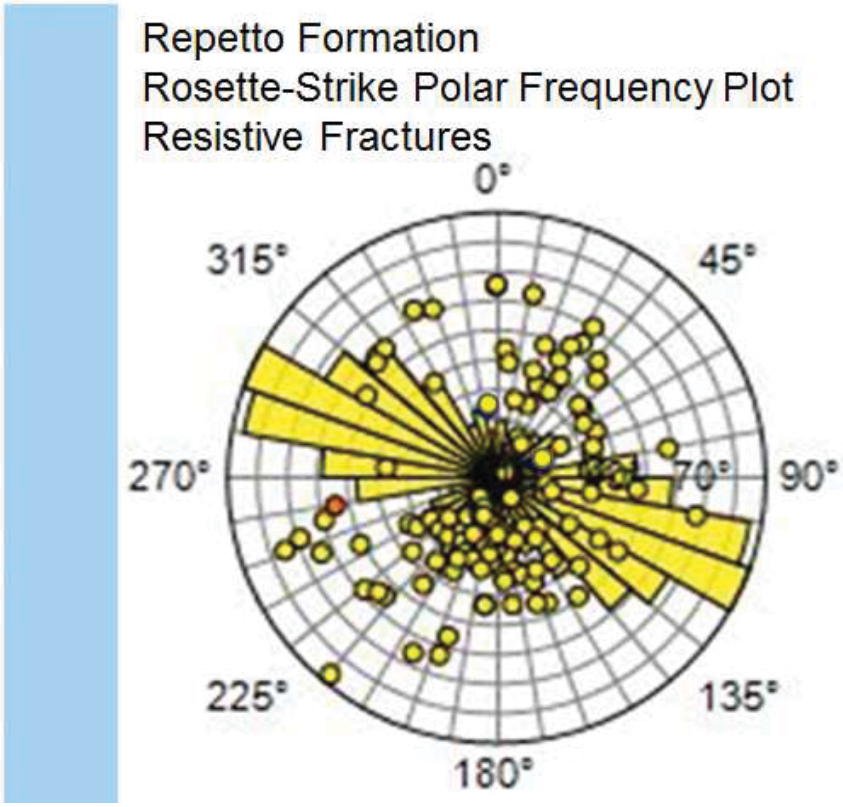

FIGURE 31. Lower hemisphere, equal-area stereonet of resistive fractures in the Repetto Formation with poles to planes and rose diagram strikes.

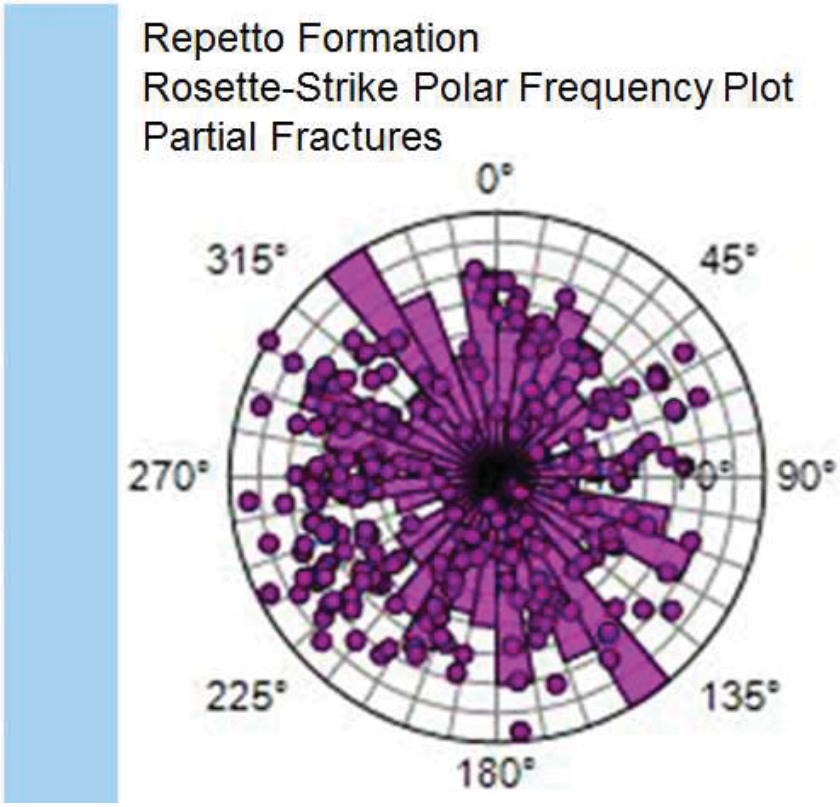

FIGURE 33. Lower hemisphere, equal-area stereonet of partial fractures in the Repetto Formation with poles to planes and rose diagram strikes.

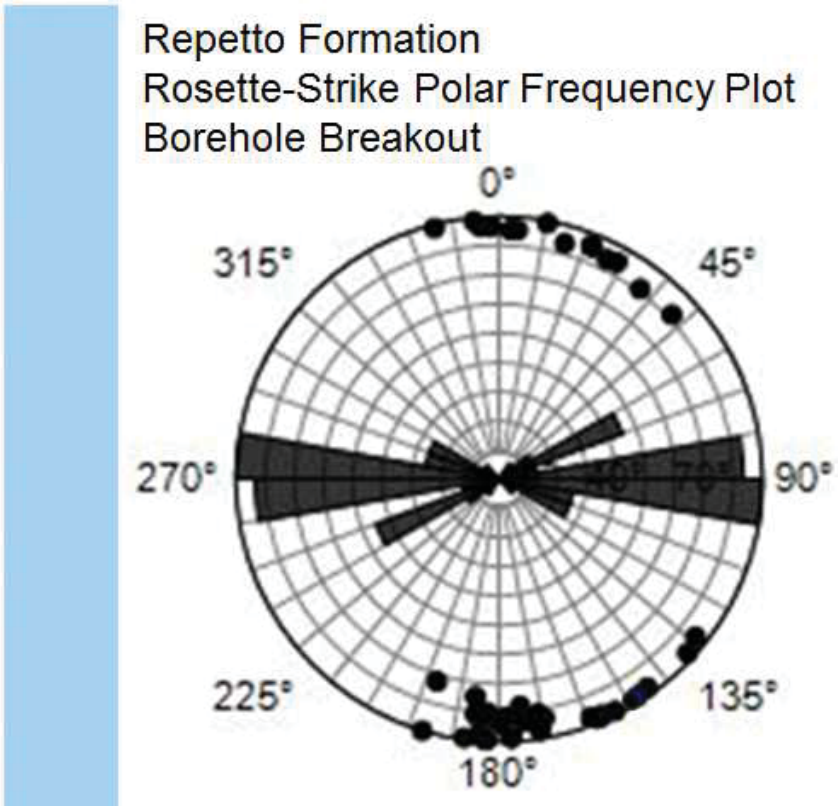

FIGURE 34. Lower hemisphere, equal-area stereonet of borehole breakouts in the Repetto Formation with poles to planes and rose diagram strikes.

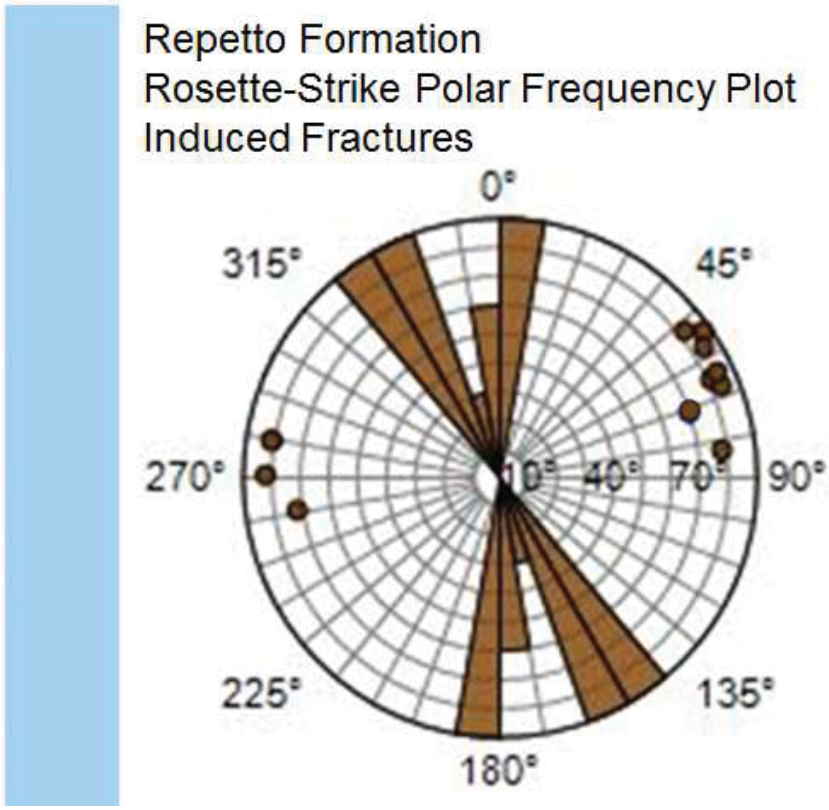

FIGURE 35. Lower hemisphere, equal-area stereonet of induced fractures in the Repetto Formation with poles to planes and rose diagram strikes.

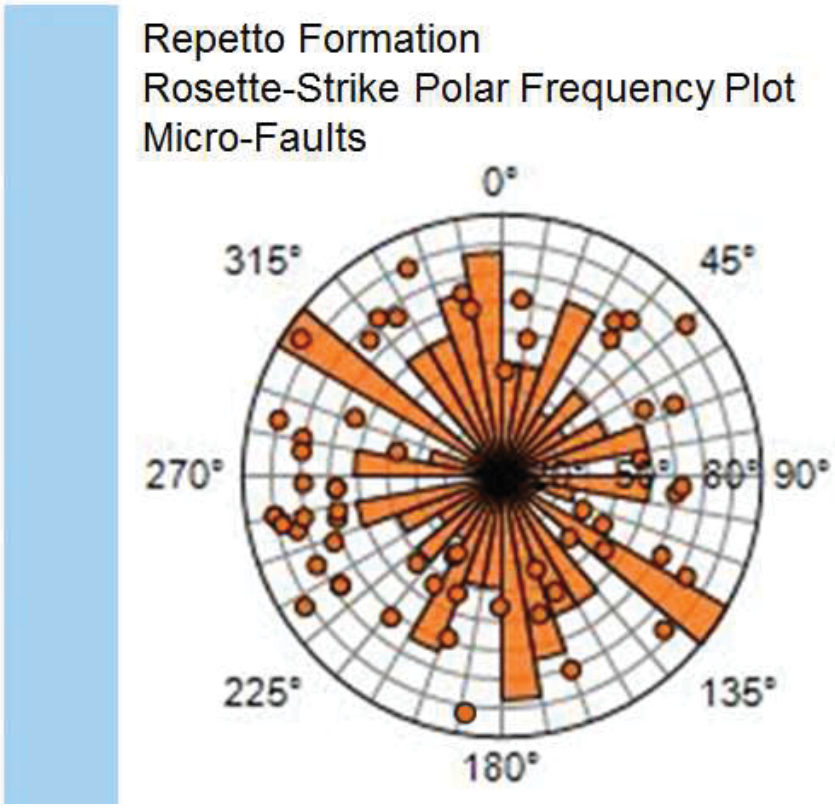

FIGURE 36. Lower hemisphere, equal-area stereonet of micro-faults in the Repetto Formation with poles to planes and rose diagram strikes.

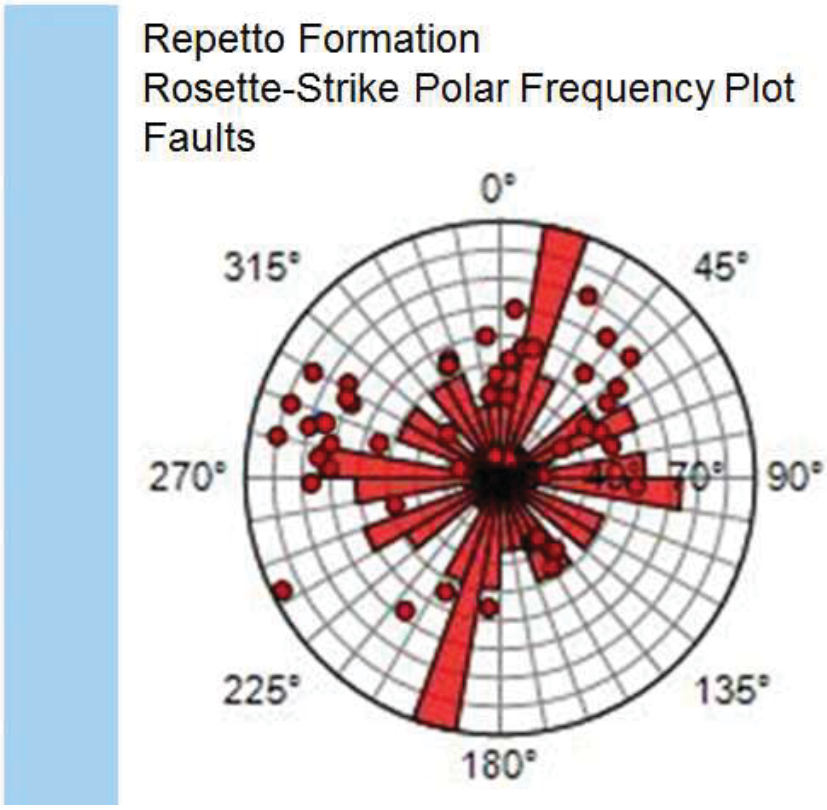

FIGURE 37. Lower hemisphere, equal-area stereonet of faults in the Repetto Formation with poles to planes and rose diagram strikes.

Pico Formation. This section describes the results observed for the individual fracture types found within the Pico Formation. Six groups of fracture types will be discussed, which include conductive fractures, resistive fractures, partial fractures, induced fractures, micro-faults, and faults. There is no borehole breakout present in the Pico Formation. Fracture orientations in this formation are less disperse by comparison to the Puente and Repetto formations.

Figure 38 is a Schmidt stereonet plot of all the conductive fracture interpreted in the Pico Formation. It shows three sets of conductive strike orientations occur in the Pico Formation. The dominant sets are seen between 310° to 320° (N40°-50°W) and 270° and 280° (N80°-90°W), but there is a third smaller set at 0° to 10° (N0°-10°E).

The resistive fractures found in the Pico Formation are plotted on Figure 39. In the Pico Formation, resistive fractures fall within two strike ranges. The ranges are from 350° to 320° (N10°-40°W) and from 310° to 290° (N50°-70°W) azimuth.

Similarly, partial fractures show two dominant sets of fractures in the Pico Formation, but minor rosette-strikes frequencies are also present (Figure 40). The dominant set ranges are located between 10° to 20° (N10°-20°W) and between 30° to 40° (N30°-40°W) azimuth.

There are no borehole breakout fractures present within the Pico Formation. However, drilling induced fractures show one preferential set of rosette-strikes frequencies towards the N-NW (Figure 41). This dominant set of fractures are striking between 340° to 10° (N20°W-N10°E).

Figures 42 and 43 are Schmidt stereonets of the micro-faults and faults in the Pico Formation. Micro-faults consist of two dominant sets that encompass most of the

fractures found in the Pico formation. These sets are between 260° to 280° (S80°W-N80°W) and between 290° to 310° (N50°-70°W). The faults interpreted in the Pico Formation fall within one dominant set of rosette-strikes frequencies. This set has a strike orientation range between 310° and 330° (N30°-50°W).

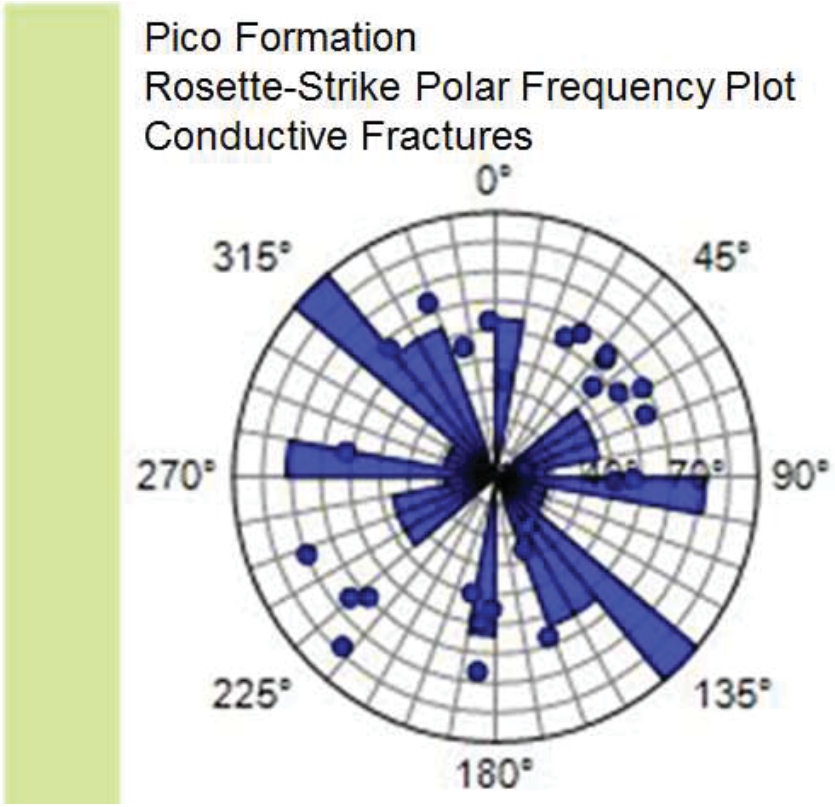

FIGURE 38. Lower hemisphere, equal-area stereonet of conductive fractures in the Pico Formation with poles to planes and rose diagram strikes.

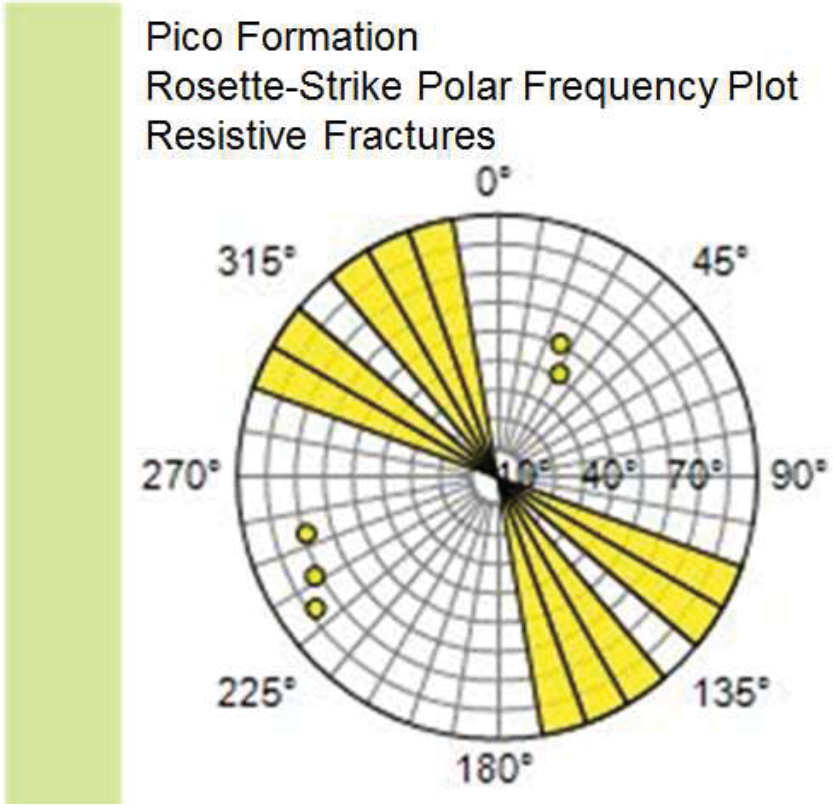

FIGURE 39. Lower hemisphere, equal-area stereonet of resistive fractures in the Pico Formation with poles to planes and rose diagram strikes.

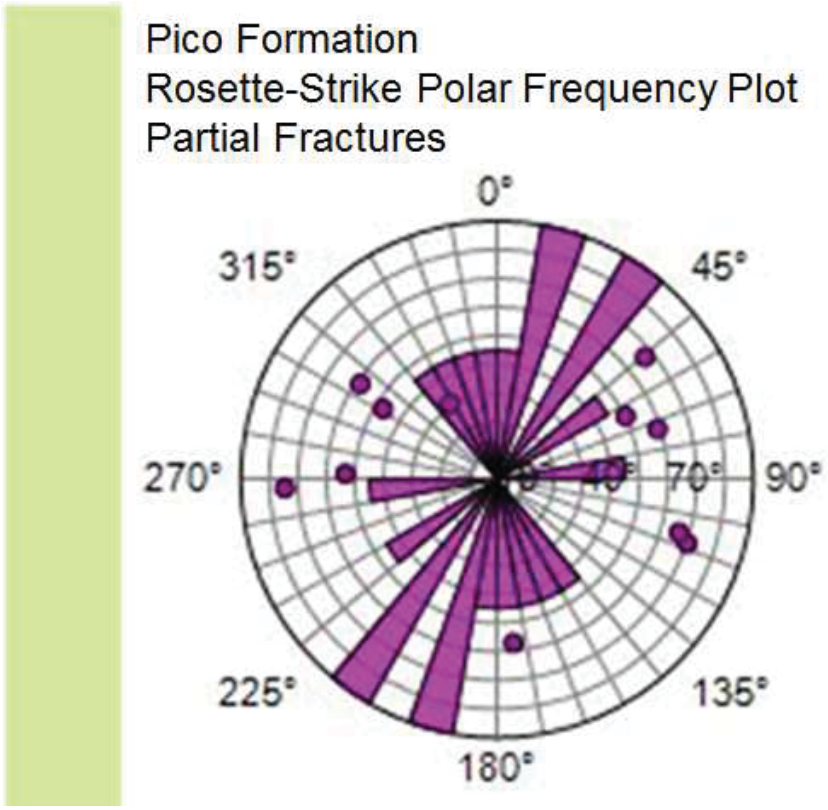

FIGURE 40. Lower hemisphere, equal-area stereonet of partial fractures in the Pico Formation with poles to planes and rose diagram strikes.

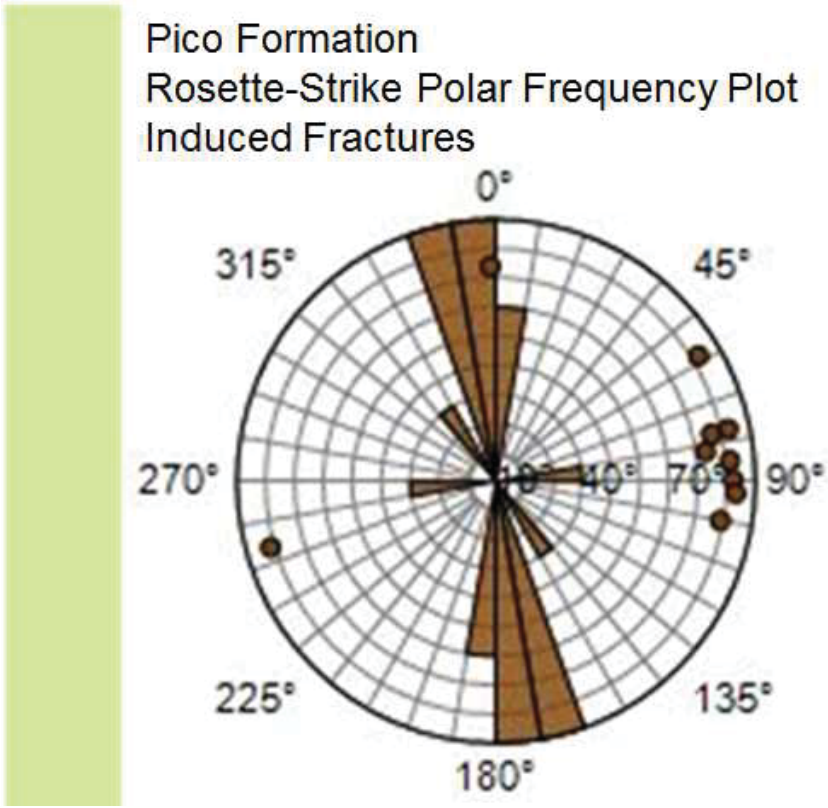

FIGURE 41. Lower hemisphere, equal-area stereonet of induced fractures in the Pico Formation with poles to planes and rose diagram strikes.

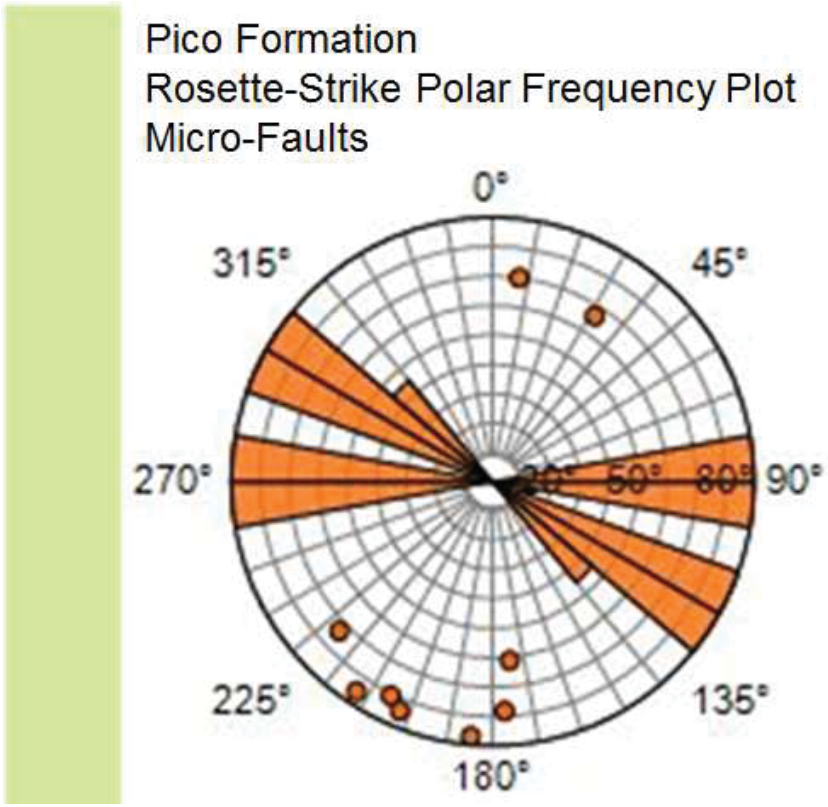

FIGURE 42. Lower hemisphere, equal-area stereonet of micro-faults in the Pico Formation with poles to planes and rose diagram strikes.

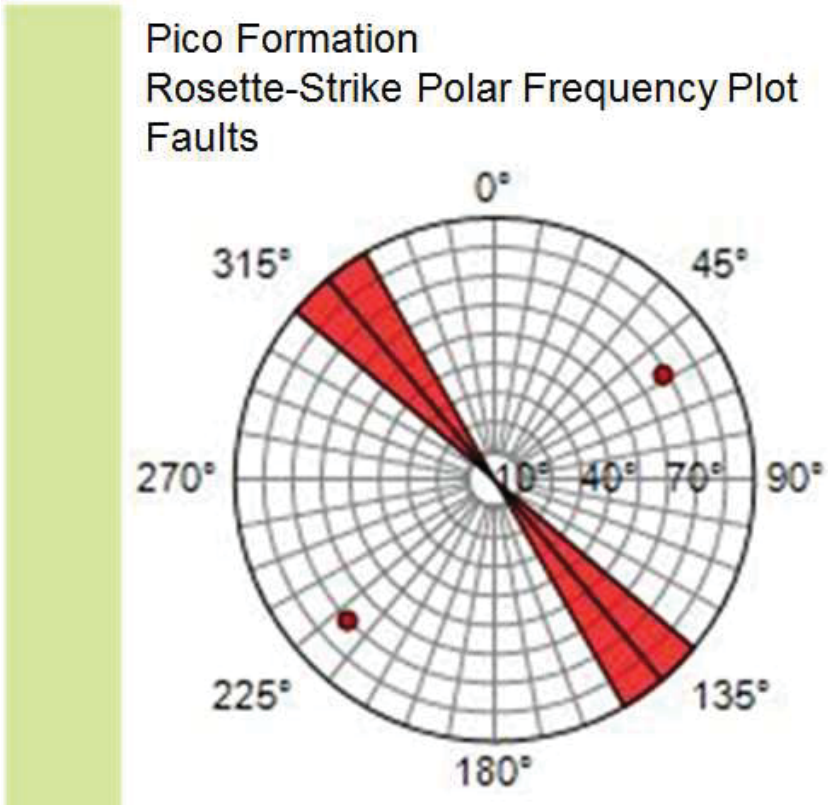

FIGURE 43. Lower hemisphere, equal-area stereonet of faults in the Pico Formation with poles to planes and rose diagram strikes.

San Pedro Formation. This section describes the results observed for the individual fracture types found within the San Pedro Formation, which is the youngest formation in this study. All seven fracture types are present in this formation and their results will be described in the following order: conductive fractures, resistive fractures, partial fractures, borehole breakout, induced fractures, micro-faults, and faults.

Figure 44 is a Schmidt stereonet plot of all the conductive fracture interpreted in the San Pedro Formation. It displays three significant sets of fracture strike orientations. These sets range between 0° to 20° (N0°-20°E), 350° to 330° (N10°-30°W), and 300° to 310° (N50°-60°W). The first two dominant sets occur more frequently than the latter.

On the other hand, resistive fractures found in the San Pedro Formation show a preference of fracture strike orientations towards the NE-SW (Figure 45). The dominant set of fractures has strikes that range between 60° and 70° (N60°-70°E). There are minor frequencies sets that are found between 10° and 120° (N10°E-S60°E).

Figure 46 is a Schmidt stereonet plot of all the partial fracture in the San Pedro Formation, which shows a broad range of partial fracture orientations. However, there is one dominant set that stand out above the rest and it ranges from 50° to 60° (N50°-60°E).

Figures 47 and 48 are Schmidt stereonet plots of borehole breakout and induced fractures interpreted in the San Pedro Formation. Borehole breakout orientations in the San Pedro Formation are mainly striking W-E. The highest frequencies are found between 260° and 280° (S80° W-N80° W). Conversely, induced fractures interpreted in the San Pedro Formation are oriented N-NW and fall within two strike ranges, 0° to 20° (N10°-20°E) and 30° to 40° (N30°-40°E).

Figures 49 and 50 are Schmidt stereonets of micro-faults and faults interpreted in the San Pedro Formation. Micro-faults in the San Pedro Formation have one dominant set of strike orientations between 60° to 70° (N60°-70°E). Faults on the other hand, display two dominant strike orientations between 0° to 10° (N0°-10°E) and 300° to 310° (N50°-60°W).

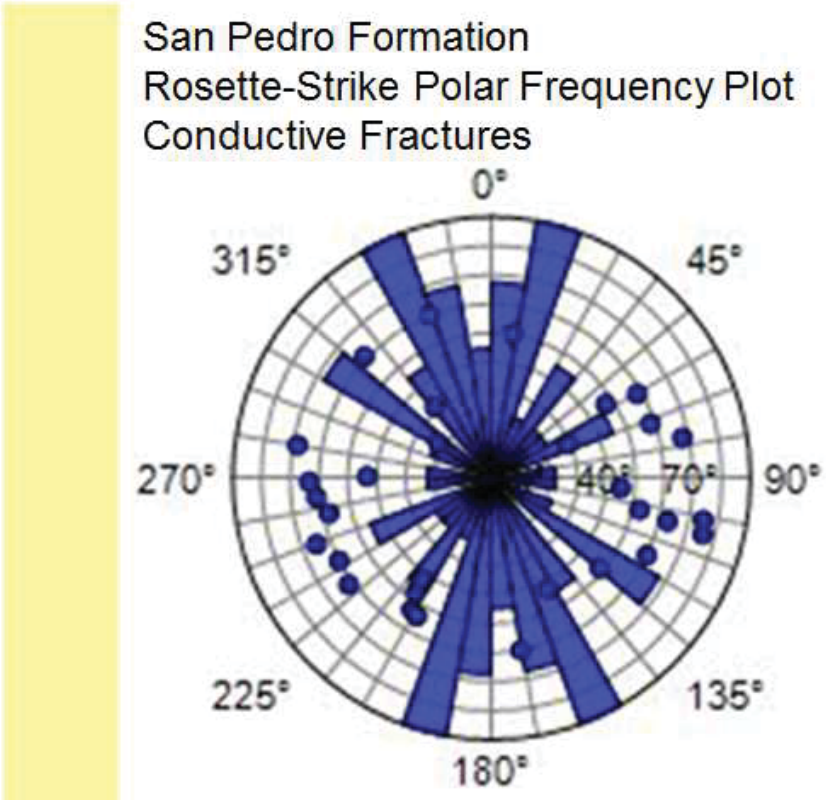

FIGURE 44. Lower hemisphere, equal-area stereonet of conductive fractures in the San Pedro Formation with poles to planes and rose diagram strikes.

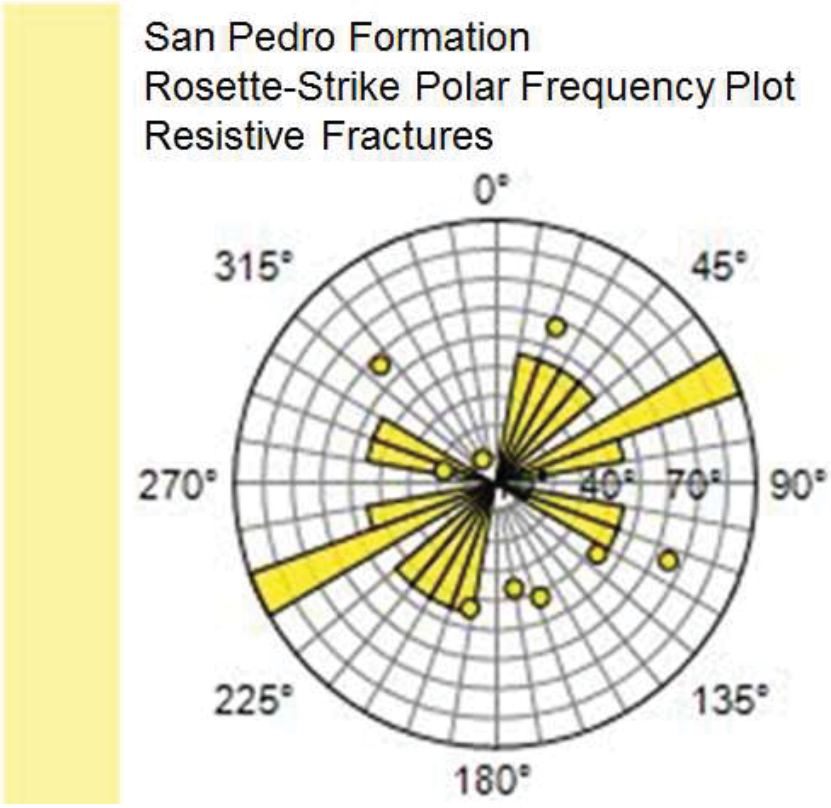

FIGURE 45. Lower hemisphere, equal-area stereonet of resistive fractures in the San Pedro Formation with poles to planes and rose diagram strikes.

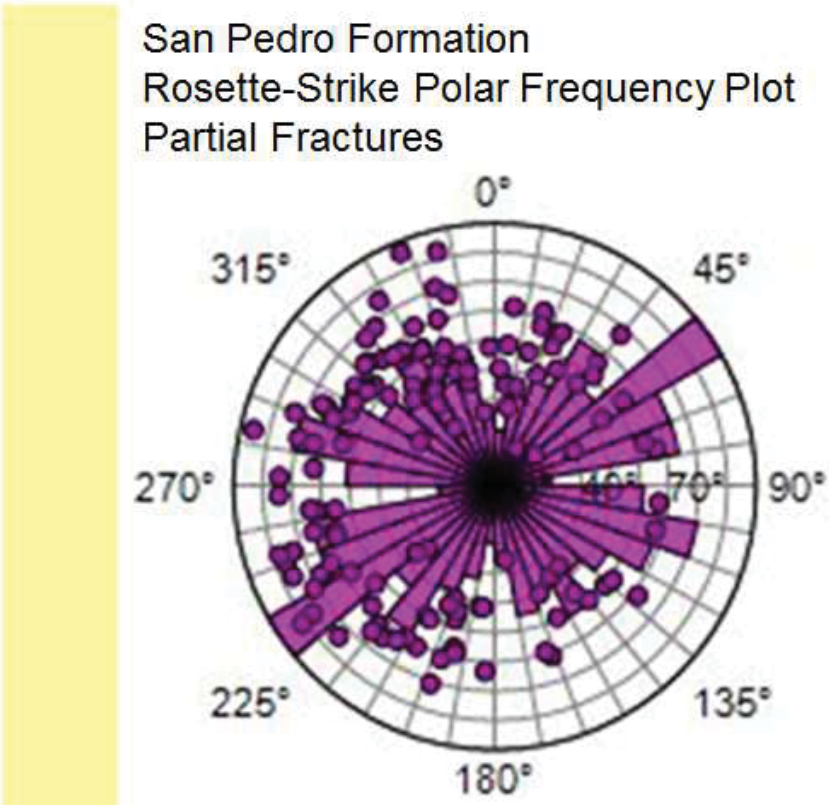

FIGURE 46. Lower hemisphere, equal-area stereonet of partial fractures in the San Pedro Formation with poles to planes and rose diagram strikes.

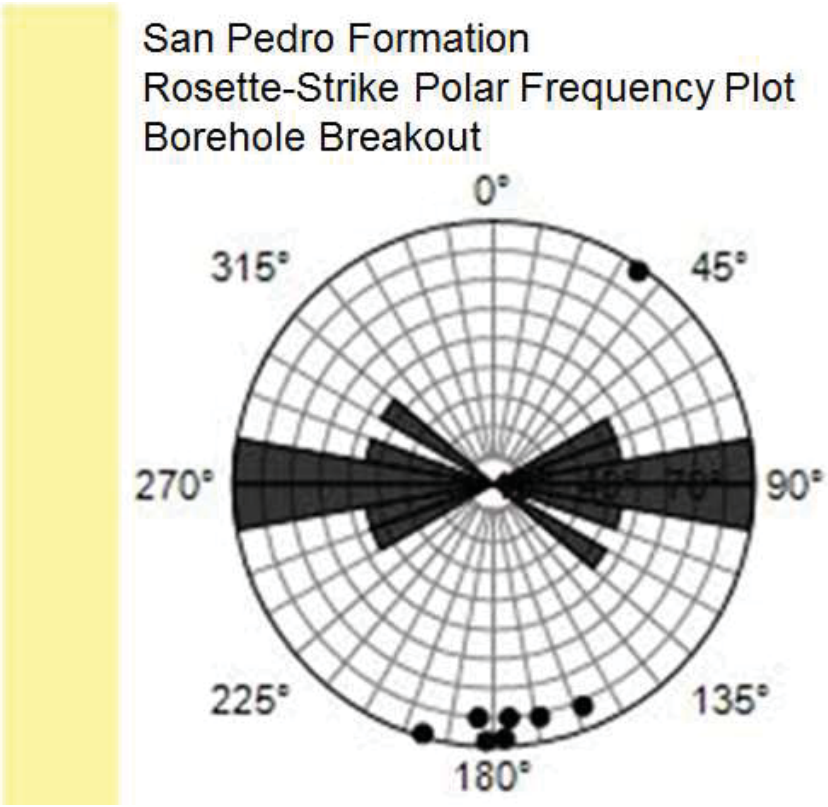

FIGURE 47. Lower hemisphere, equal-area stereonet of borehole breakouts in the San Pedro Formation with poles to planes and rose diagram strikes.

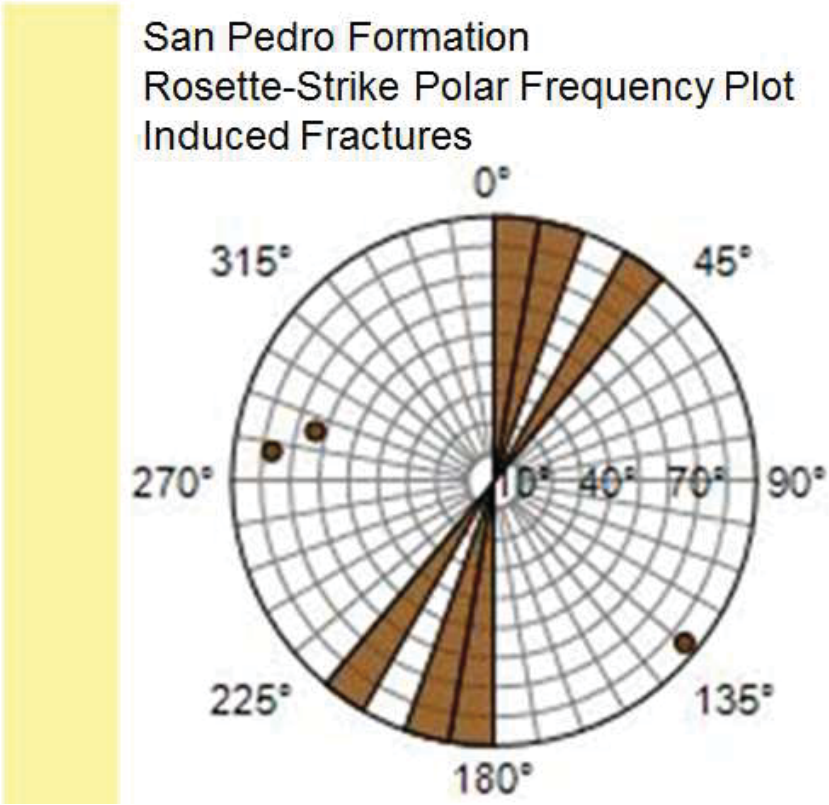

FIGURE 48. Lower hemisphere, equal-area stereonet of induced fractures in the San Pedro Formation with poles to planes and rose diagram strikes.

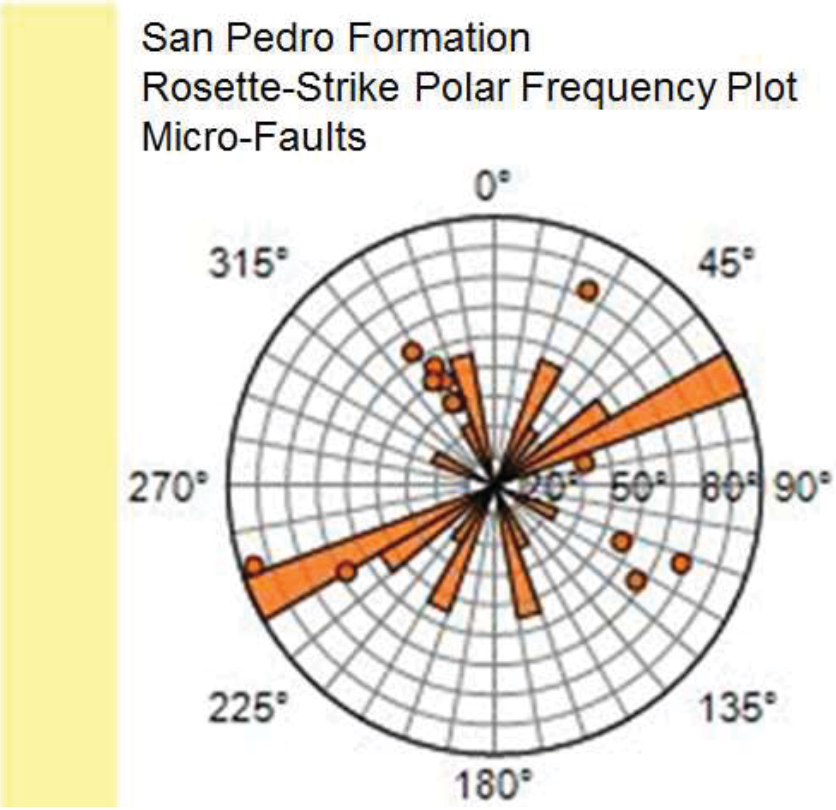

FIGURE 49. Lower hemisphere, equal-area stereonet of micro-faults in the San Pedro Formation with poles to planes and rose diagram strikes.

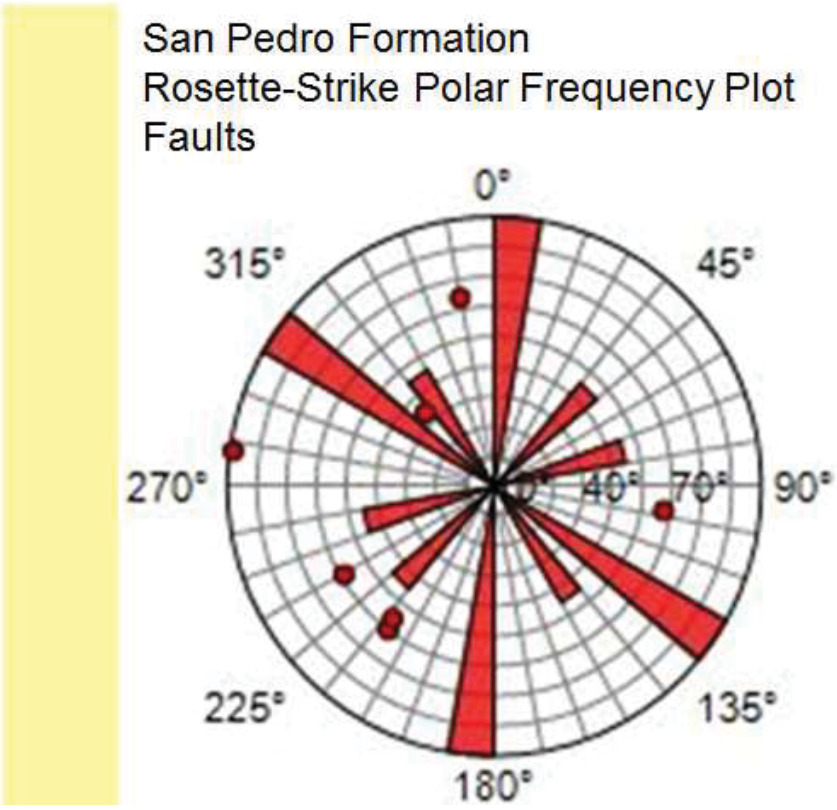

FIGURE 50. Lower hemisphere, equal-area stereonet of faults in the San Pedro Formation with poles to planes and rose diagram strikes.

CHAPTER 5

DISCUSSION

The data results are discussed in 4 sections. First, in-situ stress is discussed by identifying S_{Hmax} and S_{Hmin} established from borehole breakout and drilling induced fractures. This is done for the entire data set and at the formation level. Second, the stress orientations interpreted from the strikes of natural fractures is discussed by fracture type for each formation and as a whole. Third, similarities and differences between the in-situ stress and the stress interpreted from the strike of natural fracture will be discussed. Lastly, the relationship between the tectonic evolution and the stress inferences from this study will be compared.

Present-Day Stress Regime

Drilling Induced Fractures

Borehole breakouts and induced fracture sets were used to establish two dominant in-situ S_{Hmax} and S_{Hmin} orientations. Borehole breakouts form by compressional failure at azimuths where the concentrated stress is compressive, while drilling induced fractures form where it is tensile (Barton et al., 2009). The most commonly occurring S_{Hmax} orientations found in the Long Beach oil field are N and NW, while the most commonly occurring S_{Hmin} orientations are W-E and NE. How these stress orientations were derived will be discussed in this section.

Borehole breakouts are stress-induced cross-sectional shape elongations of the wellbore. They are defined as enlargements that develop in vertical wells at the orientation of the far-field minimum principal stress caused by compressive shear failure of the borehole wall (Barton et al., 2009). As a borehole is drilled, the material removed from the subsurface is no longer supporting the surrounding matrix, which causes circumferential stresses in the wellbore wall (Rajabi et al., 2010; Bell and Gough, 1979). Borehole breakouts occur when these circumferential stress exceed that required to cause compressive failure of the matrix and material "spall-off" from the borehole wall (Bell and Gough, 1979). In general, borehole breakouts form in very consistent orientations defined by the far-field minimum principal stresses over sections of the borehole. Therefore, when borehole breakouts are detected, their orientations can be used to interpret the orientations of these stresses (Barton et al., 2009). On electric image logs they appear as blurry zones 180° apart where the tool pad contact with the formations is weakened by the roughness of the breakout.

The most common borehole breakouts found in the data occurs between 270° to 280° azimuth. Thus, using the principals discussed above the corresponding S_{Hmin} is also oriented E to W while the S_{Hmax} is oriented N, between 350° to 10° azimuth. A set of less frequent, but notable, borehole breakouts also occur between 60° to 70° azimuth. This smaller set corresponds with a S_{Hmax} orientation between 330° to 340° azimuth. Although, this S_{Hmax} is obtained using a minor set of borehole breakouts, it is supported by the S_{Hmax} orientation derived from a dominant set of induced fractures.

Induced fractures occur in the borehole wall where the circumferential stress is negative (extensional) and exceeds the tensile strength of the rock (Barton et al., 2009).

These fractures are fine-scale features and only occur in the wall of the borehole. Generally, they do not propagate large distances into the formation unless the drilling-mud weight exceeds the magnitude of the least principal stress (Barton et al., 2009). In vertical wells these fractures form parallel to the far-field azimuth of $S_{Hmax\ on}$ the borehole axis (Zoback, 2007). In general, induced fractures also form in very consistent orientations defined by these far-field stresses along opposite sides of the borehole wall. In electric borehole images induced fractures appear 180° apart.

The data results show two dominant conjugate sets of drilling induced fractures between an azimuth of 320° to 330° and 0° to 10°. As a result, the two orientations of S_{Hmax} are N-NW, between 320°-330°, and N-NE, between 0°-10° azimuth. This argues in favor of at least two S_{Hmax} orientations existing in the Long Beach oil field. This is also viable when considering the S_{Hmax} interpreted from both the major and minor sets of borehole breakouts.

There is some variation that occurs between the two drilling induced fracture types. For example, the gradual transition of S_{Hmax} from 330° NW to 10° NE observed with relative minor induced fracture sets and the broader distribution of minor borehole breakouts. These variations are likely representative of localized stresses or data anomalies and will be further discussed in subsequent sections.

Petal fractures are drilling-induced fractures that show one distinctive set of orientations. These fractures are primarily striking north between 270° and 330° (N90°-50°W) azimuth. However, the most dominant range is between 280° and 300° (N60°-80°W). The orientation of these fractures can provide rough orientation of maximum principal stress (Zoback, 2009). However, petal fractures have a low data quality ranking

as explained in the methodology section. For this reason, the S_{Hmax} data obtained from these fractures are not reliable and will not be discussed further.

Formations and Principal-Stress Orientations

Puente Formation. This section discusses the in-situ stress in each formation, from oldest to youngest, using borehole breakouts and/or drilling-induced fracture sets. There was no borehole breakouts found in the Puente Formation. This may be a result of increased lithification in the Puente Formation, which would minimize spalling. However, there are seven induced fractures that plot within four distinct strikes-frequencies. These frequency sets represent the following S_{Hmax} orientations, in descending order from dominant to minor frequencies sets: 320° to 230° (N30°-40°W), 290° to 300° (N60°-70°W), 0° to 10° (N0°-10°E), and 270° to 260° (N80°-90°W). The dominant S_{Hmax} orientation found in the Puente Formation is NW, between 320° to 230° (N30°-40°W), while the dominant S_{Hmin} is NE, between 50° to 60° (N50°-60°E).

Repetto Formation. Borehole breakout fractures in the Repetto Formation show one dominant and one minor set of strike frequencies. The dominant set represents an S_{Hmax} orientation of 350° to 10° (N80°W-N10°E) azimuth, with an S_{Hmin} between 260° to 280° (S80°W - N80°W). The minor set has a S_{Hmin} that occurs between 330° to 340° azimuth and has a S_{Hmin} of 60°-70° (N60°E – N70°E).

Induced fractures show two dominant S_{Hmax} orientation ranges, which include 320° to 340° (N20°-40°W) and 0° to 10° (N0°-10°E). Their respective S_{Hmin} are between 50° to 70° and 90° to 100°. There is also one minor set that represents a S_{Hmax} orientation range of 350°-360° (N80°-90°W) and a S_{Hmin} of 80°-90°.

The S_{Hmax} derived from both borehole breakouts and drilling-induced fractures overlap relatively well and argue for two S_{Hmax} orientations of N and NW. These orientations are found between 350° to 10° (N80°W-N10°E) and between 320° to 330° (N40°-50°W). The small variation between the two fracture types may represent a minor variation in localized stress or a variation in drilling technique or fluid. For the purpose of this study, the S_{Hmax} orientation was used where the two fracture types overlap.

Borehole breakouts and induced fractures in the Repetto Formation make up the largest sample size of drilling-induced fracture sets in all the data. Borehole breakouts encompasses 86% of the total borehole breakout data while induced fractures make up 38% of the total induced fracture data set. Thus, the drilling-induced fractures from the Repetto Formation, particularly borehole breakouts, may be skewing S_{Hmax} and S_{Hmin} orientations when evaluating the entire data sets as a whole. However, any possible over representation from the Repetto Formation is mitigated as a result of evaluating drilling induced fracture sets at the formation level.

Pico Formation. There are no borehole breakout fractures present within the Pico Formation. This too may be due to lithological control since the Pico Formation contains a greater amount of clay and shale when compared to the other geologic units of this study. However, drilling induced fractures were found in this formation. These fractures show one preferential set of strikes frequency orientations to the N-NW. The S_{Hmax} range of this set is found between 340° to 10° (N20°W-N10°E), which corresponds to a S_{Hmin} of 70° to 100° (N70°E-S80°E).

San Pedro Formation. Borehole breakout strike-frequencies are oriented primarily W to E. The highest frequencies are found between 260° and 280° (S80° W –

N80° W), which is the S_{Hmin}. The S_{Hmax} is orientated between 350° and 10° (N10° W – N10° E). Conversely, drilling-induced fractures are oriented N-NE and have two dominant strike ranges between 0° to 20° (N10°-20°E) and 30° to 40° (N30°-40°E). These strike ranges are also the S_{Hmax} orientations for these induced fractures. Moreover, S_{Hmin} is found between 270° to 290° (N90°-80°W) and between 310° to 320° (N60°-50°W).

The S_{Hmax} derived from both borehole breakouts and drilling induced fractures generally overlap with some variation to the NE from induced fractures. The S_{Hmax} orientations for this formation will only include the sections that overlap, which represent a N to N-NE orientation.

In the San Pedro Formation, the S_{Hmax} and S_{Hmin} orientations generally overlap, but there is some variation to the NE. The S_{Hmax} orientation of borehole breakouts is relatively close to the largest set of induced fractures, with only a ten degree difference from the dominant north orientation towards the east. However, there is a dominant NE S_{Hmax} set seen in induced fractures that is not represented in borehole breakouts. Thus S_{Hmax} in the San Pedro Formation is interpreted as N to N-NE, between 350° and 10° (N10° W – N10° E).

Summary of In-Situ S_{Hmax} in Formations

While borehole breakouts show a dominant northern S_{Hmax} in the two formations with data, induced fractures appear to show some variation to the NW and NE. In the Puente Formation, the NW S_{Hmax} is supported by dominant and minor induced fracture sets. In the Repetto Formation, the overlap of dominant and less frequent sets of borehole breakouts and induced fractures argue for two possible S_{Hmax} orientations of

NW and N. In the Pico Formation, induced fractures show S_{Hmax} orientated to the N-NW. Lastly in the San Pedro Formation, borehole breakouts and induced fractures argue for a N to N-NE S_{Hmax} orientation.

Stress Orientation of Natural Fractures and Faults

Anderson's Theory and Principal-Stress

Anderson's theory of faulting (Anderson, 1942) and Coulomb's law of failure provide the background knowledge to intrepret and predict the stress conditions under which faults and fractures form, and can be used to explain how fractures and faults are oirented systematically with respect to stress directions. For example, Anderson's theory explains that Mode I tension fractures form parallel to the direction of greatest principal stress (σ_1) and perpendicular to the direction of least principal stress (σ_3) (Davis and Reynolds, 1996). The natural fractures identified in this study are interpreted to be Mode I fractures as defined by Broek (1992), which are also identified as joints in geological nomenclature (Engelder, 1987; Pollard and Aydi, 1988; Lacazette, 2009). Thus, the strike orientation of the natural fractures in this study can therefore directly indicate the orientation of the maximum and minimum stress at the time those natural fractures formed.

Faults, on the other hand, form in undamaged rock as conjugate sets oriented parallel to the intermediate stress axis and are generally 22° to 30° from the maximum stress axis (Lacazette, 2009). In deformation experiments when conjugate faults form, the conjugate angle between the faults is bisected by the direction of greatest princlipal stress (σ_1) (Davis and Reynolds, 1996). This systematic relationship that exist among faults, fractures, and princpal stress provides the basis for interpreting paleostress

direction in rocks deformed. In this section principal stress obtained from natural fractures is discussed for each fracture type and for each formation.

Natural Fractures and Faults

There are 488 conductive fractures in this study, which make up 32% of the total data and 43% of the natural fractures in this study. This is the greatest group of natural fractures and as a whole have a great diversity of fracture orientations. The set with the greatest group of conductive fractures show a N and NE S_{Hmax}, with orientations between 10° to 20° (N10°-20°E) and 50° to 60° (N50°-60°E). However, it should be noted that these two fracture sets are not significantly larger than the rest (figure 13).

On the other hand, resistive fractures show a clear and dominant NW S_{Hmax} orientation between 270° and 320° (N50°-90°W). However, smaller less dominant sets of resistive fractures are also seen within 10° of the dominant set and as well between 340° to 350° (N20°W). This broadens the range of the dominant S_{Hmax} and shows a potential alternative S_{Hmax} orientation to the N-NW.

Partial fractures also have a relatively great diversity of fracture orientations, but show two dominant sets that have NW orientations. The S_{Hmax} orientation for these two sets are located between 280° to 300° (N60°-80°W) and between 320° to 330° (N30°-40°W). However, it should be noted that these fractures are less unreliable and have a low-quality ranking as explained in the methodology section.

The most dominant micro-fault sets have strikes frequencies between 310°-320° (N40°-50°W) and 60° to 70° (N60°-70°E). As a result, this indicates that S_{Hmax} was within the range of 210° to 340° (S30°W-N20°W) of the time of their formation. Furthermore, these two sets appear to be conjugate fault sets 60° apart, which may imply

the dominant maximum principal stress at the time of formation was west 270° to 280° azimuth.

Faults have three dominant orientation sets, in which two are relatively similar to the dominant sets observed with micro-faults. The strike orientations of these sets are between 260° to 270° (N0°-20°W), 300° to 310° (N50°-60°W), and 10° to 20° (N10°-20°E). Thus, the S_{Hmax} orientation at the time of their formation was within 230° (S50°W) to 340° (N20°W) for the western striking sets and within 340° (N20°W) to 50° (N50°E) for the northerly striking set.

Formations and Principal-Stress Orientations

This section discusses the stresses interpreted in each formation, from oldest to youngest, using natural fractures sets.

Puente Formation. This section describes the stress orientations interpreted form natural fractures found within the Puente Formation. Five types of fractures will be discussed, which include conductive fractures, resistive fractures, partial fractures, micro-faults, and faults.

Overall the distribution of S_{Hmax} represented by conductive fractures is generally broad and shows strike variations of S_{Hmax}. The largest set has a S_{Hmax} orientation west between 270° to 280° (N80°-90°W). The following sets of descending frequencies have S_{Hmax} orientations between 320° to 330°(N30°-40°W), 50° to 60° (N50°-60°E), 290° to 310° (N30°-40°W), and 20° to 30° (N20°-30°E). However, when observing large and minor sets combined, there is a closely spaced distribution of strike frequencies that range from 270° to 360° (N90°-0°W). This may represent a broad range of S_{Hmax} orientations to the NW as well.

On the other hand, resistive fractures in the Puente Formation show one clear dominant S_{Hmax} orientation to the W-NW, between 290°-300° (N60°-70°W). There are minor sets within 20° to the west and 10° to the north of the dominant S_{Hmax} as well as between 340°-10° (N0°2W- N10°E), but they contain significantly less resistive fractures than the dominant set.

Partial fractures show three dominant S_{Hmax} directions to the W, N-NW, and N, as well as a broad W-NW orientation of closely spaced minor sets as well. The largest set of partial fractures shows a S_{Hmax} range between 280°-290° (N80°-90°W). Two other large sets have S_{Hmax} ranges between 340°-350° (N10°-20°W) and 0°-10° (N0°-10°E).

There are three dominant micro-fault sets with strikes-frequencies between 290° to 300° (N60°-70°W), 310° to 320° (N40°-50°W), and 60° to 70° (N60°-70°E). Micro-faults are generally striking NW or SW in the Puente Formation with no micro-faults striking directly north. As a result, this indicates that S_{Hmax} was likely orientated within 210° to 350° (S30°W - N10°W) at the time they were formed.

Similarly, faults interpreted in the Puente Formation are relatively split into NE or SW strikes with few data found in the north or south. However, there are four sets that stand out from the rest between 220°-230° (S40°-50°W), 250°-270° (S70°-90°W), 280°-290° (N80°-70°W), and 310°-320° (N40°-50°W). These strikes indicate that S_{Hmax} was likely within 190° to 350° (S10°W - N10°W) when these sets of faults formed.

Repetto Formation. This section describes the stress orientations interpreted form natural fractures found within the Repetto Formation. All five fractures types will be discussed in the following order: conductive fractures, resistive fractures, partial fractures, micro-faults, and faults.

The overall distribution of S_{Hmax} represented by conductive fractures in the Repetto Formation is similar to that observed in the Puente Formation due to a great number of strike variations. There are two greater sets that represent S_{Hmax} orientations to the N-NW and to the NW. These S_{Hmax} orientations range between 10°-20° (N10°-20°E) and between 50°-60° (N50°-60°E).

Conversely, resistive fractures in the Repetto Formation primarily show S_{Hmax} orientations as W-NW, between 260° and 330 ° (S80 ° W – N30 ° W). Moreover, the most dominant range of S_{Hmax} is observed between 280° and 300° (N60°-80°W). Partial fractures appear to have broad S_{Hmax} orientations similarly to conductive fractures. The greatest set of partial fractures has a NW dominant S_{Hmax} orientation between 320° to 330° (N30°-40°W).

There are three sets of relatively higher strike frequencies in the Repetto Formation. These sets range, in ascending order, between 300°-310° (N40°-50°W), 340°-360° (N0°-30°W), and 20°-30° (N20°-30°E). As a result, dominant S_{Hmax} orientations are more likely to fall between 270° (N90°W) and 30° (N30°E) azimuth (W to NE). Faults on the other hand, show a very dominant N-NE S_{Hmax} orientation in this formation between 10° to 20° (N10°–20°E).

Pico Formation. This section describes the stress orientations interpreted form natural fractures found within the Pico Formation. Five types of fractures will be discussed, which include conductive fractures, resistive fractures, partial fractures, micro-faults, and faults.

There are two dominant S_{Hmax} orientations interpreted from conductive fracture found in the Pico Formation. These orientations are found between 310° to 320° (N40°-

50°W) and NW between 270° and 280° (N80°-90°W). Resistive fractures in this formation have S_{Hmax} orientations to the N-NW and NW, between 350° to 320° (N10°-40°W) and between 310° to 290° (N50°-70°W). Conversely, the dominant S_{Hmax} orientations of partial fractures are NE, between 10° to 20° (N10°-20°W) and between 30° to 40° (N30°-40°W). Although, there are a few minor sets with NW S_{Hmax} orientations as well.

Micro-faults consist of two dominant strike frequencies sets to the west between 260° to 280° (S80°W-N80°W) and between 290° to 310° (N50°-70°W). These set could correspond to faults expected to form from a NW to SW S_{Hmax} orientation range between 340° (N20°W) and 230° (S50°E). On the other hand, the only set of faults found in the Pico Formation are striking between 310° and 330° (N30°-50°W), which would indicate the S_{Hmax} orientation between 0° and 280° (N80°W).

San Pedro Formation. This section describes the stress orientations interpreted form natural fractures found within the San Pedro Formation, which is the youngest formation in this study. All five types of natural fractures will be discussed in the follow order: conductive fractures, resistive fractures, partial fractures, micro-faults, and faults.

The primary S_{Hmax} orientation ranges interpreted from conductive fractures in the San Pedro Formation are 0° to 20° (N0°-20°E), 350° to 330° (N10°-30°W), and 300° to 310° (N50°-60°W), although, the latter set is smaller than the first (NW and NE). On the other hand, resistive fractures have a dominant S_{Hmax} orientation to the east, with the dominant set between 60° and 70° (N60°-70°E). Partial fractures show a broader range of sets, but the highest frequency set is found between 50° to 60° (N50°-60°E).

Micro-faults in the San Pedro Formation have one dominant set of strike orientations between 60° to 70° (N60°-70°E), which may represent a S_{Hmax} orientation between 30° to 100° (N30°-100°E). Faults on the other hand, display two dominant strike orientations between 0° to 10° (N0°-10°E) and 300° to 310° (N50°-60°W). The S_{Hmax} orientation range for these two sets overlaps and is found between 270° (N90°W) and 40° (N40°E).

Summary of In-Situ S_{Hmax} in Formations

While conductive fractures overall display a broader range of possible S_{Hmax} orientations, the orientations of the dominant sets found in each formation are distinctly different. In the Puente Formation, the dominant S_{Hmax} is oriented W, but in the Repetto Formation the dominant sets are oriented N-NE and NE. In the Pico Formation, the dominant S_{Hmax} orientations changes to the NW and W, while in the San Pedro Formation there are conjugate sets of S_{Hmax} orientations that are N-NW or N-NE.

In contrast, resistive fractures have closely grouped sets of fractures that narrowly define S_{Hmax} in each formation and demonstrate a NW to NE transition in all four formations from the oldest to the youngest. In the Puente Formation, the NW oriented S_{Hmax} is supported by a dominant and narrowly defined fracture set. In the Repetto Formation, dominant and minor sets of fractures define a slightly broader NW S_{Hmax} orientation. In the Pico Formation, dominant conjugate sets of resistive fractures show a NW and N-NW S_{Hmax} orientation. Lastly in the San Pedro Formation, dominant and minor sets establish a NE S_{Hmax} orientation.

S_{Hmax} orientations interpreted from partial fractures appear less consistent throughout the four formations. In the Puente Formation, dominant sets show W, N-NW,

and N-NE S_{Hmax} orientations. In the Repetto Formation, the dominant S_{Hmax} is oriented NW, while in the Pico Formation the dominant S_{Hmax} is N-NE. In the San Pedro Formation, the dominant set supports a NE S_{Hmax} orientation. Partial fractures have a poor data quality ranking as explained in the methodology section. For this reason, the S_{Hmax} data obtained from partial fractures are not reliable and will not be discussed further.

The S_{Hmax} orientations interpreted from the strike of faults present larger ranges of possibilities since faults can generally rupture 30° from the maximum stress axis. However, there is variation between the stress orientations interpreted from micro-faults and larger faults within formations and across the entire section, although the two can sometimes overlap or fall within close proximity. This is primarily a result of the wide range of stress field orientations that could have been present when they formed.

The greatest similarities between micro and faults were observed in the Puente Formation. Here the dominant S_{Hmax} orientation appears to have prevailed from NW to SW at the time most of these faults were formed. In the Repetto Formation, there is a large range of fault strikes seen in both micro-faults and faults that indicate these sets ruptured under a variety of different stresses. However, the dominant sets differ between micro-faults and faults, with micro-faults likely occurring when S_{Hmax} was oriented between W to NE and faults when it was N-NW to NE. In the Pico Formation, the S_{Hmax} ordination range was interpreted from SW to NW for micro-faults, but since these sets appear to be conjugate faults the S_{Hmax} axis may have been oriented 285°. Faults in the Pico Formation ruptured when S_{Hmax} was oriented W to N. In the Pico Formation, the dominant sets of micro and faults may have formed with little overlap of stress regimes,

with micro-fault more likely to occur when S_{Hmax} was oriented NE to SE and faults when it was between W to NE. However, dominant faults sets appear to be conjugate sets with S_{Hmax} likely oriented NW at 235° azimuth.

Stress Variation

In-situ vs. Paleo-Stress

Several differences exist between the present day stress orientation derived from drilling induced fractures and the stress orientations interpreted from natural fractures and faults. These differences are observed when comparing the S_{Hmax} derived from both conductive and resistive fractures, as well as faults to the present day stress. Large differences observed between conductive and resistive fractures also provide a proxy for assessing variation of paleo-stress as well. This section will compare the differences and similarities of S_{Hmax} orientations interpreted from the various fracture types and formations.

Conductive fractures. The large range of S_{Hmax} interpreted from conductive fracture is likely a result of variable stress field changes throughout time as well as the location of the fractured rock relative to local geologic features. Even when only comparing the dominant fractures sets, differences between the S_{Hmax} derived from these sets and that of the in-situ S_{Hmax} are present throughout all four formations. The S_{Hmax} orientation from dominant conductive fracture sets can vary up to 40 degrees from the in-situ orientation. Moreover, whereas in-situ S_{Hmax} show an overall stronger northern orientation and a relative smaller migration from NW to N-NE throughout the four formations, S_{Hmax} interpreted from conductive fractures is diverse and varies significantly between the formations.

Another possible explanation for the large discrepancies of S_{Hmax} orientations interpreted from conductive fractures may be the productive history of the Long Beach oil field. New fracturing of the matrix rock or propagation of pre-existing fractures can be facilitated with changing pore pressure from hydrocarbon extraction and/or water injection that can affect or change the dynamic stress field of each reservoir (Teufel, 2012). This may be acutely pertinent to the Repetto Formation, which has seen the greatest amount of development and subsequent depletion since the field was discovered in 1921 (Wright, 1991). Not surprisingly it also has the largest amount of conductive fractures and orientation diversity compared to the three other formations. Nonetheless, discrepancies still exist even in formation with no or relatively minimal oil production history, such as the Pico or San Pedro formations.

In the Puente Formation, the difference between dominant conductive fracture sets and induced fractures are as large as 40 degrees to the west. Here the dominant S_{Hmax} interpreted from conductive fractures is W and SW, while in-situ S_{Hmax} is oriented NW. The difference may reflect localized stresses, but given the large sample size of these dominant sets it is more likely these fractures formed under a different stress regime than the present. However, there are minor and intermediate sets of conductive fractures with relatively similar strikes as the in-situ orientation. These fractures may be younger fractures that developed under current stress conditions.

In the Repetto Formation, the difference between dominant conductive fracture sets and the in-situ maximum principal stress can vary as much as 80 degrees. In this formation two possible in-situ S_{Hmax} orientations are interpreted as NW and N. Similarly, two sets of dominant conductive fractures are found in this formation, but they are

orientated N-NE and NE. This indicates that the S_{Hmax} orientation at the time these fractures formed was significantly different than that observed today from borehole breakouts and induced fractures. Like in the Puente Formation, smaller sets do exist with similar orientations to the in-situ S_{Hmax} orientation, however, they are also not idiosyncratic among the large sample of disperse strikes.

In the Pico Formation, the S_{Hmax} interpreted from conductive fractures is also different than the in-situ S_{Hmax} orientation, but only by 20 degrees from the most dominant set of fractures. Here the S_{Hmax} orientation interpreted from this set of conductive fractures is NW, while the in-situ S_{Hmax} orientations is N-NW. Although some variation exist it would not be unreasonable to presume that these fractures formed under relatively similar stress conditions to the present. However, there is a slightly smaller set of conductive fractures that are oriented west and appear to be the conjugate pair of the largest set previously discussed. If this set is indeed a conjugate then it is likely to have developed around the same time as the other, which would infer a secondary S_{Hmax} orientation to the west. In this case, it could be argued that this pair of fractures formed under different stress conditions than the present, however, differentiating the relative timing of these sets is not possible at this time.

In the San Pedro Formation, the difference between the S_{Hmax} interpreted from conductive fractures and that of the in-situ stress is not greatest. Here the possible S_{Hmax} interpreted from dominant conductive fracture sets is N-NW and N-NE, while the in-situ orientation is N to N-NE. The greatest divergence is 20 degrees to the west, which exist for the dominant conductive fracture set that is oriented N-NW. This formation contains the closest proximity observed between conductive fractures and drilling induced

fractures, and thus suggests that these fractures developed under somewhat similar principal stress orientations as today.

Resistive fractures. In contrast to conductive fractures, the S_{Hmax} interpreted from resistive fractures have narrow groups of fracture strike sets and show a more steady transition from formation to formation. Yet, differences between the S_{Hmax} derived from these sets and that of the in-situ S_{Hmax} exist throughout all four formations as well. The S_{Hmax} orientation interpreted from resistive fracture sets can vary up to 50 degrees from the in-situ S_{Hmax} orientation. Furthermore, whereas in-situ S_{Hmax} has an overall stronger northern component, S_{Hmax} interpreted from resistive fractures show a larger migration from NW to NE from the youngest to the oldest formation.

The discrepancy between the S_{Hmax} orientations interpreted from resistive fractures and that of in-situ stress are also likely a result of variable stress changes through time and the location of the fractures relative to other localized geologic features. However, resistive fractures are likely more reliable indicators of paleostress than other natural fracture types. This is predominantly based on the fact that once healed, mineralized fractures are more likely to survive deformation due to the added strength of the healed material. This is certainly not always the case as there are many variables that can affect which fractures are healed, and when or how they are healed such as pore pressure, mineral and fluid content, diagenesis, effective or preferential fluid flow, production history, and temperature. However, once a fracture is mineralized it is likely to endure longer without collapsing compared to open fractures. In this case, the lower number of healed fractures combined with the narrow range of orientations suggest these fractures did form during a different stress regime than the present.

In the Puente Formation, S_{Hmax} interpreted from dominant conductive fractures is 20 degrees west of the in-situ S_{Hmax} orientation. Here both interpretations of S_{Hmax} are relatively oriented NW. The 20 degree variation can indicate this dominant resistive fracture set formed under a different stress than the present. However, there is a smaller set of drilling-induced fractures that has the same orientation as these resistive fractures. This along with the close proximity to the dominant in-situ S_{Hmax} does undermine the argument in favor of a different stress regime. However, another possibility exist that these fractures were preferentially preserved due to their proximity to the present day S_{Hmax} orientation while others collapsed and/or were not mineralized.

Despite the differences, an important thing to note is that all dominant natural fracture sets, including faults, found in the Puente Formation have a west-dominant d orientation, whether it be NW, W, or SW. Remarkably, there are no dominant conductive fracture sets that match the orientation of the dominant resistive fracture set. This suggests that these fractures may have also developed under different stress conditions compared to each other.

In the Repetto Formation, resistive fractures appear to have developed when S_{Hmax} was 20 to 50 degrees west of the in-situ S_{Hmax} orientations. Here, there are two possible in-situ S_{Hmax} orientations of NW and N, while there is only one narrowly defined S_{Hmax} orientation of W-NW interpreted from resistive fractures. Unlike in other formations, there are also no minor sets of resistive fractures with similar orientations to the in-situ S_{Hmax} orientation. This suggests that the S_{Hmax} orientation at the time these resistive fractures formed was significantly different than that observed today and potentially record a pre-existing paleo-stress orientation. Additionally, there are no other dominant

natural fracture sets with the same orientations as these dominant resistive fractures. Yet, there does exist one minor conductive fracture set that matches and one micro-fault set that comes within 10 degrees, thus perhaps these sets formed around the same time and under the same paleo-stress conditions.

In the Pico Formation, the S_{Hmax} orientation interpreted from resistive fractures shows a variation up to 50 degrees to the west from the in-situ S_{Hmax} orientation. However in this formation, resistive fracture strikes contain the broadest range observed and, thus, their possible S_{Hmax} orientation can range between NW to N-NW. In this case, a 10 degree overlap amid these resistive fractures and induced fractures exists between 340° to 350° azimuth (N20°-10°W). While it is possible that the resistive fractures which do not overlap represent a pre-exist paleo-stress record, the 10 degrees that do overlap in the N-NW orientation cannot be differentiated. Nonetheless, similar NW orientations are also observed among dominant conductive fractures, micro-faults and large fault sets. These similarities may suggest that all these sets formed around the same time and under the same paleo-stress conditions, which is different than that observed today.

In the San Pedro Formation, the difference between the S_{Hmax} interpreted from resistive fractures and that of the in-situ stress is up to 50 degree to the east. Here the possible S_{Hmax} interpreted from the dominant resistive fracture set is E-NE, while the in-situ orientation is N to N-NE. This suggests that these fractures developed under different stress orientations than the in-situ stress observed today. Remarkably, there are no dominant conductive fracture sets that match the orientation of these dominant resistive fractures. It is likely these fractures developed during a paleo-stress orientation that is possibility even older than that interpreted from conductive fractures which are

more similar to that of the present day stress. The only other natural fractures that may have formed during similar S_{Hmax} conditions in this formation are micro-faults. Otherwise, resistive fractures appear to display a unique orientation in the Pico Formation.

Faults. Differences between the S_{Hmax} derived from faults and that of the in-situ S_{Hmax} exist as well. Yet, in contrast to the other natural fractures, the S_{Hmax} orientations interpreted from faults have great ranges of possibilities since faults can generally rupture up to 30 degrees from the maximum stress axis (David, 1996). Therefore, overlap among the S_{Hmax} derived from faults and that of the in-situ stress is also observed throughout most of the formations as well. In spite of this, variations still exist and can also be seen when comparing micro-faults, faults, and fractures.

Furthermore, whereas in-situ S_{Hmax} has an overall dominant northern orientation, the S_{Hmax} orientations interpreted from faults often have a significant W or NE element. Additionally, differences are also observed between the strikes of micro-faults and faults. Although several factors can contribute to these differences, it may also be a result of variable paleo-stress through time.

The most significant difference observed between dominant fault sets and the in-situ stress orientation is found in the Puente Formation, which can range up to 120 degrees. Yet, the greatest similarities between micro-faults and large faults are also seen in this formation. Here, the dominant S_{Hmax} orientation interpreted from the strikes of these faults lies between NW to SW. However, the in-situ S_{Hmax} orientation is only found in the NW direction. It is possible that the faults striking NW formed relatively recent under the present day stress regime. However, differentiating the timing of the individual

fault sets is difficult given such a large possible range. Additionally, it is also possible these faults may be conjugates fault sets. If this is the case, then the S_{Hmax} orientation can be interpreted as having been relatively oriented west at the time these conjugate sets formed.

When comparing the S_{Hmax} orientation interpreted from other fractures in the Puente Formation, both resistive and conductive fractures also present relative western S_{Hmax} orientations. Furthermore, conductive fractures present a similar dominant SW orientation further validating a possible SW/NE paleo-stress orientation. In either case, it is clear that the faults observed in the Puente Formation also confirm an alternative stress orientation than the in-situ stress interpreted from drilling induced fractures.

In the Repetto Formation, the S_{Hmax} interpreted from faults and that of the in-situ stress can overlap. This formation includes the greatest range of fault strikes, with dominant sets showing some differences between micro-faults and large faults. Here, micro-faults show a larger range of dominant strikes and likely formed when S_{Hmax} was oriented somewhere between W to NE, while faults present a smaller, but overlapping range of N-NW to NE. When including both types of faults the interpreted S_{Hmax} orientation is W to NE. This range encompasses the two possible in-situ S_{Hmax} orientations of NW and N interpreted from borehole breakouts and induced fractures.

Like in the Puente Formation, differentiating the timing of the individual fault sets in the Repetto Formation is difficult given such a large possible range. However, the Repetto Formation contains the closest proximity of S_{Hmax} interpreted from dominant fault sets compared to the in-situ stress orientation. This would suggest these faults developed under similar stress condition as the present day. However, this formation also

contains the largest variation of S_{Hmax} orientations when comparing across all facture types. Moreover, although the S_{Hmax} interpreted from resistive and conductive fractures differs insignificantly, both fracture types fall within the large range interpreted from faults and may characterize the principal stress orientations that existed for the various fault sets. This along with the larger diversity of minor and intermediate fault sets suggest that the Repetto Formation contains one of the most diverse records of paleo-stresses and has likely experience the greatest amount of deformation. Hence, differentiating the timing or narrowing the S_{Hmax} range for faults at the time they ruptured is not possible at this time with this data alone.

In the Pico Formation, the S_{Hmax} interpreted from faults and that of the in-situ S_{Hmax} orientation is slightly different for micro-faults, but can overlap for large faults. Here, the dominant S_{Hmax} orientation interpreted from micro-faults lies somewhere between NW to SW, while the S_{Hmax} interpreted from large faults is between N to W. However, the in-situ S_{Hmax} orientation is N-NW. It is possible that the faults striking more towards the north formed relatively recent under the present day stress regime, while those with strikes to the west formed under a different S_{Hmax} orientation. However, the micro-faults may show a closely spaced set of conjugate faults. In this case, the dominant S_{Hmax} orientation would be interpreted 285°, which would denote an alternative paleo-stress orientation was present at the time of their development. Furthermore, conductive and resistive fractures respectively record the existence of dominant NW to W S_{Hmax} orientations in the Pico Formation. This demonstrates that all dominant natural fracture sets found in this formation formed under different stress conditions than the in-situ stress interpreted from drilling induced fractures.

In the San Pedro Formation, all but one set of dominant faults do not appear to have been formed under the current in-situ S_{Hmax} orientation. Here, the in-situ S_{Hmax} orientation is N to N-NE, while the S_{Hmax} orientation range interpreted from micro-faults is NE to SE and that of large faults is W to NE. Here the only possible overlap of the in-situ stress exists for a N-NE striking set of faults. However, this set appears to be part of a conjugate dominant set of faults that would indicate the S_{Hmax} orientation would be 335° at the time of their rupture in the Pico Formation.

In the Pico Formation, all but one set of dominant faults do not appear to have been formed under the current in-situ S_{Hmax} orientation. Here, the in-situ S_{Hmax} orientation is N to N-NE, while micro-fault are more likely to have formed when S_{Hmax} was oriented NE to SE and faults when it was between W to NE. It appears the dominant sets of micro-faults and faults formed with almost no overlap. Moreover, the only possible overlap of the in-situ stress to that interpreted from faults is observed for a N-NE striking set of faults. However, this set is believed to be part of a conjugate dominant set of large faults, which would allocate the S_{Hmax} orientation as NW approximately 335° azimuth at the time of their rupture in the Pico Formation. Furthermore, the dominant micro-fault set has an identical strike to the dominant resistive fracture set found in this formation, while the interpreted S_{Hmax} orientation of the dominant set of large faults may overlap with that of conductive fractures. In either case, this suggests a mixture of possible in-suit and paleo-stress was present when these various fractures and faults were formed in the San Pedro Formation.

Tectonic Regime and Evolution

This section will focus on how the data and interpretations of principal stress orientations fit into previously proposed models of the tectonic evolution and geological regimes of the study area. Therefore, it will be compared to the prevalent paleotectonic model of the Los Angeles basin and previous interpretation of the Newport-Inglewood Fault. Observations made using resistive fractures will be the focal point of the discussion, but other fracture types will be discussed throughout as well.

The Los Angeles Basin and Newport-Inglewood Fault

The prevalent paleotectonic model for the development of the Los Angeles basin consists of three-stages (Ingersoll and Rumelhart, 1999). These stages include transrotation (18–12 Ma), followed by transtension (12–6 Ma), and then finally by transpression (6–0 Ma) (Ingersoll and Rumelhart, 1999). These stages are usually discussed in terms of three major basin-filling units, which correlate with the microplate-capture events that occurred during the conversion of the California coast from a convergent to a transform margin (Wright, 1991; Nicholson et al., 1994; Bohannon and Parsons, 1995; Ingersoll and Rumelhart, 1999). These basin-filling units consist of the Topanga Formation, Puente Formation, and Fernando Group, which consist of the Repetto and Pico Formations. Thus, with the exception of the Topanga Formation, 3 of the units typically associated with the three-stage evolution of the Los Angeles basin are encompassed in this study and should reflect some of these events.

By proximity, the Newport-Inglewood Fault Zone is a significant stress producing structure relative to the study area and, thus, should be reflected in the stress observed from this study. Currently, the Newport-Inglewood Faults forms part of the local

southern California system of faults that accommodates the tectonic deformation between the Pacific and North American plates (Wright, 1991; Walls et al., 1998). It has been proposed that it separates the continental granitic basement in the east from the metamorphic Catalina schist facies of the inner Continental Borderland to the west (Yerkes et al., 1965; Hill, 1971; Wright, 1991). It is thought to mark an area of structural weakness along a Mesozoic subduction zone (Hill, 1971) that is postulated to have reactivated with dextral strike-slip motion sometime in the upper Miocene to late Pliocene (Wright, 1991; Freeman et al., 1992; Grant and Shearer, 2004).

The stress associated with the prevalent paleotectonic model of the Los Angeles basin and the onset of the Newport Inglewood Fault would have produced significant stress changes within or proximal to the study area. Any fractures associated with these events should also reflect these changes. However, when comparing the principal paleo-stress orientations interpreted from fractures in this study, differences exist between observations made here and anticipated stress shifts from the previous models.

The most striking trends are observed with resistive fractures, which have a relatively consistent grouping of strikes compared to the other fractures. The S_{Hmax} interpreted from resistive fractures is orientated NW in the Puente and Repetto formations. It begins to show some variation to the N-NW in the Pico Formation, and then changes to the NE in the San Pedro Formation. The difference in S_{Hmax} orientation between the oldest and youngest formation is 120°.

The lack of variation in S_{Hmax} orientation observed in the Puente and Repetto formations presents no evidence of any significant stress regime changes associated with transrotation, transtension, and transpression. The first substantial change in the SHmax

orientation is observed between the Repetto and the Pico Formation. Here the NW orientation is still present, but a N-NW orientation is also introduced. This perhaps marks the first record of transpressional events in this area. However, it is important to note that the stress orientation associated with transpression may have been present long before 2.5 million years ago, which is the approximate age of the Repetto-Pico contact (Tsutsumi et al., 2001). However, the conditions necessary to produce fractures may not have been or the impact was not significant within the study area.

However, this change in stress orientation may overlap with the onset of the dextral propagation of the Newport-Inglewood Fault in the mid-to-late Pliocene. Thus, it is more likely a paleo-stress record of the S_{Hmax} orientation associated with this event and thus an argument can be made that the right-lateral strike-slip motion of the fault may have actually started 2.5 million ago or later. Additionally as the fault continues to propagate, the significant change in S_{Hmax} observed in the San Pedro Formation may represent the more localized stress associated with the compressional restraining bend and current left stepping surface rupture of the Newport-Inglewood Fault in the Long Beach oil field. Additionally, as the fault continues to rupture and move laterally to its current state, any pre-existing fractures and principal stress trajectories located south of the primary fault segments would have likely shifted towards the NE as dextral offset continues and is accommodated in the surrounding rocks. Consequently, this may account for the greater NE strikes of these fractures relative to the N-NE in-situ S_{Hmax} orientation found in this formation.

This interpretation of the initial right lateral onset of the fault is primarily focused on resistive fractures because they are the most robust fracture type. However, it is

important to note that the other fracture types do not show this same pattern. For example, conductive fractures show a large variation of strikes within and across formations, which speaks to a more complex structure. Even when isolating the most dominant fracture sets, decoding the timing of these events is difficult at this time. A more detailed analysis with a greater distribution of data within and away from the fault zone would be needed to distinguish the fractures that formed under macro and micro stress trajectories.

However, there is some evidence that suggests different stress regimes and structure changes across formations when comparing other fractures. For example, in the Pico Formation the strike of dominant conductive fracture sets changes to strike W and NW. This is the only formation where the S_{Hmax} interpreted from conductive fractures is relatively similar to that of resistive fractures. It reinforces the S_{Hmax} orientation recorded with resistive fractures, which may overlaps with the onset of the dextral propagation of the Newport-Inglewood Fault. Yet another change in S_{Hmax} is captured with conductive fractures when their strike orientation changes in the San Pedro Formation. Here, we are perhaps still seeing some of the similar events as in the Pico Formation, but overall these fracture strikes are closer to the in-situ orientation and likely formed during the present day stress directions.

When examining faults, the large range of possible S_{Hmax} orientations and lack of structural slip direction, rupture extent, structural positioning, and architecture limit the information we have available to assess their cross-cutting relationship to these formations and chronicle their timing or association to existing models. There are some variations of strikes seen within and across the four formations, however, the majority of

dominant fault sets have strikes that fall within the S_{Hmax} range of the main segment of the Newport-Inglewood Fault, which is locally called the Cherry Hill Fault. These faults may have formed under similar stress conditions and are likely synthetic faults, which typically form at acute angles of about 15° to the main line of faulting (Davis and Reynolds, 1996). Moreover, exceptions to these NW striking faults are also seen across all four formations, but our ability to differentiate between antithetic faults or faults that formed under different stress conditions, such as compressional faults, is limited without a sense of slip direction. Thus, the lack of information limits our ability to chronical their timing within the scope of the existing models. The best we can say at this time is whether these faults were formed under similar in-situ stress conditions, which was discussed in the previous section.

CHAPTER 6

CONCLUSIONS

A subsurface fracture analysis was performed in the Long Beach oil field, which is one of six major oil fields associated with the deformation caused by the Newport-Inglewood Fault Zone. Fractures from 12 electric borehole-image logs that collectively penetrate the Puente, Repetto, Pico, and San Pedro formations were used to interpret in-situ and paleo-principal stress orientations.

In-situ S_{Hmax} orientations derived from borehole breakouts and drilling-induced fractures indicate that in-situ orientations can range between 320° to 40° ($N40^0W$-$N40^0E$), but overall have a dominant N orientation. Anderson's stress model was applied to natural fractures and faults to interpret the S_{Hmax} orientations present at the time of their formations. These orientations were compared against the in-situ stress for each fracture type and for each formation. Variations from the in-situ stress, which were interpreted as paleo-stresses, were found for every fracture type within and across the four formations in this study.

Resistive fractures were determined to be the most robust set of fractures for interpreting potential principal stress changes associated with tectonic events. They showed a relatively consistent NW paleo-S_{Hmax} orientation in the Puente and Repetto Formations, but a N-NW orientation was introduced in the Pico Formation, which then changed to NE in the San Pedro Formation. The change in S_{Hmax} orientation in the Pico

Formation may signal the onset of the dextral movement of the Newport-Inglewood Fault 2.5 million years ago or later. It may also be the first time transpressional stress associated with the evolution of the Los Angeles Basin is captured by fractures in the Long Beach oil field. Additionally, greater NE strikes of resistive fractures relative to the N-NE in-situ S_{Hmax} orientation of the San Pedro Formation is likely a result of successive displacement of principal stress trajectories as the Newport-Inglewood Fault continues to propagate and the surrounding rocks accommodate the dextral offset of the fault.

CHAPTER 7

RECOMMENDATIONS FOR FUTURE RESEARCH

The discovery that principal stress orientation changes in the Pico Formation and may mark the onset of the dextral movement of the Newport-Inglewood Fault in the Long Beach oil field is important. Furthermore, the variation between in-situ principal-stress and paleo-stress is intriguing, but not entirely consistent with the paleo-stress changes anticipated for the Los Angeles basin. Consequently, the findings of this study raise a number of questions that were not able to be answered with the data set and scope of the study.

Fracture data for this study were interpreted from borehole image logs with variable vertical depth. The data were allocated by formation to minimize any possible variable sampling rates for wells that may not include the same logged intervals. Unfortunately, this study was not able to sample an equal lateral distribution for each formation. This limitation often restricted the ability to make direct comparisons between lateral geo-spatial positions of fractures and geo-spatial stress trajectory orientations in the same intervals. Additionally, the limitations of the logging tools to only image fractures within a vertical resolution of 5 mm (0.2 in.) and a depth of investigation of approximately 5 cm to the well bore, limited the size and type of fractures sampled for this study.

In an optimal situation, the geo-spatial position of the fractures relative to the structure would be evaluated with a greater sample distribution within and away from the

Newport-Inglewood Fault in order to distinguish between local and regional stress trajectories. Additionally, fracture morphology would also be compared against the mechanical stratigraphy of the fractured rock using core analysis and outcrop analogues. This would provide a greater in depth analysis of the fracture morphology, density and structural position relative to principal-stress trajectories. Moreover, analysis of mineral infilling of resistive fractures with thin sections and geochemistry would also provide a better understanding of the stress history in the Long Beach oil field.

REFERENCES

REFERENCES

Anderson, E.M., 1942, The dynamics of faulting and dyke formation with application to Britain: Edinburgh, Oliver and Boyd, p. 191.

Atwater, T.M., 1970, Implications of plate tectonics for the Cenozoic tectonic evolution of western North America: Geological Society of America Bulletin, v. 81, p. 3513-3536.

Axen, G.J., and Fletcher, J.M., 1998, Late Miocene–Pleistocene extensional faulting, northern Gulf of California, Mexico and Salton Trough, California: International Geology Review, v. 40, p. 217-244.

Barton, C., Moos, D., and Tezuka, K., 2009, Geomechanical wellbore imaging – Implications for reservoir fracture permeability: AAPG Bulletin, v. 93, p. 1551-1569.

Behl, R.J., 1999, Relationships between silica diagenesis, deformation and fluid flow in Monterey Formation cherts, Santa Maria Basin, Ca, *in* Eichhubl, P., ed., Diagenesis, deformation, and fluid flow in the Miocene Monterey Formation, Special Publication Pacific Section Society for Sedimentary Geology, v. 83, p.77-83.

Bell, J.S., and Gough, D.I., 1979, Northeast–southwest compressive stress in Alberta: Evidence from oil wells; Earth Planet Science Letter, v. 45, p. 475-482.

Blake, G.H., 1991, Review of the Neogene biostratigraphy and stratigraphy of the Los Angeles basin and implications for basin evolution: *in* Biddle, K.T., ed., Active Margin Basin: American Association of Petroleum Geologists Memoir 52, p.135-184.

Blake, M.C., Campbell, R.H., Diblee, T.W., Howell, D.G., Nilsen, T.H., Normark, W.R., Vedder, J.C., and Silver, E.A., 1978, Neogene basin formation in relation to plate-tectonic evolution of the San Andreas fault system, California: American Association of Petroleum Geologists Bulletin, v. 62, no. 3, p. 344-372.

Bohannon, R.G., and Parsons, T., 1995, Tectonic implications of post–30 Ma Pacific and North American relative plate motions: Geological Society of America Bulletin, v. 107, p. 937-959.

Broek, D., 1982, Elementary engineering fracture mechanics: New York, Springer-Verlag, p. 540.

Critelli, S., Rumelhart, P.E., and Ingersoll, R.V., 1995, Petrofacies and provenance of the Puente Formation (middle to upper Miocene), Los Angeles basin, southern California: Implications for rapid uplift and accumulation rates: Journal of Sedimentary Research, v. A65, p. 656-667.

Crouch, J.K., and Suppe, J., 1993, Late Cenozoic tectonic evolution of the Los Angeles basin and inner California Borderland: A model for core complex–like crustal extension: Geological Society of America Bulletin, v. 105, p. 1415-1434.

Davis, G.H., and Reynolds, S. J., 1996, Structural geology or rocks and regions, 2nd ed.: New York, John Wiley & Son, Inc., p. 1-737.

Division of Oil, Gas, and Geothermal Resources, 1992, California oil and gas fields, volumes 1, 2, and 3.

Eldridge, G.H., and Arnold, A., 1907, The Santa Clara Valley, Puente Hills, and Los Angeles oil districts, southern California: U.S. Geological Survey Bulletin, v. 309, p. 366.

Engelder, T., 1987, Joints and shear fractures in rock, *in* Atkinson, B. K., ed., Fracture mechanics of rock: London, Academic Press, p. 27-29.

Engelder, T., 1992, Stress regimes in the lithosphere: Princeton, Princeton University Press, 457 p.

Freeman, S.T., E.G. Heath, P.D. Guptil, and Waggoner, J.T., 1992, Seismic hazard assessment, Newport– Inglewood fault zone in engineering geology practice in southern California: Belmont, B. W. Pipkin and R. J. Proctor, p. 211-231.

Grant, L.B., and Rockwell, T.K., 2002, A northward-propagating earthquake sequence in coastal southern California?: Seismological Research Letters, v. 73, p. 461-469.

Grant, L.B., and Shearer, P.M., 2004, Activity of the offshore Newport–Inglewood Rose Canyon fault zone, coastal southern California, from relocated microseismicity: Seismological Society of America Bulletin, v. 94, p.747-752.

Grant, L.B., Waggoner, J.T., Rockwell, T.K., and Von Stein, C., 1997, Paleoseismicity of the north branch of the Newport-Inglewood fault zone in Huntington Beach, California, from cone penetrometer test data: Seismological Society of America Bulletin, v. 87, p. 277-293.

Halliburton, 2008, Wireline and perforating services: X-tended Range Micro Imager (XMRI) tool, Halliburton, H03629

Hamlin, H., 1918, Earthquakes in southern California: Bulletin of the Seismological Society of America, v. 8, p. 20-24.

Harding, T.P., 1973, Newport-Inglewood trend, California: An example of wrench style deformation: American Association of Petroleum Geologists Bulletin, v. 57, p. 97-116.

Hauksson, E., 1987, Seismotectonics of the Newport-Inglewood fault zone in the Los Angeles basin, southern California: Seismological Society of America Bulletin, v. 77, p. 539-561.

Hauksson, E., and Gross, S., 1991, Source parameters of the 1933 Long Beach earthquake: Seismological Society of America Bulletin, v. 81, p. 81-98.

Hennings, P., 2009, The Geologic Occurrence and Hydraulic Significance of Fractures in Reservoirs, *in* AAPG-SPE-SEG Hedberg research conference: American Association of Petroleum Geologists Bulletin, v. 93, p. 1407-1412.

Hill, M.L., 1971, Newport-Inglewood zone and Mesozoic subduction, California: Geological. Society of America Bulletin, v. 82, p. 2957-2962.

Hoots, H.W., 1931, Geology of the eastern part of the Santa Monica Mountains, Los Angeles county, California: U.S. Geological Survey Professional Paper C-165, scale 1:24, 000, p. 83–134.

Ingersoll, R.V., and Rumelhart, P.E., 1999, Three-stage evolution of the Los Angeles basin, southern California: Geology, v. 27, p. 593-596.

Lacazette, A., 2000, Breakouts and induced tensile fractures form at constant azimuths in the wellbore: http://www.naturalfractures.com, Web. 19 Feb. 2015.

Lacazette, A., 2009, Paleostress analysis from image logs using pinnate joints as slip indicators: American Association of Petroleum Geologists Bulletin, v. 93, p. 1489-1501.

Lagraba P., J. O., Hansen, S. M., Spalburg, M., and Helmy, M., 2010, Borehole image tool-design, value of information, and tool selection, in Poppelreiter, M., Garcia-Carballido, C., and Kraaijveld, M., ed., Dipmeter and borehole image log technology: American Association of Petroleum Geologists Memoir 92, p.15-38.

Luyendyk, B.P., 1991, A model for Neogene crustal rotations, transtension, and transpression in southern California: Geological Society of America Bulletin, v. 103, p. 1528-1536.

Luyendyk, B.P., and Hornafius, J.S., 1987, Neogene crustal rotations, fault slip, and basin development in southern California, *in* Ingersoll, R.V., and Ernst, W.G., eds., Cenozoic basin development of coastal California (Rubey Volume 6): Englewood Cliffs, NJ, Prentice Hall, p. 259-283.

Mendenhall, W.C., 1905, Development of underground waters in the western coastal plain region of southern California: U.S. Geological Survey Water-Supply and Irrigation Paper 139, p. 105.

Nicholson, C., Sorlien, C.C., Atwater, T., Crowell, J.C., and Luyendyk, B.P., 1994, Microplate capture, rotation of the western Transverse Ranges, and initiation of the San Andreas transform as a low angle fault system: Geology, v. 22, p. 491-495

Pollard, D.D., and Aydin, A., 1988, Progress in understanding jointing over the past century: Geological Society of America Bulletin, v. 100, p. 1181-1204

Rajabi, M., Sherkati, S., Bohloli, B., and Tingay, M., 2010, Subsurface fracture analysis and determination of in-situ stress direction using FMI logs –An example from the Santonian carbonates (Ilam Formation) in the Abadan Plain, Iran: Tectonophysics, v. 492, p. 192-200.

Redin, T., 1991, Oil and gas production from submarine fans of the Los Angeles basin, *in* Biddle, K.T., ed., Active margin basins: American Association of Petroleum Geologists Memoir 52, p. 239-259.

Rumelhart, P.E., and Ingersoll, R.V., 1997, Provenance of the upper Miocene Modelo Formation and subsidence analysis of the Los Angeles basin, southern California –Implications for paleotectonic and paleogeographic reconstructions: Geological Society of America Bulletin, v. 109, p 885-899.

Schlumberger, 2002, FMI: Borehole geology, geomechanics and 3D reservoir modeling, Schlumberger, SMP-5822

Taber, S., 1920, The Inglewood earthquake in southern California, June 21, 1920: Bulletin of the Seismological Society of America, v. 10, p. 129-145.

Teufel, Lawrence, 2012, Naturally Fractured Reservoir Class: Houston, Petroskills.

Tingay, M., Müller, B., Reinecker, J., Heidbach, O., Wenzel, F., and Fleckenstein, P., 2005, Understanding tectonic stress in the oil patch: The World Stress Map Project: The Leading Edge, v. 24, p. 1276-1282

Tsutsumi, H., Yeats, R.S. and Huftile, G.J., 2001, Late Cenozoic tectonics of the northern Los Angeles fault system: California Geological Society of America Bulletin, v. 113, p. 454-468.

United States Geological Survey, 2015, Quaternary Faults in Google Earth: Holocene to Latest Pleistocene; http://earthquake.usgs.gov/hazards/qfaults/google.php. "Acceded 3 March 2015."

Walls, C., Rockwell, T., Mueller, K., Bock, Y., Williams, S., Pfanner, J., Dolan, J., and Fang, P., 1998, Escape tectonics in the Los Angeles metropolitan region and implications for seismic risk: Nature, v. 394, p. 356-360.

Weigand, P.W., and Savage, K.L., 1993, Review of the petrology and geochemistry of the Miocene Conejo Volcanics of the Santa Monica Mountains, California, *in* Weigand, P.W., et al., eds., Depositional and volcanic environments of middle Tertiary rocks in the Santa Monica Mountains, southern California: Pacific Section, Society for Sedimentary Geology, Book 72, p. 93-112.

Wilcox, R.E., Harding, T.P., and Seely, D.R., 1973, Basic wrench tectonics: American Association of Petroleum Geologists Bulletin, v. 57, p. 74-96.

Wright, T.L., 1987, The Inglewood oil field, *in* Wright, T., and Heck, R., eds., Petroleum geology of coastal southern California: Pacific Section, American Association of Petroleum Geologists Guidebook 60, p. 41-49.

Wright, T.L., 1991, Structural geology and tectonic evolution of the Los Angeles Basin, *in* Biddle, K.T., ed., Active Margin Basin: American Association of Petroleum Geologists Memoir 52, p. 35-106.

Yeats, R.S., 1973, Newport-Inglewood fault zone, Los Angeles basin, California: American Association of Petroleum Geologists Bulletin, v. 57, p. 117-135.

Yeats, R.S., and Beall, J.M., 1991, Stratigraphic controls of oil fields in the Los Angeles basin overview, *in* Biddle, K. T., ed., Active margin basins: American Association of Petroleum Geologists Memoir 52, p. 221-237.

Yerkes, R.F., McCullon, T.H., Schoellhamer, J. E., and Vadder, J.G., 1995, Geology of the Los Angeles basin California, an introduction: USGS Professional Paper 420-A, p. 57.

Zippi, P.A., 2011, Biostratigraphy of the SHEU-38 well, Long Beach Oil Field, Los Angeles County, CA: Biostratigraphy.com, LLC Report 986, p. 1-13.

Zoback, M.D., 2007, Reservoir geomechanics: New York, Cambridge University Press, p. 464.